Ultraviolet Photoelectron Spectroscopy of Organic Anions

by

Adam J. Gianola

B.S., University of Nevada-Reno, 2000

A thesis submitted to the

Faculty of the Graduate School of the

University of Colorado in partial fulfillment

of the requirements for the degree of

Doctor of Philosophy

Department of Chemistry and Biochemistry

2006

This thesis entitled:

Ultraviolet Photoelectron Spectroscopy
of Organic Anions

Written by Adam J. Gianola

has been approved for

The Department of Chemistry and Biochemistry

by

_____

W. Carl Lineberger

_____

J. Mathias Weber

Date: _____

The final copy of this thesis has been examined by both the signatories, and we find that both the content and the form meet acceptable presentation standards of scholarly work in the above mentioned discipline.

Gianola, Adam J. (Ph.D. Physical Chemistry)

Ultraviolet Photoelectron Spectroscopy of Organic Anions

Thesis directed by Professor W. Carl Lineberger

Ultraviolet photoelectron spectroscopy has been used to study several negative organic ions and their corresponding neutrals: cyclopentadienide, pyrrolide, imidazolide, pyrazolide, vinyl diazomethyl anion, and 2-oxepinoxide. The photoelectron spectra obtained for these systems gives structural, vibrational, and electronic information about the corresponding neutral radicals.

Several of the ions listed above are related: cyclopentadienide, pyrrolide, imidazolide and pyrazolide. Each is a 5-membered ring system, with 0, 1, or 2 nitrogen atoms in the ring. The cyclopentadienyl radical is a well known radical exhibiting Jahn-Teller distortion, and these effects are evident in the photoelectron spectrum of cyclopentadienide. Replacement of one C—H group in cyclopentadienide by an N atom gives the pyrrolide ion. Jahn-Teller effects are no longer present in the radical counterpart, pyrrolyl; however, electronic interactions between the ground and first excited states are evident in the photoelectron spectrum. Imidazolide and pyrazolide are isomers of one another, and each has two N atoms in the ring. In imidazolide the N atoms are separated, while in pyrazolide they are adjacent. The corresponding radicals (imidazolyl and pyrazolyl) also show interesting electronic interactions between their ground and first excited states. In imidazolyl the interactions are weak, and the effects are not evident in the photoelectron spectrum. In pyrazolyl they are significantly stronger, and unexpected vibrational bands appear in the photoelectron spectrum as a result.

Also observed in the spectra of imidazolide and pyrazolide were photoelectron signals from other isomers. These isomers are nearly structurally identical to the imidazolide and pyrazolide ions, with the exception that a hydrogen atom is displaced from a carbon site

to a nitrogen site. The photoelectron spectra of these isomers appear very different. Electronic interactions in the analogous radicals are not present, and the photoelectron spectra appear very Franck-Condon like. Gas-Phase acidities for these ions were also obtained through bracketing experiments. Combination of the electron affinities obtained from the photoelectron spectra with these gas-phase acidities allows for determination of a C—H bond dissociation enthalpy of the parent molecules imidazole and pyrazole.

Although not a ring system, the vinyldiazomethyl anion is an isomer of imidazolide and pyrazolide. It can be thought of as a ring opened pyrazolide ion (by breaking a C—N bond). Its photoelectron spectrum is rather simple, appearing very Franck-Condon like. Interestingly, it appears that the spectrum originates mostly from the E-vinyldiazomethyl anion only; there is little indication of the presence of the Z-isomer. Franck-Condon simulations show each isomer would have a different spectral signature.

The 2-oxepinoxide anion is a seven-membered ring containing oxygen. The corresponding neutral, the 2-oxepinoxy radical, is a proposed intermediate in the combustion of benzene. The phenyl radical is expected to be formed first in a benzene flame, and many pathways for reaction of phenyl radical with O_2 have been studied theoretically. The phenyl-peroxy radical is thought to isomerize into the 2-oxepinoxy radical as a first step to the formation of CO, CO_2, and other combustion products. Production of the 2-oxepinoxide ion and subsequent photodetachment to form the 2-oxepinoxy radical is one of the first experimental steps to be taken to investigate these combustion pathways.

Acknowledgements

My advisor, Professor Carl Lineberger, is the first of a long list of people I would like to thank for assistance in my graduate career. Carl is a great advisor who has given me the chance to work in a fantastic place and interact with and meet many other people who share his enthusiasm for science. His ability to identify trouble spots with experiments and his physical intuition into the meanings of results still amaze me to this day. Somehow, Carl has managed to organize and run a research group which does high quality and very interesting science without sacrificing the comfort of an enjoyable work environment. Perhaps it is the experiments or maybe Carl himself who attracts students and postdocs who share common interests and similar attitudes.

It is also possible that these people are attracted by JILA. The facilities and personnel in JILA are surely among the best in the world. I would particularly like to thank James Fung-A-Fat from the electronics shop for his expertise with the electronics of the photoelectron spectrometer. Without his help, it would have been nearly impossible to navigate through the 'dark ages' and perform the experiments contained in this thesis. I think he still has the old voltage programmer sitting on a shelf next to his desk. I also thank Hans Green, Kim Hagen, and Todd Asnicar from the machine shop, who were always willing to drop whatever they were doing and give me a hand at a moments notice.

I would also like to thank Professors Barney Ellison and Veronica Bierbaum, whom I have had many close interactions with. Barney and I have had many informal discussions, which usually start with me intending to get his opinion on an experiment or result and always end with me being extremely interested in whatever unrelated topic we talked about instead. Regardless of this, Barney's enthusiasm for the research I have been working on has constantly helped me to maintain a positive attitude throughout graduate school. Veronica Bierbaum has been one of the most helpful people I have encountered in graduate school.

Several of the papers on my publication list have been in collaboration with her group, and without her careful attention to detail these papers would surely have numerous errors which were overlooked by several others including myself.

Two other professors who deserve my thanks are Professor Barry Carpenter and Professor John Stanton. Professor Carpenter suggested the experiments which are contained in Chapter 8 to me. He also helped me to realize how skillful I actually am in the lab when I put all my efforts forth. Professor Stanton was the person who suggested an elegant solution to the issues with my results that I didn't quite understand initially. He also has been a helpful friend who I felt comfortable speaking with very openly and honestly, who offered good advice to boot.

I want to thank all the members of the Lineberger, Ellison, and Bierbaum groups for their friendship and help over the years: Mark Taylor, Todd Sanford, Jack Barbera, Jeff Rathbone, Stephanie Villano, Alan Maccarone, Xu Xhang, Tim D'Andrea, Shuji Kato, Rebecca Hoenigman, and Nick Betts. I especially wish to thank Evan Jochnowitz, Django Andrews, and Jon Goldwin for being great friends and helping me out through the extremely difficult times of graduate school and life. There are also many other friends I met through the Chemistry Department who have entertained me at karaoke night and helped make my life in graduate school a little more enjoyable and probably a little longer: Chris Downey, Melissa Trainer, Aaron Miller, Michele Jacobson, Carrie Stoffel, Aaron Hieb and Jen Boots. Coincidentally, many of these people at one time or another joined me on the ice rink in our intramural ice hockey team, the Ice Buckets. Special thanks also go to Mary Ellen Flynn, Amanda Daflos, and Katarina Miller for being there to not talk science.

I also thank my parents and sisters who have never fully realized what I was still doing in school. Many times I heard "How are classes going?" or "When are you graduating?" when the answers to those question were usually "What classes?" and "I don't

know." Still, they have always been supportive and interested in whatever I was working to accomplish.

Finally, I wish to thank Danielle Blank for her love, support, and encouragement over the past few years. Whether she understood them or not, she has always been willing to listen to my problems (both scientific and otherwise) and I really have valued her opinion on practical matters concerning life and other day to day stuff. She has helped me talk out and deal with many problems which I'm sure other people were tired of hearing about. Without her I'm sure I would be in the funny farm by now!

Contents

Tables and Figures

1 Introduction

1.1 Anion Photoelectron Spectroscopy

Photoelectron spectroscopy is a useful tool for studying the properties of atomic and molecular anions, neutrals, and cations.[1-3] Neutral photoelectron spectroscopy involves measuring the kinetic energy of an electron removed from a neutral species with a photon, resulting in a cation and a free electron. Similarly, anion photoelectron spectroscopy involves measurement of the kinetic energy of an electron removed from an anion by a photon. Proper choice of the anionic species allows one to study unstable or short lived neutral species such radicals and transition states.[4]

An atomic anion (M^-) can absorb a photon of sufficient energy ($h\nu$) to detach an electron (e^-) with some kinetic energy, leaving a neutral, $M^- + h\nu \rightarrow M + e^-$. In anion photoelectron spectroscopy experiments, these electrons are collected and their kinetic energy distribution is measured. This distribution reflects the internal energy of the resulting neutral species. Conservation of energy requires that the energy of the photon absorbed in the detachment ($h\nu$) be equal to the kinetic energy of the detached electron (eKE) plus the binding energy of the electron (eBE), $h\nu = eKE + eBE$. If the energy of the incident photon is large enough, more strongly bound electrons can be detached from the anion resulting in electronically excited neutrals.

For atomic anions, the transitions from anion to neutral are purely electronic. With photons of a single energy, there will be discrete electron kinetic energies, each corresponding to detachment of a particular anion state to an electronic state of the neutral. As an example, Figure 1.1 shows the photoelectron spectrum of oxygen anion (O^-), and reflects the two lowest spin-orbit states of O^- ($^2P_{3/2,1/2}$) detaching to the three lowest states of

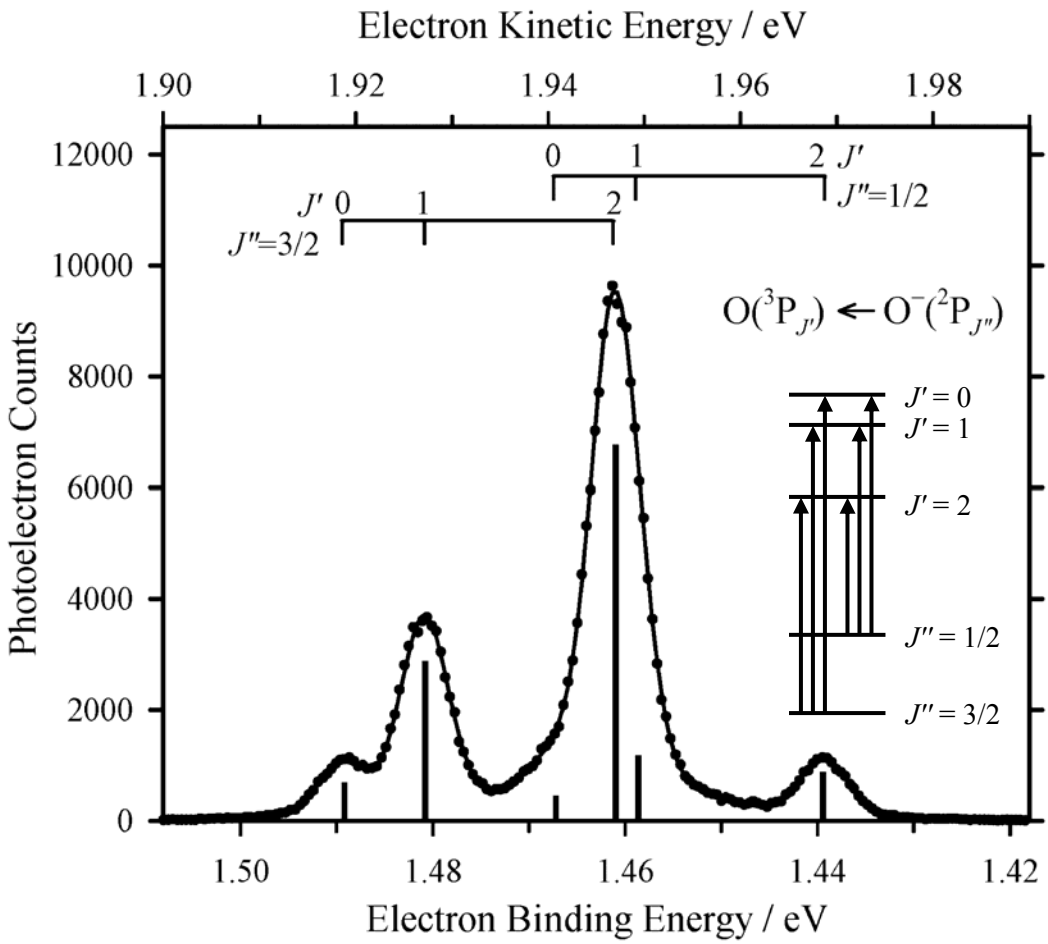

Figure 1.1 363.8 nm (3.408 eV) photoelectron spectrum of atomic oxygen anion (O^-). The spectrum is composed of six transitions, from the O^- ($^2P_{3/2,1/2}$) states to the O ($^3P_{2,1,0}$) states.[7]

oxygen atom ($^3P_{2,1,0}$).[5-7] For the spectrometer described in Chapter 2, the linewidth of atomic transitions is the instrumental linewidth, typically 6-12 meV fwhm Gaussian lineshape.

Molecular photoelectron spectra, on the other hand, can be considerably more complex than atomic photoelectron spectra, due to the fact that many vibrational and rotational levels may exist within a single electronic manifold.[1, 2] This internal energy must be taken into consideration when conservation of energy is applied to the system. Consider the photoelectron spectroscopy of a stable diatomic anion, AB^-. This ion will have a distribution of vibrational (E_{vib}), rotational (E_{rot}), and electronic (E_{elec}) energies. Likewise, the resulting neutral species will also have vibrational, rotational, and electronic energies, yielding the following for conservation of energy:

$$AB^-[E''_{vib}(v'')+E''_{rot}(J'')+E''_{elec}]+h\nu \rightarrow AB[E'_{vib}(v')+E'_{rot}(J') + E'_{elec}] + e^- \text{ (eKE)} \quad (1.1)$$

where a double prime indicates the initial state (the anion), and a single prime indicates the final state (the neutral). Since our instrumental resolution is typically inadequate to observe individual rotational levels, rotational broadening of an individual band is taken into account by application of a rotational correction[8] to the final energies obtained through:

$$AB^-[E''_{vib}(v'') + E''_{elec}] + h\nu \rightarrow AB[E'_{vib}(v') + E'_{elec}] + e^- \text{ (eKE)} \quad (1.2)$$

Figure 1.2 depicts the potential energy curves and vibrational energy levels for this hypothetical system.

The ion production method described in Chapter 2 produces ions which are thermalized to room temperature.[9, 10] Unless there are low lying electronic states in the anion (such as in O^-), there will typically be only one electronic state of the anion populated, with a thermal distribution of vibrational levels. The transition from the anion ground electronic, vibrational, and rotational state to the neutral ground electronic, vibrational, and rotational state is the origin of the electronic absorption (photodetachment) band. The energy of this

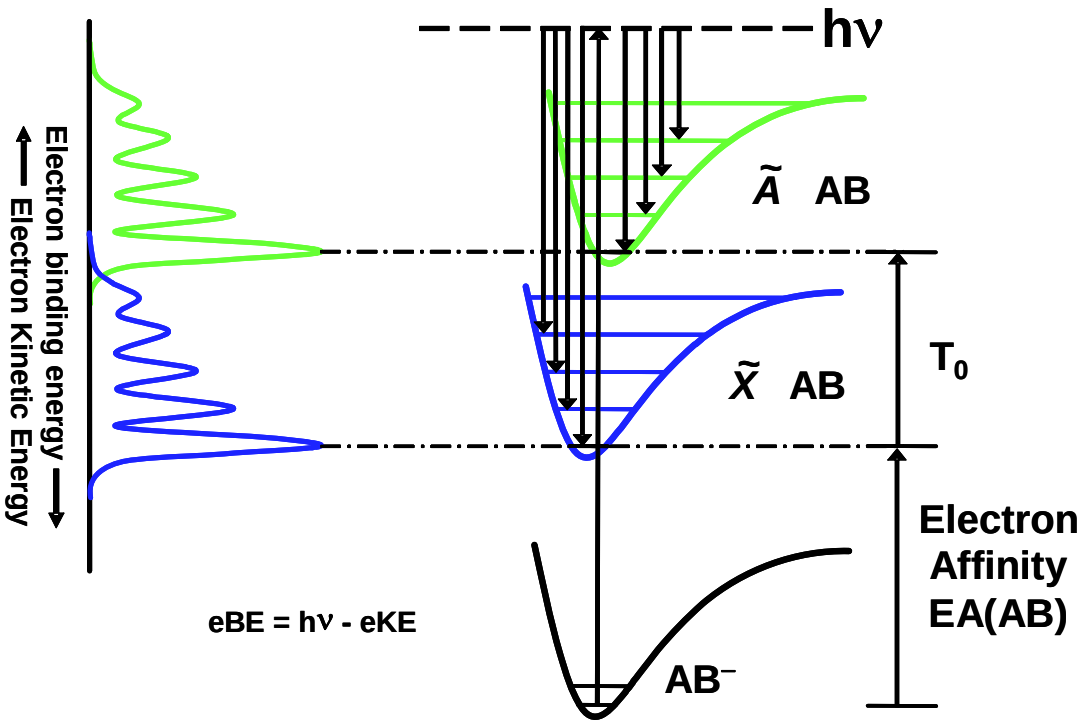

Figure 1.2 Schematic representation of photodetachment from molecular anion AB^- to two possible electronic states of neutral molecule AB.

transition is defined as the adiabatic electron affinity (EA) of the neutral species, EA(AB). A similar transition between the ground state of the anion and an electronically excited state of the neutral can yield an electronic energy splitting for the neutral, commonly referred to as a term energy, T_0. The term energy is simply the difference in binding energies between the ground vibrational level of the ground electronic state and the ground vibrational level of the excited electronic state: $T_0 = E_{ex}^0 - E_0^0$.

Since the vibrational energy levels of the anion and neutral are quantized, electrons will be detached with discrete energies corresponding to the transition between a particular vibrational state in the anion, and a vibrational state of the neutral. Transitions from a vibrationally excited anion, known as hot-bands, typically appear in the room temperature spectra and contain vibrational information for the anion. Likewise, transitions from the ground vibrational state of the anion yield vibrational information for the neutral species. By precisely measuring the difference between the discrete electron energies, relative vibrational energies can be determined.

The identities of different electronic states appearing in a photoelectron spectrum are determined by the orbital from which the outgoing electron is detached. For example, in a closed shell atomic anion, detachment of an electron from an s-orbital or p-orbital will respectively result in doublet S and doublet P states of the neutral atom appearing in the spectrum. Similarly, for a closed shell molecular anion, detachment of an electron in σ-type or π-type orbitals will result in doublet σ and doublet π states appearing in the spectrum. The energy necessary for these detachments can be approximated by the absolute energy of the orbitals in which the detached electrons are found in the anion.

1.2 Photoelectron Intensities and Selection Rules

The transition dipole moment, **M**, provides valuable information about a spectroscopic transition. In particular, selection rules can be derived to determine whether or not a transition is allowed and thus whether or not it is expected to be observed. Additionally, the square of the transition dipole moment is proportional to the intensity of a transition, allowing for direct comparison of the strengths of different transitions.[11, 12]

Specifying the initial and final states of the system by wavefunctions $\Psi_i(r,q)$ and $\Psi_f(r,q)$, respectively, and the transition moment operator by $\mu(r,q)$, the transition dipole moment is given by integrating over all electronic (r) and nuclear (q) coordinates:

$$\mathbf{M} = \left\langle \Psi_i(r,q) \middle| \mu(r,q) \middle| \Psi_f(r,q) \right\rangle \tag{1.3}$$

The Born-Oppenheimer approximation is invoked to separate the nuclear and atomic motion from one another. This approximation is based on the assumption that the electrons are much lighter and faster than the nuclei and can react quickly to changes in nuclear positions. The wavefunction for the system can then be separated as:

$$\Psi(r,q) = \psi_{vib}(q)\,\psi_{elec}(r,q) \tag{1.4}$$

Substituting into the transition dipole moment gives:

$$\mathbf{M} = \left\langle \psi_{vib,i}(q)\psi_{elec,i}(r,q) \middle| \mu(r,q) \middle| \psi_{vib,f}(q)\psi_{elec,f}(r,q) \right\rangle \tag{1.5}$$

If the transition moment operator is resolved into the sum of an electronic part and a nuclear part the transition dipole moment becomes:

$$\mathbf{M} = \left\langle \psi_{vib,i}(q)\psi_{elec,i}(r,q) \middle| \mu_{elec}(r) + \mu_{nuc}(q) \middle| \psi_{vib,f}(q)\psi_{elec,f}(r,q) \right\rangle \tag{1.6}$$

$$\begin{aligned} \mathbf{M} = &\left\langle \psi_{vib,i}(q)\psi_{elec,i}(r,q) \middle| \mu_{elec}(r) \middle| \psi_{vib,f}(q)\psi_{elec,f}(r,q) \right\rangle \\ &+ \left\langle \psi_{vib,i}(q)\psi_{elec,i}(r,q) \middle| \mu_{nuc}(q) \middle| \psi_{vib,f}(q)\psi_{elec,f}(r,q) \right\rangle \end{aligned} \tag{1.7}$$

Recognizing that the nuclear transition moment and vibrational wavefunctions do not depend upon the electronic coordinates, the second term in equation 1.7 can be rewritten, yielding:

$$\mathbf{M} = \left\langle \psi_{vib,i}(q)\psi_{elec,i}(r,q) \middle| \mu_{elec}(r) \middle| \psi_{vib,f}(q)\psi_{elec,f}(r,q) \right\rangle + \left\langle \psi_{vib,i}(q) \middle| \mu_{nuc}(q) \middle| \psi_{vib,f}(q) \right\rangle \left\langle \psi_{elec,i}(r,q) \middle| \psi_{elec,f}(r,q) \right\rangle \tag{1.8}$$

Noticing that electronic wavefunctions of different electronic states are orthogonal, it is clear that the second half of equation 1.8 is zero. Assuming the Condon approximation, the electronic wavefunctions are nearly constant over the range of nuclear coordinates sampled by the molecule and can be approximated as having an average internuclear separation of q_0. The remainder of the transition dipole moment can then be separated as:

$$\mathbf{M} = \left\langle \psi_{vib,i}(q) \middle| \psi_{vib,f}(q) \right\rangle \left\langle \psi_{elec,i}(r,q_0) \middle| \mu_{elec}(r) \middle| \psi_{elec,f}(r,q_0) \right\rangle \tag{1.9}$$

The square of equation 1.9 is proportional to the relative intensity of a transition:

$$I \propto |\mathbf{M}|^2 = \left| \left\langle \psi_{vib,i}(q) \middle| \psi_{vib,f}(q) \right\rangle \right|^2 \left| \left\langle \psi_{elec,i}(r,q_0) \middle| \mu_{elec}(r) \middle| \psi_{elec,f}(r,q_0) \right\rangle \right|^2 \tag{1.10}$$

Where the electronic transition strength is $|\langle \psi_{elec,i}(r,q_0)|\mu_{elec}(r)|\psi_{elec,f}(r,q_0)\rangle|^2$ and the Franck-Condon factor is the square of the vibrational wavefunction overlap, $|\langle \psi_{vib,i}(q)|\psi_{vib,f}(q)\rangle|^2$. A consequence of the Condon approximation is that for a given pair of electronic states, the electronic transition strength will be the same for all vibrational transitions and the relative intensities for the different vibrational transitions will be directly related to the Franck-Condon factors.

In the case of electron detachment, the initial-state wavefunctions describe the anion and the final-state wavefunctions describe the neutral species plus a free electron.[13] This leads to an important difference from typical electronic absorption spectroscopy: the total spin of the system must still be conserved, but since the electron detaches with a spin of ± ½ ħ, the spin of the molecule must also change by the same amount. This allows for appearance of both singlet and triplet states in a photoelectron spectrum when detaching from a doublet anion, allowing for direct measurement of a singlet-triplet splitting. Since only one electron is involved in the transition, a more general form of the spin selection rule for the molecule is

$\Delta S = \pm ½$. When there are resonance states in the continuum, however, this spin selection rule does not hold, such as in the case of N_2^- where there are shape and Feshbach resonances and two electrons can be involved in a transition.[13]

Since the absorbed photon brings with it 1ħ of angular momentum, an angular momentum selection rule exists for the system (molecule + unbound electron) of $\Delta J = 0, \pm 1$, completely analogous to conventional bound-bound spectroscopy. The outgoing electron may carry the angular momentum of the photon; if the electron is initially in an atomic s-type orbital, conservation of angular momentum requires that the electron be promoted to a p-type orbital, or detached as a p-wave. Similarly, an atomic p-type electron will be promoted to s-type or d-type orbitals, or detached as an s-wave or d-wave. For molecular orbitals, the detachment process is more complicated. A picture analogous to atomic detachment suggests that detachment from a σ molecular orbital will result in an outgoing wave with a π-type shape, and detachment of an electron from a π orbital will yield interfering σ-type and δ-type waves.

Each electronic state appearing in the photoelectron spectrum of a polyatomic anion is made up of one or more vibrational peaks. In atomic or molecular systems, there are 3N degrees of freedom, where N is the number of atoms. Of these, 3 degrees of freedom correspond to translation of the center of mass of the system, and for a nonlinear polyatomic molecule, like those described later in this dissertation, 3 more degrees of freedom correspond to the different rotations of the molecule as a whole. This leaves 3N-6 degrees of freedom for molecular vibrations. Assuming the normal mode approximation, the 3N-6 vibrational modes are separable and the overall Franck-Condon factor becomes a product of Franck-Condon factors for each vibrational mode.

Assuming the vibrations are all harmonic, vibrational selection rules can now be determined. For a non-zero Franck-Condon factor, the product $\langle \psi_{vib,i}(q) | \psi_{vib,f}(q) \rangle$ must be

totally symmetric; thus, totally symmetric vibrational modes can be active in a photoelectron spectrum for any Δv. By symmetry, the Franck-Condon factors for non-totally symmetric vibrational modes are zero for $\Delta v = \pm 1, \pm 3, \pm 5\ldots$ but can be non-zero for $\Delta v = 0, \pm 2, \pm 4\ldots$. In practice, non-totally symmetric vibrational modes have significant Franck-Condon factors only for $\Delta v = 0$ unless there is a large change in the vibrational frequency between the anion and the neutral.

Figure 1.2 shows potential curves in which there is only a small geometry change upon photodetachment. This results in the band origin having the largest Franck-Condon overlap which is thus the most intense feature in the spectrum, as seen in the curves on the left side of Figure 1.2. In some cases, however, the geometry shift upon photodetachment can be large. This will result in a small Franck-Condon factor for the band origin and much larger Franck-Condon factors for vibrationally excited levels of the neutral. The point in the spectrum with the most intensity (and largest Franck-Condon factor) is often referred to as a vertical detachment energy (VDE). This energy corresponds to the energy required to remove an electron with no geometry change. Figure 1.3 shows hypothetical potential energy curves for a harmonic oscillator where there is a large geometry change, and illustrates the differences between the band origin and VDE.

1.3 Nonadiabatic Effects

The above discussion of transition strengths holds well for many systems where the electronic state density is low. When electronic states lie very close in energy, there can be strong interactions between states. This usually indicates that non-adiabatic terms neglected in the Born-Oppenheimer approximation become significant contributions to the potential energy surface.

Mathematically, the potential energy surface can be represented by an expansion of the Hamiltonian about a reference nuclear configuration in the basis of noncoupled electronic states.[14] Including up to second-order terms, the potential is:

$$V_i = V_0 + \sum_{\alpha} \left\langle \Psi_i \left| \tfrac{\partial H}{\partial Q_\alpha} \right| \Psi_i \right\rangle Q_\alpha + \tfrac{1}{2} \sum_{\alpha} \left\langle \Psi_i \left| \tfrac{\partial^2 H}{\partial Q_\alpha{}^2} \right| \Psi_i \right\rangle Q_\alpha{}^2 - \sum_{\alpha, k \neq i} \frac{\left\langle \Psi_i \left| \tfrac{\partial H}{\partial Q_\alpha} \right| \Psi_k \right\rangle \left\langle \Psi_k \left| \tfrac{\partial H}{\partial Q_\alpha} \right| \Psi_i \right\rangle}{E_k - E_i} Q_\alpha{}^2 \tag{1.11}$$

Here, the index α covers all the normal modes, while *i* and *k* describe all the relevant electronic states. The last term in Equation 1.11 is where interactions between different electronic states can arise. The matrix elements in this term are nonzero only when considering the appropriate symmetry vibration which can couple the two electronic states. For example, consider a molecule in the C_{2v} point group with electronic states of A_2 and B_1 symmetry. The last term in Equation 1.11 is nonzero only when considering b_2 vibrations since $a_2 \times b_1 = b_2$. Also, notice that when the energy splitting between two electronic states is small, this term can become very large.

This type of coupling can have large effects on the potential energy surfaces of interacting electronic states. For example, if the coupling term is large enough, the potential surface can curve downward along a coupling coordinate, transforming a stationary point which would otherwise be a minimum into a transition state with one or more imaginary frequencies. When considering the interaction where $E_k - E_i$ is negative, this term causes the potential surface to become steeper along the coupling coordinate, and can shift vibrational frequencies to much larger and unexpected values. Often, when electronic structure calculations compute frequencies that are too large or too small for a system which is otherwise expected to have "normal" vibrational frequencies, it may be an indication that electronic states are interacting with one another.

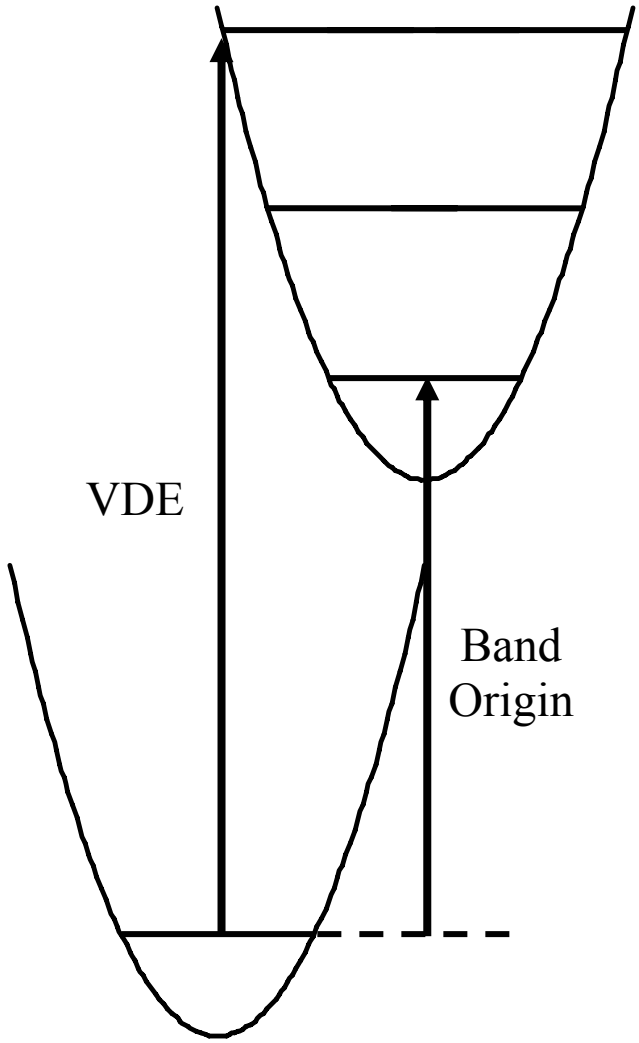

Figure 1.3 Harmonic oscillator potential energy curves showing a large geometry change upon photodetachment.

1.4 Photoelectron Angular Distributions

Photoelectron intensities can also vary with the polarization of the incoming linearly polarized photons.[15, 16] By controlling the angle between the laser polarization and the photoelectron collection axis it is possible to measure the relative angular distributions of a photoelectron spectrum. Photoelectron intensities have angular distributions according to:

$$I \propto \frac{\sigma_{total}}{4\pi}\left[1+\beta P_2(\cos\theta)\right] \tag{1.12}$$

where $P_2(\cos\theta)$ is the second Legendre polynomial [$\frac{1}{2}(3\cos^2\theta - 1)$], θ is the angle between the laser polarization and the photoelectron collection axis, σ_{total} is the total photodetachment cross section, and β is the anisotropy parameter which can range from -1 to 2.[15, 16]

Detachment from different symmetry orbitals will yield different photoelectron angular distributions. For example, detachment of an electron in an atomic s-orbital, such as from H^-, will result in an outgoing p-wave, which will be oriented along the laser polarization and have a $\cos^2\theta$ behavior ($\beta = 2$). On the other hand, detachment of an electron in an atomic p-orbital, such as from O^-, will result in both s- and d-waves. These may interfere and, depending on the photon energy, yield values for β typically between -1 and 0. Detachment from molecular orbitals is more complicated, but previous measurements have shown that $\beta < 0$ for detachment from π-type molecular orbitals and $\beta > 0$ for detachment from σ-type molecular orbitals.[17, 18]

For the results described later in this dissertation, the anisotropy parameter gives clues to the type and symmetry of the molecular orbital from which electrons are detached. Additionally, it is also used to distinguish features arising from different electronic states in the same spectrum. Most of the spectra presented have the laser polarization at the magic angle ($\theta = 54.7°$) to the photoelectron collection axis. The magic angle is the angle where $P_2(\cos\theta) = 0$, and the photoelectron intensities are simply proportional to the total

photodetachment cross section and are free from angular effects. Values of the anisotropy parameter are estimated by relative intensity measurements with the laser polarization parallel ($\theta = 0°$) and perpendicular ($\theta = 90°$) to the photoelectron collection axis:

$$\beta \approx \frac{I_{0°} - I_{90°}}{\frac{1}{2} I_{0°} + I_{90°}} \tag{1.13}$$

1.4 Dissertation Outline

This dissertation is split among several chapters. Chapter 2 describes the anion photoelectron spectrometer in detail, including components of the optical system. It also describes the general computational methods used for simulation and analysis of the spectra. Chapters 3-8 each describe the experimental results obtained for a single parent molecule.

Chapter 3 describes the results obtained from the cyclopentadiene molecule (C_5H_6). Cyclopentadiene is a 5-membered ring molecule consisting only of carbon and hydrogen. Spectra of the corresponding anion, cyclopentadienide ($C_5H_5^-$), have been previously obtained;[19] however, the spectra presented here have much higher resolution and allow for determination of more of the vibrational properties of the analogous neutral, cyclopentadienyl radical (C_5H_5•), a well-known Jahn-Teller molecule.[20, 21]

The photoelectron spectra obtained from the pyrrole system (C_4H_5N) are the subject of Chapter 4. Similar to cyclopentadiene, pyrrole is a five-membered ring molecule; unlike cyclopentadiene, pyrrole contains carbon, hydrogen, *and* nitrogen. By substituting a nitrogen atom for a C—H group, cyclopentadiene and pyrrole are isoelectronic. This substitution eliminates Jahn-Teller effects in the pyrrolyl radical system, though other non-adiabatic effects influence the appearance of the spectra.

Substitution of a nitrogen atom for another C—H group results in other isoelectronic systems ($C_3H_4N_2$). If the substitution is such that the nitrogen atoms are separated in the

5-membered ring, the result is the imidazole molecule, the subject of Chapter 5. If the two nitrogen atoms are adjacent in the 5-membered ring, pyrazole is the result, and is the subject of Chapter 6. Although isomers, the photoelectron spectra of the corresponding anions, imidazolide and pyrazolide, appear very different. Non-adiabatic effects still influence both spectra, but the effects are small in the imidazolyl radical system and much larger in the pyrazolyl radical system. Additionally, photodetachment signals are observed for isomeric anions of imidazolide and pyrazolide. These anions retain the ring structure, but are deprotonated at a carbon-site instead of the nitrogen-site.

Chapter 7 discusses the results from another isoelectronic system, vinyldiazomethane ($C_3H_4N_2$). Vinyldiazomethane is a ring-opened isomer of imidazole and pyrazole. The backbone of the molecule has the structure of pyrazole where a C—N bond is broken and the ring is opened. The corresponding anion (the vinyldiazomethyl anion) is not produced from deprotonation as the anions described in other chapters, but is actually synthesized in the flow tube in a molecule/anion reaction between N_2O and allyl anions ($C_3H_5^-$). Two conformers (E and Z) of the vinyldiazomethyl anion are expected to be formed in the flow tube, but analysis of the detachment signals indicates only one is formed in detectable amounts.

Chapter 8 focuses on the photoelectron spectra of the 2-oxepinoxide anion, whose corresponding radical (2-oxepinoxyl) is a suspected reactive intermediate formed during the combustion of benzene and has been the focus of several theoretical investigations. The spectra presented here represent some of the first experimental results obtained on this radical species and are performed with the ultimate goal of obtaining the heat of formation of the 2-oxepinoxyl radical.

Chapter 9 provides a summary of the experimental results presented in this dissertation and includes a discussion of the trends observed in the photoelectron spectrum of the 5-membered ring anions. These trends are used in an extrapolation to approximate the

properties of 5-membered ring systems which contain more nitrogen atoms. Future work which builds on the results presented here is also discussed.

Chapter 1 References

[1] J.H.D. Eland, *Molecular Photoelectron-Spectroscopy.* Journal of Physics E-Scientific Instruments, 1978. **11**(10): p. 969-977.

[2] K.M. Ervin and W.C. Lineberger, *Photoelectron Spectroscopy of Negative Ions*, in *Advances in Gas Phase Ion Chemistry*, N.G. Adams and L.M. Babcock, Editors. 1992, JAI Press: Greenwich. p. 121-166.

[3] P. Chen, *Photoelectron Spectroscopy of Reactive Intermediates*, in *Unimolecular and Bimolecular Reaction Dynamics*, C.Y. Ng, T. Baer, and I. Powis, Editors. 1994, Wiley & Sons: New York. p. 371-425.

[4] P.G. Wenthold and W.C. Lineberger, *Negative ion photoelectron spectroscopy studies of organic reactive intermediates.* Accounts of Chemical Research, 1999. **32**(7): p. 597-604.

[5] C.E. Moore, *Atomic Energy Levels*. NSRDS-NBS. 1952, Washington: US GPO Circular No. 467.

[6] D.M. Neumark, K.R. Lykke, T. Andersen, and W.C. Lineberger, *Laser Photodetachment Measurement of the Electron-Affinity of Atomic Oxygen.* Physical Review A, 1985. **32**(3): p. 1890-1892.

[7] K.M. Ervin, W. Anusiewicz, P. Skurski, J. Simons, and W.C. Lineberger, *The only stable state of O_2^- is the $X\,^2\Pi_g$ ground state and it (still!) has an adiabatic electron detachment energy of 0.45 eV.* Journal of Physical Chemistry A, 2003. **107**(41): p. 8521-8529.

[8] P.C. Engelking, *Approximate Rotational Band Shifts.* Journal of Physical Chemistry, 1986. **90**(19): p. 4544-4545.

[9] D.G. Leopold, K.K. Murray, and W.C. Lineberger, *Laser Photoelectron-Spectroscopy of Vibrationally Relaxed CH_2^- - a Reinvestigation of the Singlet Triplet Splitting in Methylene.* Journal of Chemical Physics, 1984. **81**(2): p. 1048-1050.

[10] D.G. Leopold, K.K. Murray, A.E.S. Miller, and W.C. Lineberger, *Methylene - a Study of the $X\,^3B_1$ and $^1A_1$ States by Photoelectron-Spectroscopy of CH_2^- and CD_2^-.* Journal of Chemical Physics, 1985. **83**(10): p. 4849-4865.

[11] P.F. Bernath, *Spectra of Atoms and Molecules*. 1995, New York: Oxford University Press.

[12] D.C. Harris and M.D. Bertolucci, *Symmetry and Spectroscopy An Introduction to Vibrational and Electronic Spectroscopy*. 1978, New York, NY: Oxford University Press.

[13] J. Simons, *Detachment Processes for Molecular Anions*, in *Photoionization and Photodetachment*, C.Y. Ng, Editor. 1999, World Scientific: River Edge, NJ. p. 958-1010.

[14] R.G. Pearson, *A symmetry rule for predicting molecular structure.* Journal of the American Chemical Society, 1969. **91**: p. 4947-4955.

[15] J. Cooper and R.N. Zare, *Angular distribution of photoelectrons.* Journal of Chemical Physics, 1968. **48**: p. 942-943.

[16] J.L. Hall and M.W. Siegel, *Angular dependence of the laser photodetachment of the negative ions of carbon, oxygen, and hydrogen.* Journal of Chemical Physics, 1968. **48**: p. 943-945.

[17] R.F. Gunion, M.K. Gilles, M.L. Polak, and W.C. Lineberger, *Ultraviolet Photoelectron-Spectroscopy of the Phenide, Benzyl and Phenoxide Anions, with Abinitio Calculations.* International Journal of Mass Spectrometry and Ion Processes, 1992. **117**(1-3): p. 601-620.

[18] P.G. Wenthold, M.L. Polak, and W.C. Lineberger, *Photoelectron spectroscopy of the allyl and 2-methylallyl anions.* Journal of Physical Chemistry, 1996. **100**(17): p. 6920-6926.

[19] P.C. Engelking and W.C. Lineberger, *Laser Photoelectron Spectrometry of $C_5H_5^-$ - Determination of Electron-Affinity and Jahn-Teller Coupling in Cyclopentadienyl.* Journal of Chemical Physics, 1977. **67**(4): p. 1412-1417.

[20] B.E. Applegate, A.J. Bezant, and T.A. Miller, *The Jahn-Teller and related effects in the cyclopentadienyl radical. II. Vibrational analysis of the $A\,^2A_2''$ - $X\,^2E_1''$ electronic transition.* Journal of Chemical Physics, 2001. **114**(11): p. 4869-4882.

[21] B.E. Applegate, T.A. Miller, and T.A. Barckholtz, *The Jahn-Teller and related effects in the cyclopentadienyl radical. I. The ab initio calculation of spectroscopically observable parameters.* Journal of Chemical Physics, 2001. **114**(11): p. 4855-4868.

2 Methodology

2.1 Overview

The anion photoelectron spectrometer used to perform the experiments described in this dissertation consists of four major parts: the ion source, the ion optics and mass selection elements, the laser system, and the electron energy analyzer. A flowing afterglow ion source is used to create a beam of negative ions. The ion beam is accelerated, shaped and focused, and passed through a Wien velocity filter for mass selection. The mass selected ion beam is then focused and decelerated for interaction with a photon beam. Photoelectrons are produced at the interaction region and a portion of them are energy analyzed using a hemispherical energy analyzer. The electrons are detected using a position sensitive detector which digitizes the position of the electrons for analysis by a computer. This chapter focuses on the components of the anion photoelectron spectrometer in detail, and is accompanied by a discussion of the computational methods used to simulate and analyze the spectra.

2.2 Ion Source

The experiments described later in this thesis were performed using a common ion source, known as a microwave discharge flowing afterglow ion source. The microwave discharge ion source is made of two components, a brass microwave cavity, and a quartz discharge cylinder.[1, 2] Figure 2.1 illustrates the construction of the microwave discharge source. Helium buffer gas, purified by passing through a liquid nitrogen cooled molecular sieve trap, is passed through the quartz discharge cylinder at a rate of 6-8 standard liters per minute (controlled by an adjustable Tylan flow controller), along with a trace amount of O_2 (7-10 standard cm^3 per minute). The discharge is ignited by means of a Tesla coil, which produces a plasma containing unbound electrons. The electrons absorb the 2.45 GHz

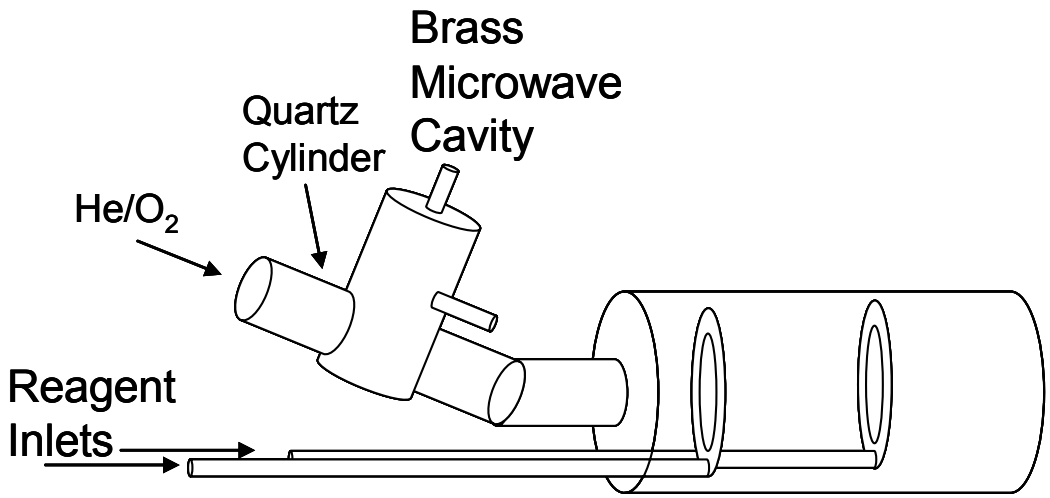

Figure 2.1 Microwave Discharge Ion Source. A brass microwave cavity encloses a quartz discharge cylinder. The microwave discharge is connected to the flow tube where ions react with neutral reagents introduced through movable ring inlets.

microwave radiation which maintains the plasma.[3] The microwave radiation is provided from an Opthos MPG 4 Microwave Power Generator. Typical discharge ignition is achieved by providing ~70 W of forward power to the brass cavity and energizing the Tesla coil on the quartz cylinder. Once a stable discharge is produced, the forward power is reduced and the majority of the radiation is absorbed by the plasma; correspondingly, the reflected power should be near zero, protecting the magnetron in the microwave generator. The forward power may be adjusted to achieve maximum ion signal. For production of atomic oxygen anion (O^-), for example, the smallest forward power necessary to maintain the discharge produces the maximum ion signal.

Atomic oxygen anions are used as the main anion precursor and are produced in the discharge by dissociative electron attachment to O_2:

$$O_2 + e^- \rightarrow O_2^{-*} \rightarrow O^- + O \tag{2.1}$$

Two movable ring inlets are located just downstream from the microwave discharge and used to introduce precursor molecules into the flow tube for subsequent reaction. For example, introduction of methane (CH_4) into the flow tube results in production of hydroxide (HO^-), another major ion precursor, via a hydrogen transfer reaction with O^-:

$$O^- + CH_4 \rightarrow HO^- + CH_3 \tag{2.2}$$

These inlets may be used to titrate a reaction by adjusting their relative position in the flow tube for the appropriate reaction distance (reaction time).

Once created, the anions continue down the flow tube where they are thermalized to room temperature by 10^4 – 10^5 collisions with the He buffer gas.[1, 2] The source region is pumped by a 330 l/s Stokes Roots Blower. A typical flow tube pressure is 0.4 Torr (~50 Pa) at 7.3 standard liters per minute of He. Surrounding the flow tube is a jacket which may be filled with liquid nitrogen to aid in further cooling of the ions to roughly 200 K.

2.3 Ion Optics and Mass Selection

The ions are gently extracted from the flow tube through a small aperture (~1 mm) in a nosecone at 0-3 volts, where they encounter the first of a series of adjustable ion optics and deflectors (called the afterglow lenses); here the ions are focused and accelerated to 736 eV kinetic energy. A 2000 l/s 6-inch diffusion pump maintains the vacuum chamber pressure in the afterglow lens region at about 10^{-4} Torr (~10^{-2} Pa). Figure 2.2 illustrates construction of the flow tube and afterglow lenses. The nosecone, first three lens elements (L1-L3) and first deflector (D1H and D1V) are mounted in the vacuum chamber as a single assembly. The potentials on L1, L2, and L3 can be adjusted separately and deflector D1 is referenced to the L3 potential and has independent horizontal and vertical deflections. The next series of lenses and second deflectors are also mounted as a single assembly with an aperture plate on the front. The first assembly fits over the second assembly to ensure the ion trajectories are not affected by the ground potential of the vacuum chamber walls. Lens element L4 is also adjustable and deflector D2 is referenced to the L4 potential and has independent horizontal and vertical deflections. Lens elements L5 and L6 are given constant potentials of 400 and 736 volts, respectively. Table 2.1 lists typical potentials for all adjustable elements.

Beyond lens element L6 is another pair of deflectors (D3) which are used to steer the anions, now traveling at 736 eV kinetic energy, through a 10° bend in the ion flight path. These deflectors allow the anions to be steered thought the 10° bend, while neutrals and photons collide with the vacuum chamber walls. Following the 10° bend is a 3-element quadrupole einzel lens (Q1) which is used to focus and deflect the ion beam[4] through an aperture plate, A2. The ion current is measurable on this aperture by means of a Keithley 600A electrometer. Typical total ion beam currents are 10-30 nA. This region is pumped by a 3000 l/s 8-inch diffusion pump to a pressure of 10^{-6} Torr (~10^{-4} Pa). Figure 2.3 depicts this region of the instrument. A pair of deflectors (DL4) follow, and another 3-element

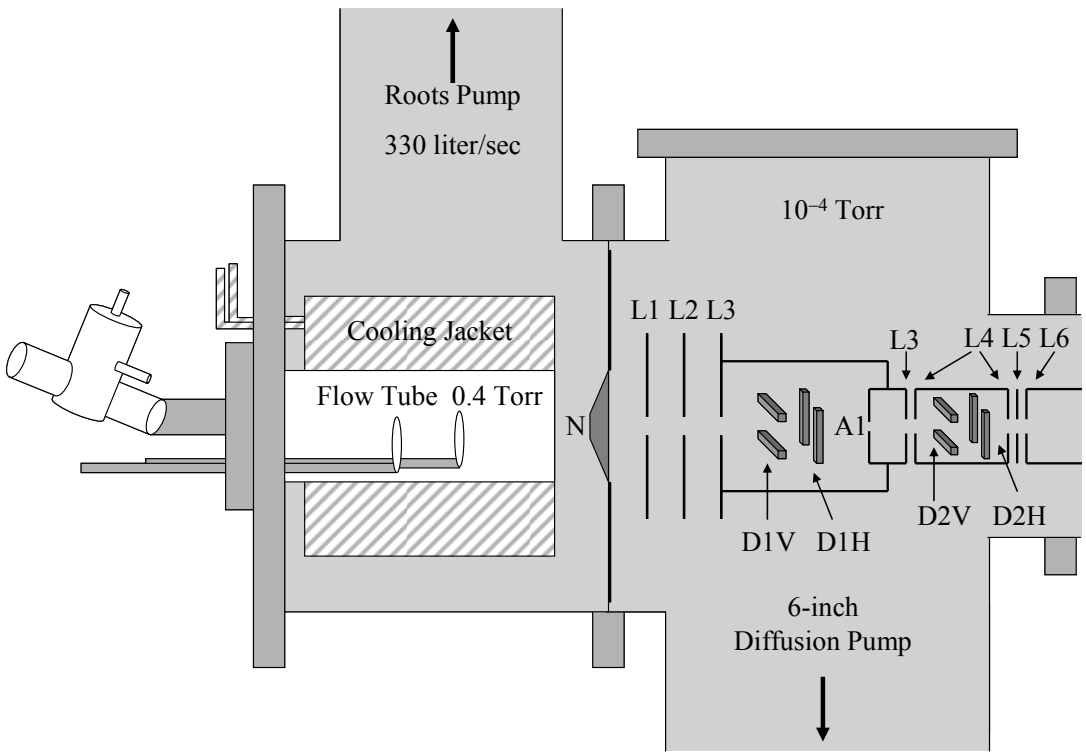

Figure 2.2 Flow tube and afterglow ion optics. The nosecone is labeled N, acceleration lenses are labeled L1-L6, deflectors are labeled D1 and D2, and the aperture is labeled A1.

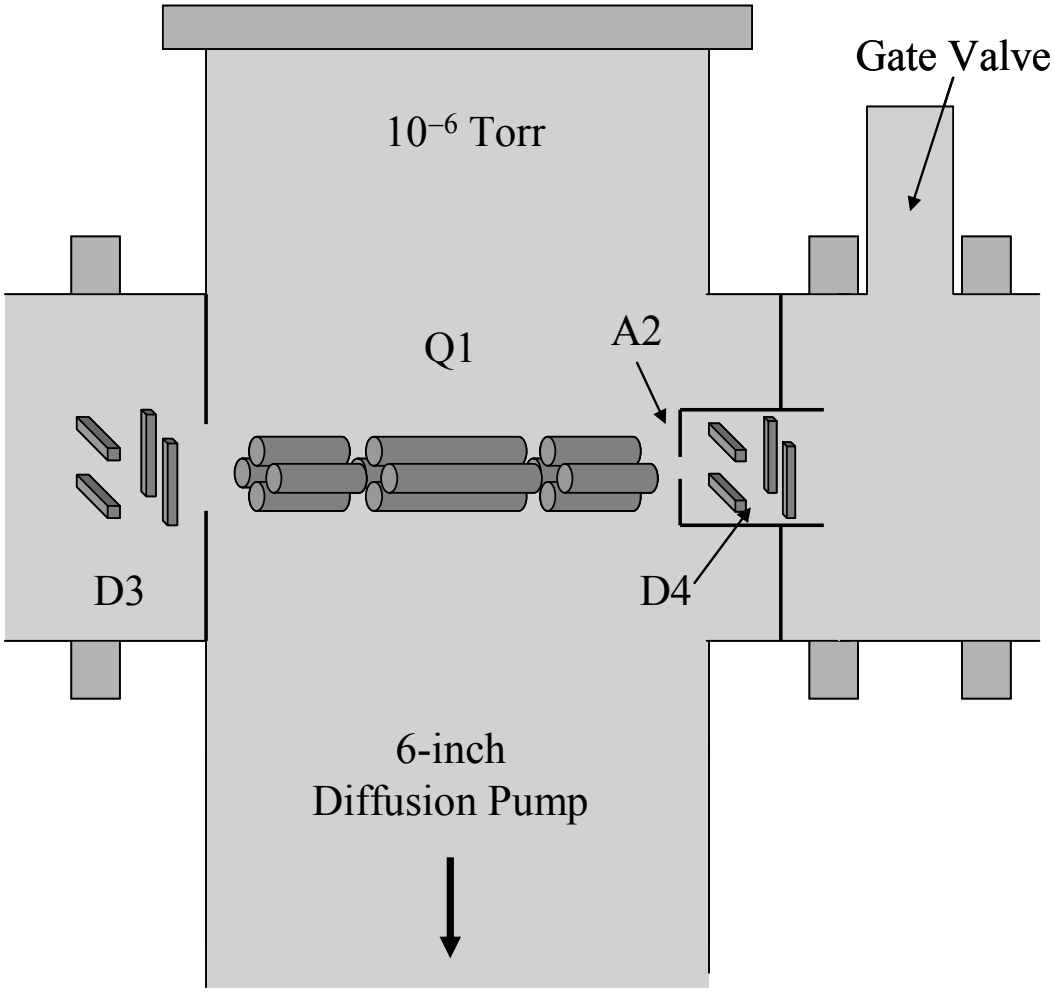

Figure 2.3 10 degree deflectors (D3), first 3-element quadrupole einzel lens (Q1), second aperture (A2) and fourth deflectors (D4).

Element	Typical Potential		Element	Typical Potential
Nosecone	1 V		Q4 Inner Right	25 V
L1	25 V		Q4 Inner Left	40 V
L2	160 V		Q4 Inner Top	-33 V
L3	175 V		Q4 Inner Bottom	-37 V
D1 Horizontal	0 V		Q4 Outer Vertical	38 V
D1 Vertical	0 V		Q4 Outer Horizontal	-39 V
L4	181.7 V		D5 Horizontal	-47 V
D2 Horizontal	0 V		D5 Vertical	24 V
D2 Vertical	0 V		DL1	736 V
L5	400 V		DL2	134 V
L6	736 V		DL3	360 V
D3 Vertical	0 V		DL4	35 V
D3 Horizontal	±75 V		Interaction Region	35 V
Q1 Inner Top	19 V		Computer eKE	2.06
Q1 Inner Bottom	20 V		Computer V3	0.1
Q1 Inner Right	-20 V		Manual Te	3.97 V
Q1 Inner Left	-20 V		V1	17.29 V
Q1 Outer Horizontal	26 V		V2	16.04 V
Q1 Outer Vertical	-27 V		V3	0.572 V
D4 H	13 V		V4	15.28 V
D4 V	8 V		VHC	1.958 V
Q2 Inner Top	17 V		VIN	3.38 V
Q2 Inner Bottom	15 V		VOUT	1.352 V
Q2 Inner Right	-18 V		Contact Potential	-0.428 V
Q2 Inner Left	-17 V		V5	28.62 V
Q2 Outer Horizontal	21 V		V6	245.4 V
Q2 Outer Vertical	-22 V		1st MCP	250.7 V
E-Field Voltage	60 V		Last MCP	3573 V
B-Field Voltage	3.2 V for O^-			
Q3 Inner Top	18 V			
Q3 Inner Bottom	7 V			
Q3 Inner Right	-14 V			
Q3 Inner Left	-14 V			
Q3 Outer Horizontal	14 V			
Q3 Outer Vertical	-16 V			

Table 2.1 Typical potentials for the photoelectron spectrometer.

quadrupole lens (Q2) sits behind a gate valve. These ion optics are used to focus and deflect the ion beam into the mass selection region.

The mass selection region used in the photoelectron spectrometer is a velocity filter consisting of perpendicular electric and magnetic fields, a Wien filter. The Wien filter sits in a common assembly with the second and third 3-element quadrupole lenses (Q2 and Q3) as illustrated in Figure 2.4. This region is pumped to a pressure of 10^{-7} Torr (~10^{-5} Pa) by a 250 l/s Varian Turbomolecular Pump.

The velocity filter operates according to the following principles. The force on an ion from an electric field is the product of the charge of the ion, q, and the electric field, $\vec{E}$: $\vec{F} = q\vec{E}$. The force on an ion from a magnetic field depends not only upon the charge of the ion and direction and magnitude of the field, $\vec{B}$, but on the direction and magnitude of the ion's velocity, $\vec{v}$: $\vec{F} = q\vec{v} \times \vec{B}$. By setting these two forces equal and opposite, it is possible for an ion to pass through the Wien filter undeflected. All ions have the net charge of a single electron, and thus all feel the same force from the electric field. Since all ions have the same kinetic energy (½ mv^2 = 736 eV), there will be a velocity distribution of the ions, with the lighter ions traveling faster and the heavier atoms traveling slower, resulting in different forces for different mass ions. Ions which are too heavy or too light are deflected and neutralized by the walls of the Wien filter. To select which mass ion is passed through the Wien filter undeflected, the magnetic field is adjusted while the electric field is kept constant. The magnetic field is created via a water cooled electromagnet powered by a 0-10A / 0-60V Kepco regulated DC voltage supply. The electric field sector is constructed as illustrated in Figure 2.5; voltages are provided by a voltage divider circuit powered by a 0-40mA / 0-500V power supply. The Wien filter has a mass resolution of $m/\Delta m \approx 40$, which is sufficient for separation of O^-, HO^-, and the deprotonated species described later with masses of 60-90 amu.

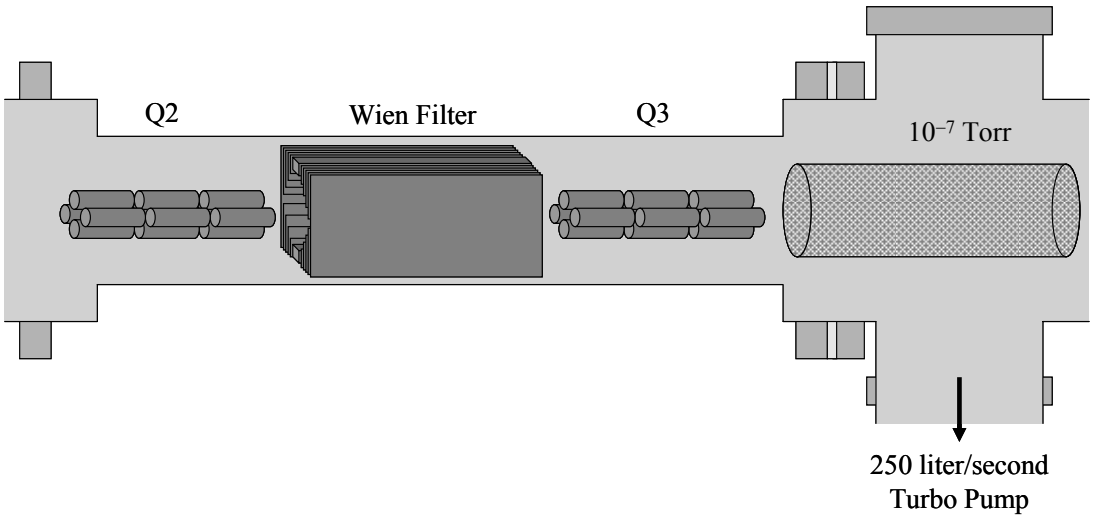

Figure 2.4 Wien filter region of the photoelectron spectrometer. Ions are focused into the Wien filter with 3-element quadrupole Q2 and mass selected inside the Wien filter. The mass selected ions are refocused with 3-element quadrupole Q3 and pass through a short field-free region.

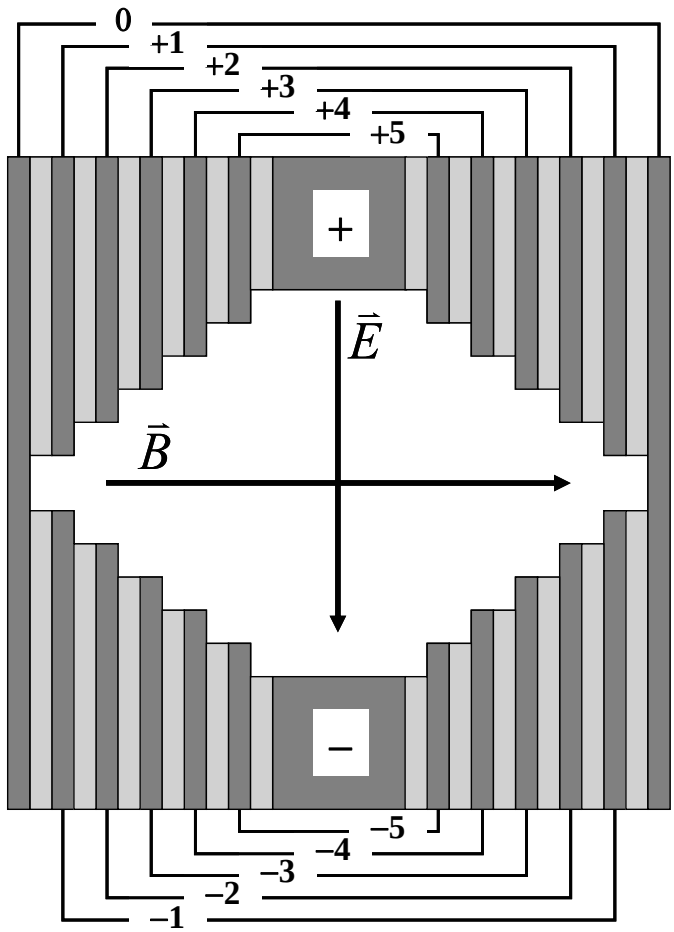

Figure 2.5 Construction of the Wien filter electric field plates. Five pairs of parallel stainless steel shims on each side (+ and –) and two electrodes (dark grey) have voltages distributed to give a vertical electric field equivalent to infinite parallel plates. Teflon shims (light grey) are placed between the stainless steel shims to insulate them from each other. The ion trajectory is into the plane of the page, and the magnetic field lines run from left to right.

There are several more ion optics following the mass selection region: a 3-element quadrupole (Q3), a short field free region, an aperture (A3), another 3-element quadrupole (Q4), a pair of deflectors (D5), and a series of deceleration lenses (DL1-DL4). The deceleration lenses slow the ions to 35V as well as focus them for interaction with a laser beam. Ions are collected in a Faraday cup and their current is measured using a Keithley 602 Electrometer. Ion currents of 1-2000 pA are achievable. Figure 2.6 illustrates the components in the final chamber of the photoelectron spectrometer which is pumped to 10^{-8} Torr (~10^{-6} Pa) by a 280 l/s Varian turbomolecular pump.

2.4 Ultraviolet Laser System

The 35 eV ion beam is intersected perpendicularly in the interaction region with a 363.8 or 351.1 nm photon beam from a continuous wave Spectra Physics 2045 Argon-Ion Laser. Before reaching the interaction region, the laser photons encounter several optical components which alter the laser light in order for the vacuum cavity to double as a power build-up cavity.[5, 6] A diagram of the laser system is given in Figure 2.7. The laser cavity itself consists of a highly reflective back mirror, an etalon, a plasma tube, and an output coupler. Operation at 363.8 or 351.1 nm is selected with the appropriate output coupler. An etalon is placed in the laser cavity to allow for operation on a single cavity mode within the 363.8 or 351.1 nm Doppler profile. The argon ion laser output power is typically ~1 W for single mode operation at 363.8 or 351.1 nm.

Several mirrors direct the laser light through a telescope where the light is focused into the interaction region. An acousto-optic modulator (AOM), piezoelectric translators (piezo) on the back mirror of the laser and front cavity window, and two photodiodes are used in a servo system which maintains the power build-up in the vacuum chamber. Power increases approximately 100 fold in the build-up cavity. A half wave plate is placed

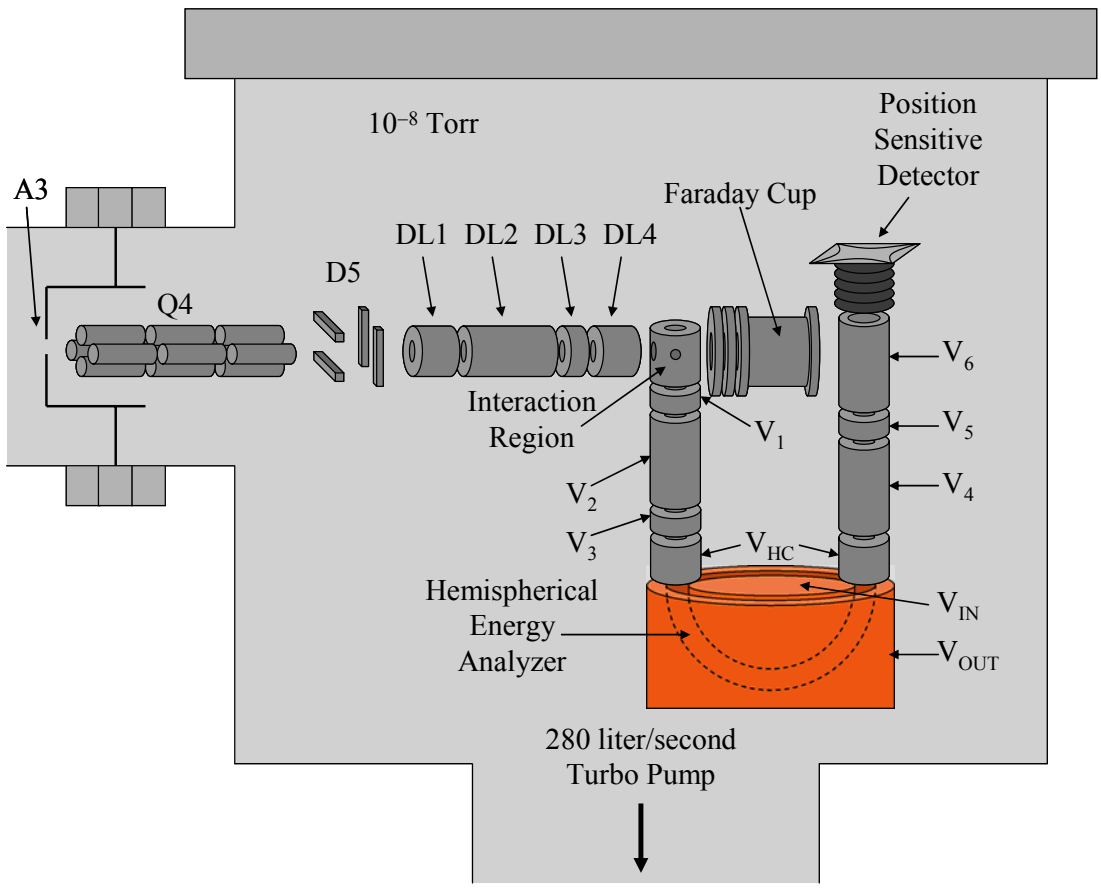

Figure 2.6 Vacuum chamber containing the final elements of the ion beam path and the electron energy analysis and detection components.

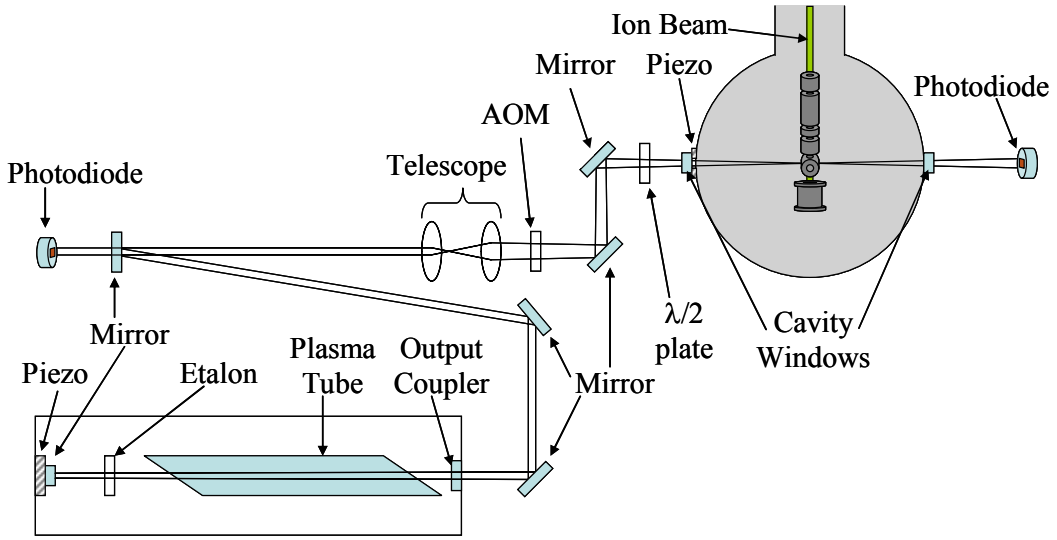

Figure 2.7 Components of the laser system. The system is made up of an argon-ion laser and the vacuum chamber serves as an external build-up cavity. The back mirror of the laser and the front cavity window are mounted on piezoelectric translators. The acousto-optic modulator (AOM), piezos, and photodiodes are part of a servo system which maintain efficient build-up within the vacuum chamber.

immediately before injection into the power build-up cavity to allow for rotation of the laser polarization within the cavity.

The build-up cavity operates similar to the laser cavity but has no gain medium. For intensity to buildup constructively within the cavity, the cavity length must be a half-integer multiple of the laser wavelength. The build-up cavity length, however, is sensitive to external factors such as thermal fluctuations, mechanical vibrations from the pumps, or acoustic noise due to the pumps or other room noise. To maintain the build-up, these fluctuations are responded to by the servo system. A direct response can be achieved by adjusting the piezos on the front cavity window which directly changes the cavity length. The piezo on the back mirror of the laser can also be used to restore the system to resonance. The piezo is used to adjust the length of the laser cavity, thereby changing the laser wavelength.

Similarly, the AOM is used to slightly change the laser wavelength/frequency. Within the AOM is a quartz crystal which is connected to an acoustic transducer. An acoustic frequency of 55-85 MHz is applied to the quartz crystal, producing a standing wave in the crystal, which acts as a Bragg diffraction grating.[7] The incoming laser beam is diffracted and the frequency of the diffracted laser light is offset by the frequency of the standing wave in the crystal. Additionally, a 1 MHz dither is added on top of the 55-85 MHz offset. The 55-85 MHz offset allows for small frequency adjustments and optically isolates the laser and build-up cavities from one another, preventing any light which reflects off the build-up cavity from returning to the laser cavity and causing interference. The 1 MHz dither serves to provide an error signal for the servo electronics, which adjust the build-up cavity piezo, laser cavity piezo, or AOM frequency offset to maintain the resonance condition of the build-up cavity. Each of the piezos and the AOM are used to respond to different frequencies of noise in the system. The slowest frequencies (0 – 100 Hz) are responded to by the piezos on the build-up cavity. The piezo on the back mirror of the laser is used to react to higher

frequency noise (100 Hz – 10 kHz). The highest frequency noise (10 kHz – 1 MHz) is dealt with by the AOM.

Depending on the state in which the system is last left, build-up may not happen on its own by simply turning on the electronics. The electronics should be left with the active stabilization turned off. Assuming the optics are aligned close enough to allow for the light to resonate within the vacuum cavity, the alignment is optimized by adjusting the telescope, the AOM tilt angle, the two mirrors immediately in front of the cavity, and the front cavity window. Next, the servo electronics are switched to active stabilization on. At this point the phase delay between the AOM and piezos can be adjusted. While monitoring the signal on the photodiode located at the back side of the vacuum chamber, the phase delay should be set to the point where the cavity is close to or even starting to have build-up occur. This is when there are the most resonances occurring. At this point, the gain for the laser piezo can be adjusted which should allow build-up to begin. The build-up can be optimized by small adjustments to the phase delay, the laser piezo gain as well as the gain on the AOM servo. Occasionally, it may be necessary to adjust the bias positions of the laser and buildup cavity piezos.

2.5 Photoelectron Energy Analysis and Detection

At the position where the ion and laser beams intersect (the interaction region) photoelectrons are ejected in all directions. A portion of the electrons are ejected in a downward direction and pass through a 5° half angle opening in the interaction region where they enter the energy analysis region of the instrument.[8] The components of the energy analyzer are pictured in Figure 2.8, which depicts a cutaway showing the path the photoelectrons take through the analyzer.

The hemispherical energy analyzer operates at a constant transmission energy, presently ~4.0 eV. Since electrons may be photodetached with kinetic energies ranging from 0 eV to the photon energy (~3.5 eV), the electrons must be accelerated before they enter the hemispherical analyzer if they are to be transmitted and detected. A series of lenses is used to accelerate and focus the incoming electrons to the proper energy and position. The electrons are first accelerated to 5-10 times their initial energy with lens elements 1 and 2. Lens elements 2, 3, and the input stack Herzog Corrector are also constructed to form a zoom lens which focus the electrons to the entrance of the hemispheres while giving them the appropriate transmission energy. Passing through the hemispherical analyzer, the electrons are spread in space, with slower electrons near the center hemisphere and faster electrons near the outer hemisphere. Electrons which are too slow or too fast collide with the hemispheres and are neutralized. Only electrons within ~2% of the transmission energy are passed through the entire analyzer. These electrons are accelerated and imaged onto a position sensitive detector using lens elements 4, 5, and 6. The position sensitive detector consists of a stack of 5 microchannel plates coupled to a resistive anode detector (Quantar Technology 3318A). The minimum detectable electron energy is approximately 0.1 eV, though the transmission of electrons slower than about 0.3 eV is significantly lower than unity due to poor transmission through the energy analyzer. Normally, electron energies smaller than 0.3 eV are not measured.

2.6 Data Collection

The position sensitive detector is wired to a position computer (Quantar 2401B) which analyzes the outputs of the resistive anode detector to determine the spatial position of a single detached electron. The position computer is attached to an oscilloscope (for real time viewing of the electron positions on the detector) as well as a PC for data collection. Since

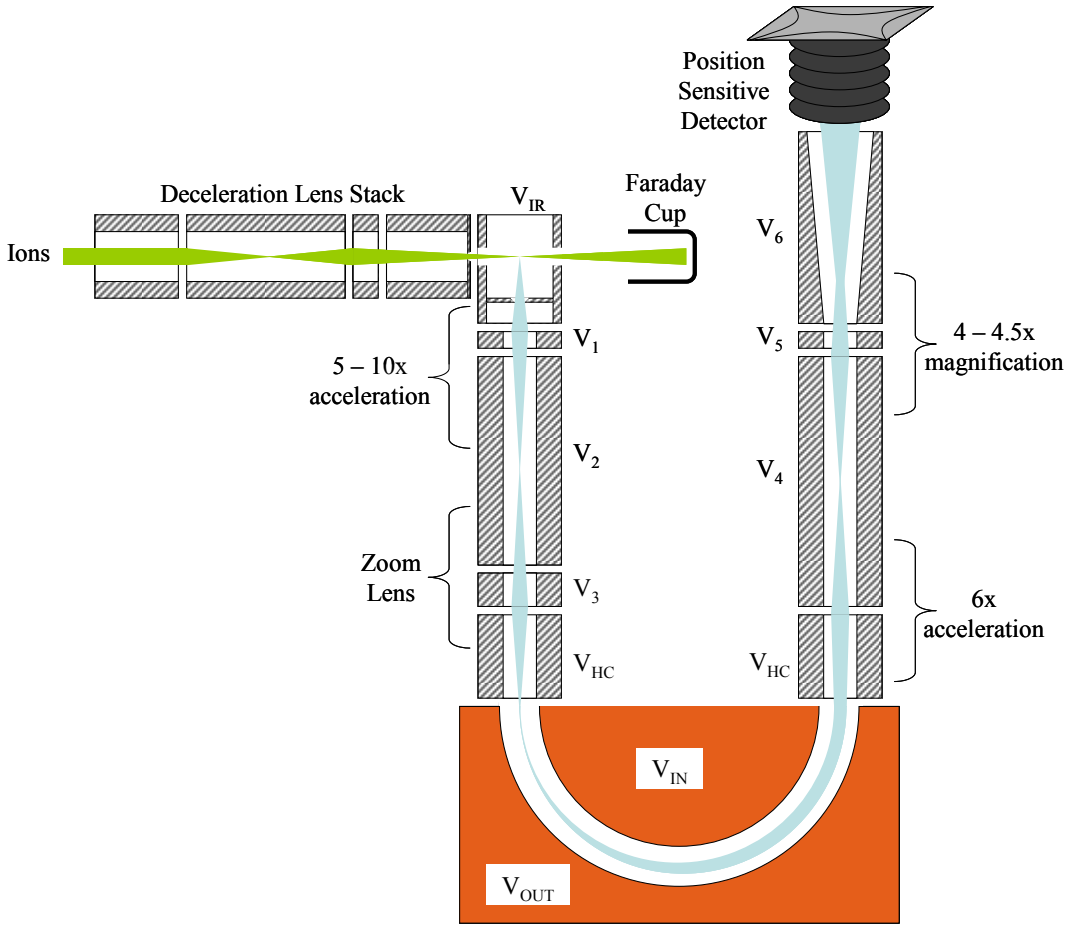

Figure 2.8 Cutaway of the electron kinetic energy analyzer system. The deceleration lenses and analyzer lenses (V_1-V_6, V_{HC}) are made from molybdenum, and the concentric hemispheres of the analyzer are made from oxygen-free high conductivity copper.

only a very small energy region (2% of the 4 eV transmission energy) is detected at a time, a LabVIEW program is used to accumulate a complete photoelectron spectrum (from 0.3 to ~3.5 eV). This program handles the process of adjusting the electron analyzer voltages to collect photoelectrons of different energies by sending out digital signals to a digital to analog encoder chip located within a voltage programmer (JILA LC036). A photoelectron spectrum is collected in LabVIEW by specifying a starting kinetic energy, total number of spectral segments, and the spacing between spectral segments.

For proper determination of the electron kinetic energy, the photoelectron spectrum of a reference ion is obtained to fix the absolute energy scale. Since it is atomic and the neutral's electron affinity[9] is precisely known (1.46111 eV), O^- is typically used for this purpose. Additionally it is usually the major precursor ion and is formed in the flow tube before and while most experiments are performed. A second calibration is performed periodically to determine any nonlinearity in the energy scale. This is done by measuring the energies of all the peaks in the tungsten anion (W^-) photoelectron spectrum and comparing with the absolute positions tabulated by Charlotte Moore.[10] A small (< 0.5%) energy compression is typically observed. One final correction to the photoelectron energies must be applied since the anions are traveling at 35 eV of kinetic energy when the electrons are detached. This correction converts the electron kinetic energies from the laboratory frame to the center of mass frame of the anions. The final electron kinetic energy can be determined by:

$$eKE = h\nu - \left[EA_{ref} + \gamma \left(eKE_{ref} - eKE_{lab} \right) + Wm_e \left(\tfrac{1}{M_{ref}} - \tfrac{1}{M} \right) \right] \tag{2.3}$$

where $h\nu$ is the photon energy, EA_{ref} is the electron affinity of the reference ion, γ is the energy compression factor, ($eKE_{ref} - eKE_{lab}$) is the lab frame difference in the kinetic energies of the reference ion and the molecule of interest, W is the kinetic energy of the ion beam, m_e

is the electron mass, M_{ref} is the mass of the reference ion, and M is the mass of the molecule of interest.

2.7 Spectral Simulation and Assignment

In order to assign and interpret the photoelectron spectra, electronic structure calculations are performed using the Gaussian suite of software.[11] Optimized molecular geometries and harmonic vibrational frequencies are obtained for each anion/neutral pair. The B3LYP[12, 13] method of Density Functional Theory[14] (DFT) is typically used with a modest basis set [6-31+G(d) or 6-311++G(d,p)]. Using these geometry and frequency results, Franck-Condon factors are obtained for the transitions between the anion and the neutral using the FCFGAUS and PESCAL programs.[15-17] The DFT calculations also allow for computation of the EA by taking the DFT energy difference between anion and neutral (including zero point energies).

The FCFGAUS program extracts the geometries, normal mode vectors, and vibrational frequencies for the anion and neutral from the Gaussian output and outputs Duschinsky rotation matrices, normal mode displacement vectors, molecular geometries, and normal mode frequencies in a form used by PESCAL. The PESCAL program computes Franck-Condon factors, treating molecular vibrations as independent harmonic oscillators and transforming the anion normal modes into linear combinations of the neutral normal modes.[15, 18-21] The raw Franck-Condon factors are convoluted with an experimental linewidth (Gaussian or Lorentzian lineshape with full width at half maximum of 8-15 meV), resulting in simulated spectrum based solely on the electronic structure calculations.

Generally, for systems free from non-adiabatic effects, the Franck-Condon simulation matches the experimental spectra quite well. This allows for precise determination of the band origin and electron affinity, and assignment of vibrational bands to the appropriate normal vibrations. These vibrational assignments typically confirm that the normal modes

whose vibrational motions occur along the geometry displacements from anion to neutral are the modes active in the photoelectron spectra.

When non-adiabatic effects are present, there will be large discrepancies between the experimental spectrum and the Franck-Condon simulation. In general, the Frank-Condon simulation will overestimate the intensities of vibrational bands in systems where non-adiabatic effects are important. Also, there may be extra vibrational bands in the experimental spectrum which are missing from the Franck-Condon simulation. This is often due to non-totally-symmetric modes appearing in the experimental spectrum which have calculated Franck-Condon factors of zero (due to symmetry). These two effects tend to offset one another in an intensity borrowing manner, where the intensity of some bands are lowered while other not normally allowed bands gain intensity. If reliable assignments can be made, photoelectron spectra showing non-adiabatic effects can yield information which is not normally anticipated, such as the frequencies of non-totally symmetric vibrations which appear in the spectrum.

2.8 Thermodynamics

For many of the systems discussed in this dissertation, thermodynamic parameters can be evaluated using thermochemical cycles. Figure 2.9 illustrates three gas-phase thermochemical cycles. Using the negative ion cycle, the electron affinity (EA) of the system of interest is combined with the enthalpy of deprotonation ($\Delta_{acid}H_0$) of the parent system and the ionization energy (*IE*) of the hydrogen atom (13.5984 eV) to determine a bond dissociation enthalpy for breaking an R—H bond (D_0):

$$D_0(\text{R—H}) = \Delta_{acid}H_0(\text{RH}) - IE(\text{H}) + \text{EA(R)} \tag{2.3}$$

Often, values for the 298 K gas phase acidity ($\Delta_{acid}G_{298}$) or deprotonation enthalpy ($\Delta_{acid}H_{298}$) are available in the literature.[22] Conversion of the 298 K deprotonation enthalpy to

0 K is achieved by considering the contributions from integrated heat capacities, which can be derived from the Gaussian output files, but are explicitly written as:

$$\Delta_{\text{acid}} H_0(\text{RH}) = \Delta_{\text{acid}} H_{298}(\text{RH}) - \int_0^{298} \text{dT}[\text{C}_\text{P}(\text{R}^-) + \text{C}_\text{P}(\text{H}^+) - \text{C}_\text{P}(\text{RH})] \tag{2.4}$$

Error bars for the thermal corrections derived from the Gaussian output files are assumed to be small, on the order of 0.1 kcal mol^{-1}.

Using these bond dissociation energies, an absolute heat of formation can be obtained for the R system if the heat of formation of the parent system is available in the literature:

$$\Delta_f H_T(\text{R}) = \Delta_f H_T(\text{RH}) + \text{D}_T(\text{RH}) - \Delta_f H_T(\text{H}) \tag{2.5}$$

where T represents the temperature in K.

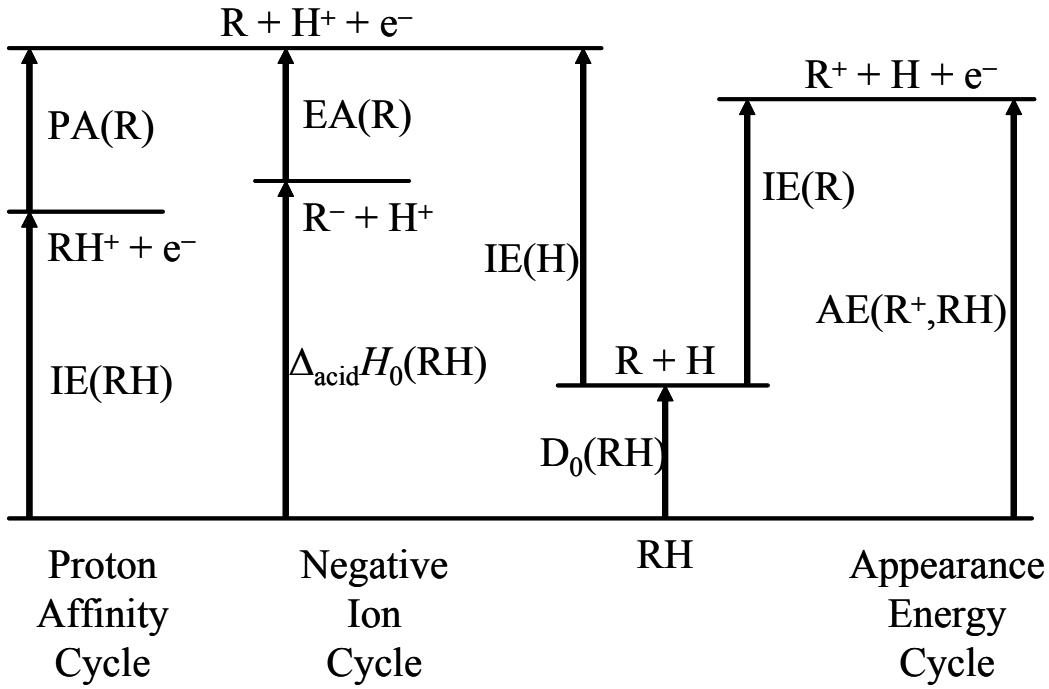

Figure 2.9 Gas-phase thermochemical cycles. The negative ion cycle combines electron affinity measurements with gas phase acidity measurements to determine R—H bond dissociation energies.

Chapter 2 References

[1] D.G. Leopold, K.K. Murray, and W.C. Lineberger, *Laser Photoelectron-Spectroscopy of Vibrationally Relaxed CH_2^- - a Reinvestigation of the Singlet Triplet Splitting in Methylene.* Journal of Chemical Physics, 1984. **81**(2): p. 1048-1050.

[2] D.G. Leopold, K.K. Murray, A.E.S. Miller, and W.C. Lineberger, *Methylene - a Study of the $X\,^3B_1$ and $^1A_1$ States by Photoelectron-Spectroscopy of CH_2^- and CD_2^-.* Journal of Chemical Physics, 1985. **83**(10): p. 4849-4865.

[3] F.C. Fehsenfeld, K.M. Evenson, and H.P. Broida, *Microwave Discharge Cavities Operating at 2450 MHz.* Review of Scientific Instruments, 1965. **36**(3): p. 294-298.

[4] M. Marynowski, W. Franzen, and M. Elbatanouny, *Analysis of the Properties of an Electrostatic Triplet Quadrupole Lens Used as an Electron-Beam Transport Device.* Review of Scientific Instruments, 1994. **65**(12): p. 3718-3723.

[5] K.M. Ervin, J. Ho, and W.C. Lineberger, *A Study of the Singlet and Triplet-States of Vinylidene by Photoelectron-Spectroscopy of $H_2C{=}C^-$, $D_2C{=}C^-$, and $HDC{=}C^-$ - Vinylidene Acetylene Isomerization.* Journal of Chemical Physics, 1989. **91**(10): p. 5974-5992.

[6] K.M. Ervin and W.C. Lineberger, *Photoelectron Spectroscopy of Negative Ions*, in *Advances in Gas Phase Ion Chemistry*, N.G. Adams and L.M. Babcock, Editors. 1992, JAI Press: Greenwich. p. 121-166.

[7] I.C. Chang, *Acousto-Optic Devices and Applications*, in *Handbook of Optics*, M. Bass, Editor. 1995, McGraw-Hill: New York. p. 12.1-12.54.

[8] C.S. Feigerle, *Ph.D. Thesis*. 1983, University of Colorado: Boulder, CO.

[9] C. Valli, C. Blondel, and C. Delsart, *Measuring electron affinities with the photodetachment microscope.* Physical Review A, 1999. **59**(5): p. 3809-3815.

[10] C.E. Moore, *Atomic Energy Levels*. NSRDS-NBS. 1952, Washington: US GPO Circular No. 467.

[11] M.J. Frisch, G.W. Trucks, H.B. Schlegel, G.E. Scuseria, M.A. Robb, J.R. Cheeseman, J.A. Montgomery, Jr. , T. Vreven, K.N. Kudin, J.C. Burant, J.M. Millam, S.S. Iyengar, J. Tomasi, V. Barone, B. Mennucci, M. Cossi, G. Scalmani, N. Rega, G.A. Petersson, H. Nakatsuji, M. Hada, M. Ehara, K. Toyota, R. Fukuda, J. Hasegama, M. Ishida, T. Nakajima, Y. Honda, O. Kitao, H. Nakai, M. Klene, X. Li, J.E. Knox, H.P. Hratchian, J.B. Cross, C. Adamo, J. Jaramillo, R. Gomperts, R.E. Stratmann, O. Yazyev, A.J. Austin, R. Cammi, C. Pomelli, J.W. Ochterski, P.Y. Ayala, K. Morokuma, G.A. Voth, P. Salvador, J.J. Dannenberg, V.G. Zakrzewski, S. Dapprich, A.D. Daniels, M.C. Strain, O. Farkas, D.K. Malick, A.D. Rabuck, K. Raghavachari, J.B. Foresman, J.V. Ortiz, Q. Cui, A.G. Baboul, S. Clifford, J. Cioslowski, B.B. Stefanov, G. Liu, A. Liashenko, P. Piskorz, I. Komaromi, R.L. Martin, D.J. Fox, T. Keith, M.A. Al-Laham, C.Y. Peng, A. Nanayakkara, M.

Challacombe, P.M.W. Gill, B. Johnson, W. Chen, M.W. Wong, C. Gonzalez, and J.A. Pople, *Gaussian 03, Revision B.05*. 2003, Gaussian, Inc.: Pittsburgh, PA.

12 C.T. Lee, W.T. Yang, and R.G. Parr, *Development of the Colle-Salvetti Correlation-Energy Formula into a Functional of the Electron-Density.* Physical Review B, 1988. **37**(2): p. 785-789.

13 A.D. Becke, *Density-Functional Thermochemistry .3. The Role of Exact Exchange.* Journal of Chemical Physics, 1993. **98**(7): p. 5648-5652.

14 R. Krishnan, J.S. Binkley, R. Seeger, and J.A. Pople, *Self-Consistent Molecular-Orbital Methods .20. Basis Set for Correlated Wave-Functions.* Journal of Chemical Physics, 1980. **72**(1): p. 650-654.

15 K.M. Ervin, T.M. Ramond, G.E. Davico, R.L. Schwartz, S.M. Casey, and W.C. Lineberger, *Naphthyl radical: Negative ion photoelectron spectroscopy, Franck-Condon simulation, and thermochemistry.* Journal of Physical Chemistry A, 2001. **105**(48): p. 10822-10831.

16 K.M. Ervin, *FCFGAUS, Fortran program*. 2003, Reno: http://www.chem.unr.edu/~ervin/pes; University of Nevada, Reno.

17 K.M. Ervin, *PESCAL, Fortran program*. 2004, Reno: http://www.chem.unr.edu/~ervin/pes; University of Nevada, Reno.

18 P. Chen, *Photoelectron Spectroscopy of Reactive Intermediates*, in *Unimolecular and Bimolecular Reaction Dynamics*, C.Y. Ng, T. Baer, and I. Powis, Editors. 1994, Wiley & Sons: New York. p. 371-425.

19 I. Ozkan, *Franck-Condon Principle for Polyatomic-Molecules - Axis-Switching Effects and Transformation of Normal Coordinates.* Journal of Molecular Spectroscopy, 1990. **139**(1): p. 147-162.

20 R. Botter, V.H. Dibeler, J.A. Walker, and H.M. Rosenstock, *Experimental and Theoretical Studies of Photoionization-Efficiency Curves for C_2H_2 and C_2D_2.* J. Chem. Phys., 1966. **44**: p. 1271-1278.

21 T.E. Sharp and H.M. Rosenstock, *Franck-Condon factors for Polyatomic Molecules.* J. Chem. Phys., 1964. **41**: p. 3453-3463.

22 J.E. Bartmess, *"Negative Ion Energetics Data"*, in *NIST Chemistry Webbook, NIST Standard Reference Database Number 69*, J.P. Linstrom and W.G. Mallard, Editors. June 2005, National Institue of Standards and Technology: Gaithersburg MD, 20899.

3 Cyclopentadienide, $C_5H_5^-$

3.1 Introduction

The cyclopentadienyl radical, C_5H_5•, has a long history. Well known as a Jahn-Teller system, cyclopentadienyl radical has been the subject of numerous theoretical investigations.[1-11] First experimentally investigated in 1956,[12] it is now recognized as an intermediate in hydrocarbon combustion and may possibly be involved in soot formation.[13-21] There have since been many experimental investigations of the cyclopentadienyl radical, including absorption,[22] electron impact ionization,[23] electron paramagnetic resonance,[24] fluorescence,[25-30] kinetics,[31] and anion photodetachment.[32] Many of these experimental and theoretical investigations have sought to extract information about the molecular structure, Jahn-Teller coupling constants, and Jahn-Teller stabilization energy, and only a few of the theoretical studies have tried to predict or interpret the experimental spectra. For this thesis, the anion photodetachment experiments were repeated with a higher energy photon (3.53 eV versus 2.54 eV) and much better photoelectron energy resolution, in order to obtain a more precise EA for C_5H_5• and to determine vibrational frequencies of C_5H_5•.

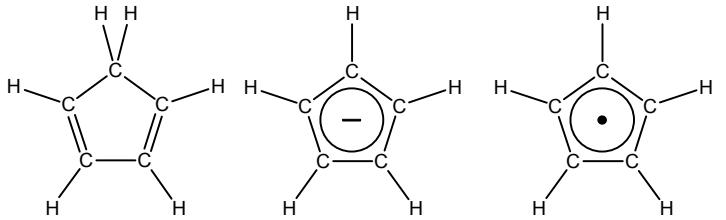

Cyclopentadiene Cyclopentadienide Cyclopentadienyl Radical

The cyclopentadienyl radical readily binds an electron in the gas phase to form cyclopentadienide ($C_5H_5^-$). Being a closed shell molecule in the D_{5h} point group, the ground state of $C_5H_5^-$ is $^1A_1'$. The highest occupied molecular orbital of $C_5H_5^-$ is doubly degenerate and has e_1'' symmetry. Logically, it follows that the ground state of C_5H_5• should be $^2E_1''$ and

be doubly degenerate. The Jahn-Teller theorem states there is at least one non-totally symmetric vibration along which the orbital energy degeneracy can be lifted.[33] The symmetric direct product of the electronic state symmetry gives the symmetry of the linear Jahn-Teller active vibrational modes which eliminate the degeneracy:

$$E_1'' \times E_1'' = A_1' + E_2' \quad (3.1)$$

Here, A_1' represents the electronic coupling symmetry and E_2' represents the Jahn-Teller mixing; the symmetry of the linearly active Jahn-Teller vibrational modes is accordingly e_2'. There are 4 doubly degenerate e_2' vibrational modes in C_5H_5•.

The photoelectron spectrum of $C_5H_5^-$ will thus represent a transition between the $^1A_1'$ ground state of $C_5H_5^-$ and the Jahn-Teller $^2E_1''$ ground state of C_5H_5•. Since there are only two vibrational modes of a_1' symmetry (i.e., totally symmetric modes) in C_5H_5, it is expected that the photoelectron spectrum will be composed of the band origin and vibrational bands corresponding to the Jahn-Teller active modes and the two totally symmetric vibrational modes.

3.2 Experiment

The cyclopentadiene dimer ($C_{10}H_{12}$, Aldrich 98%) was cracked to produce cyclopentadiene (C_5H_6) according to the literature procedure.[34] Once produced, C_5H_6 was stored under liquid nitrogen to prevent redimerization unless the sample was being used. Due to its high vapor pressure and to maintain a steady flow rate into flow tube, C_5H_6 was kept at 0 °C when in use by submersing the sample in an ice water bath. Hydroxide ions (HO^-), created using the microwave discharge ion source as described in Chapter 2, were used to deprotonate the C_5H_6 introduced downstream to create $C_5H_5^-$. Typical ion beam currents of $C_5H_5^-$ were ~300 pA. In some experiments, liquid nitrogen was used to cool the flow tube and produce vibrationally cooler ions; in these experiments, slightly smaller ion beams were

produced (~200 pA). The laser wavelength used for photodetachment of $C_5H_5^-$ was 351.1 nm and the measurement of the oxygen EA was used in calibration of the absolute energy scale.

3.3 Results

Figure 3.1 (bottom panel) shows the 351.1 nm magic angle ($\theta = 54.7°$) photoelectron spectrum of $C_5H_5^-$ taken under liquid nitrogen cooled flow tube conditions (~200 K). The room temperature spectrum shows broadening of the vibrational bands due to contributions from hot band transitions. The spectra are dominated by an intense band origin appearing at 1.812 ± 0.005 eV (labeled A), four moderately intense peaks (labeled E, F, H and I), and many small features all appearing to higher binding energy of peak A. Figure 3.1 (top panel) also shows the previously obtained photoelectron spectrum[32] of $C_5H_5^-$, where the small features are obscured by the strong band origin and poorer energy resolution.

Figure 3.2 shows the 351.1 nm photoelectron spectra of $C_5H_5^-$ taken at laser polarizations parallel ($\theta = 0°$, vertical polarization) and perpendicular ($\theta = 90°$, horizontal polarization) to the experimental photoelectron collection axis. These spectra were also obtained under liquid nitrogen cooled flow tube conditions. Values for the anisotropy parameter (β) for features in the spectrum were determined, with most features having $\beta \approx -0.9$ except several small features between peaks A and E where β lies between –0.3 and –0.7. Figure 3.3 shows an expanded view of the $\theta = 0°$ spectrum and reveals several small features which appear with only minimal relative intensity in the $\theta = 90°$ and $\theta = 54.7°$ spectra. Table 3.1 summarizes the peak positions relative to the origin.

In order to better assign the vibrational features of the photoelectron spectra, $C_5H_5^-$ and C_5H_5• geometry optimizations and frequency calculations were performed at the B3LYP/6-311++G(d,p) level of density functional theory (DFT) using the methods described

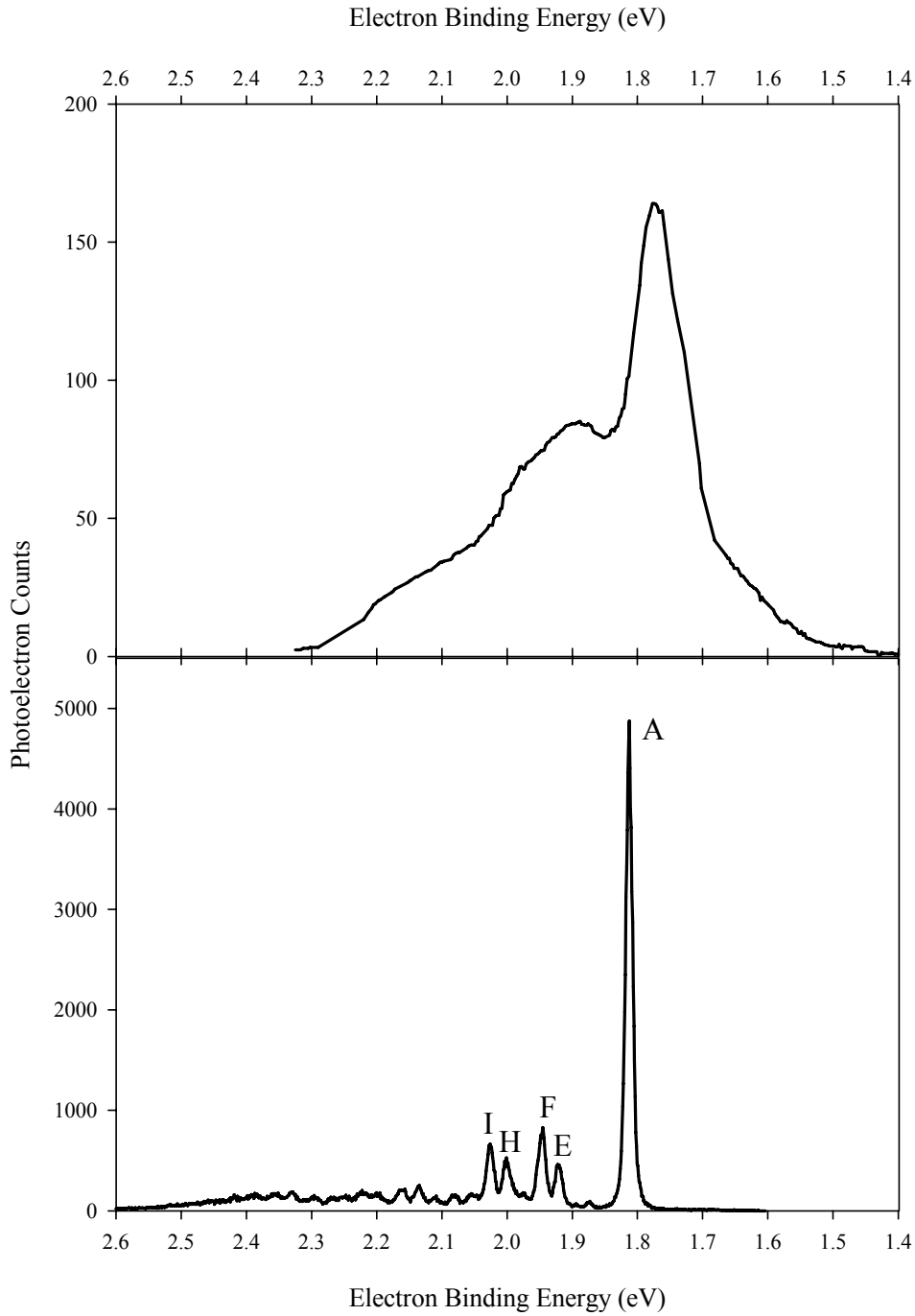

Figure 3.1 Top panel: 488.0 nm photoelectron spectrum of $C_5H_5^-$ from reference 32. Bottom panel: 351.1 nm magic angle photoelectron spectrum of $C_5H_5^-$ taken at 200 K.

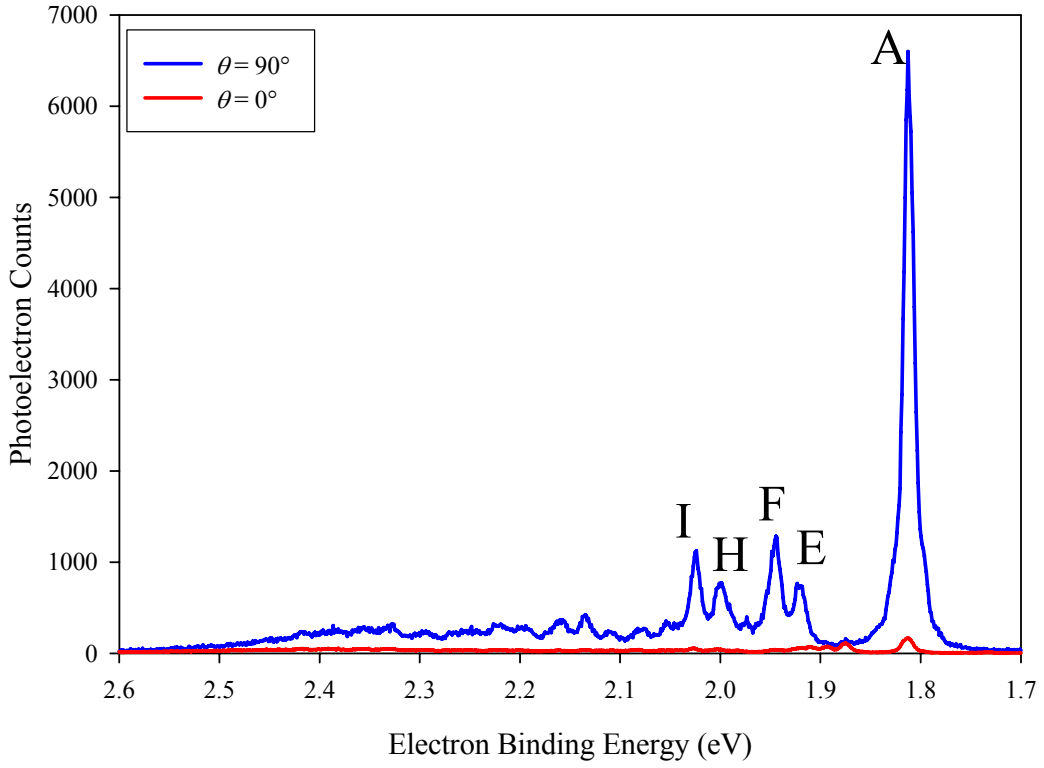

Figure 3.2 351.1 nm photoelectron spectra of $C_5H_5^-$ taken at 200 K. The red curve was obtained with the laser at vertical polarization ($\theta = 0°$), and the blue curve was obtained with the laser at horizontal polarization ($\theta = 90°$).

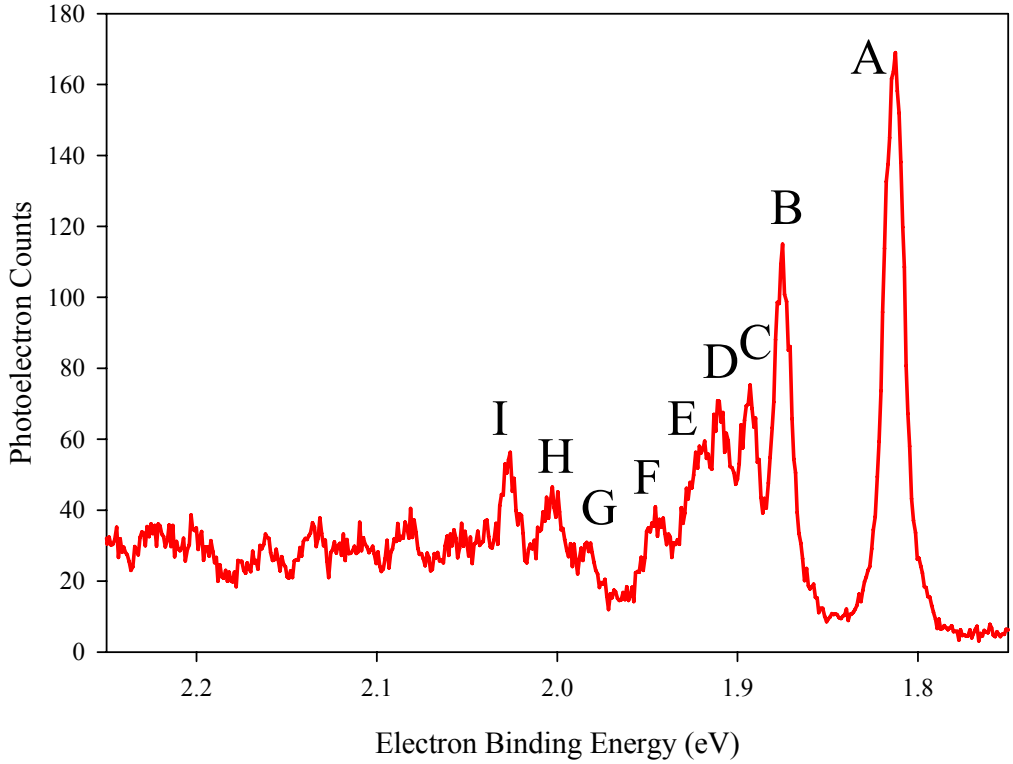

Figure 3.3 Expanded view of the 351.1 nm photoelectron spectrum of $C_5H_5^-$ taken at 200 K with the laser at vertical polarization ($\theta = 0°$).

Peak Label	Peak Position (cm^{-1})	β
A	0	–0.95 ± 0.05
B	500 ± 15 cm^{-1}	–0.35 ± 0.08
C	650 ± 30 cm^{-1}	–0.37 ± 0.08
D	790 ± 10 cm^{-1}	–0.68 ± 0.15
E	890 ± 15 cm^{-1}	–0.88 ± 0.05
F	1080 ± 10 cm^{-1}	–0.94 ± 0.05
G	1325 ± 35 cm^{-1}	–0.89 ± 0.05
H	1520 ± 15 cm^{-1}	–0.91 ± 0.05
I	1720 ± 15 cm^{-1}	–0.92 ± 0.05

Table 3.1 Relative experimental peak positions and anisotropy parameters for peaks appearing in Figures 3.1 - 3.3.

in Chapter 2. Table 3.2 lists the $C_5H_5^-$ vibrational frequencies obtained from this calculation and Table 3.3 lists the $C_5H_5^-$ molecular geometry.

DFT geometry optimization of C_5H_5• fails to converge when constrained to D_{5h} symmetry, presumably because of the Jahn-Teller effect. The symmetry of the neutral system is lowered from D_{5h} to C_{2v} by displacement along the e_2' Jahn-Teller active normal modes. Lowering of the symmetry results in the degenerate $^2E_1''$ state transforming into $^2A_2$ and $^2B_1$ states in the C_{2v} point group. It has been shown that for C_5H_5• there is no quadratic Jahn-Teller mixing.[6] This lack of quadratic mixing causes the resulting lower symmetry states to energetically relax by the same amount from the symmetric D_{5h} point, resulting in degenerate, but displaced, $^2A_2$ and $^2B_1$ states.

Geometry optimizations and frequency calculations on these C_{2v} states were performed at the B3LYP/6-311++G(d,p) level and are summarized in Tables 3.3 and 3.4. Stationary points were located for both A_2 and B_1 electronic symmetries. These states were not found to be exactly degenerate at this level of theory; the $^2A_2$ state was found to be lower by ~0.00095 eV.

In order to make qualitative assignments of the photoelectron spectra, Franck-Condon simulations were carried out, as outlined in Chapter 2, using the results from the D_{5h} anion and C_{2v} neutrals. The results are presented in Figure 3.4. The origin positions and intensities of the Franck-Condon simulations were adjusted to match the experimental EA and origin intensity. Additionally, the C_{2v} stationary points each had a single vibrational mode of b_2 symmetry with a low frequency (~65 cm^{-1}) which was omitted from the simulation. These modes should correspond to the low barrier and nearly flat pseudorotation coordinate which transforms C_5H_5• between $^2A_2$ and $^2B_1$.

From the simulations in Figure 3.4, it is clear that the intensities of most vibrational bands are overestimated, while the intensities of a few others are underestimated. However,

Mode	Nuclear Motions	Frequency (cm^{-1})	Symmetry
ν_1	C—H stretch	3174	a_1'
ν_2	C—C stretch	1143	a_1'
ν_3	In plane C—H bend	1271	a_2'
ν_4	Out of plane C—H bend	636	a_2''
ν_5	In plane C—H stretch	3152	e_1'
ν_6	In plane ring distortion	1455	e_1'
ν_7	In plane C—H bend	1013	e_1'
ν_8	Out of plane C—H bend	602	e_1''
ν_9	In plane C—H stretch	3128	e_2'
ν_{10}	In plane ring distortion	1370	e_2'
ν_{11}	In plane C—H bend	1058	e_2'
ν_{12}	In plane ring bend	846	e_2'
ν_{13}	Out of plane C—H bend	744	e_2''
ν_{14}	Out of plane ring bend	613	e_2''

Table 3.2 $C_5H_5^-$ fundamental vibrational frequencies obtained from B3LYP/6-311++G(d,p) calculations.

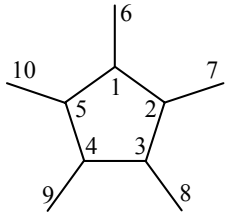	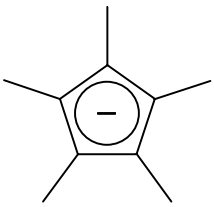	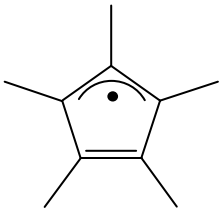	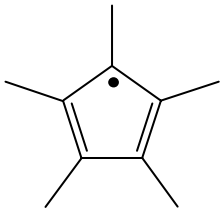
Point Group	D_{5h}	C_{2v}	C_{2v}
Electronic State	$^1A_1'$	$^2A_2$	$^2B_1$
C—C Bonds (Å) 1-2	1.4153	1.3981	1.4364
2-3	1.4153	1.4692	1.3692
3-4	1.4153	1.3585	1.4821
C—H Bonds (Å) 1-6	1.0855	1.0796	1.0828
2-7	1.0855	1.0824	1.0798
3-8	1.0855	1.0805	1.0815
∠CCC (°) 1-2-3	108.00	108.77	107.28
2-3-4	108.00	107.66	108.23
5-1-2	108.00	107.15	108.99
∠HCC (°) 6-1-2	126.00	126.43	125.50
7-2-3	126.00	125.01	127.08
8-3-4	126.00	127.27	124.85

Table 3.3 $C_5H_5^-$ and C_5H_5• geometries obtained from B3LYP/6-311++G(d,p) calculations.

Mode	Nuclear Motions	Symmetry	$^2A_2$ Frequency (cm^{-1})	$^2B_1$ Frequency (cm^{-1})
ν_1	C—H stretch	a_1	3240	3239
ν_2	C—H stretch	a_1	3232	3216
ν_3	C—H stretch	a_1	3201	3200
ν_4	C—C stretch + C—H bend	a_1	1565	1485
ν_5	C—C stretch + C—H bend	a_1	1443	1385
ν_6	Ring breathing	a_1	1142	1142
ν_7	C—C stretch	a_1	1081	1058
ν_8	C—C stretch	a_1	1033	944
ν_9	In plane C-C-C bend	a_1	847	846
ν_{10}	Out of plane C—H bend	a_2	908	901
ν_{11}	Out of plane C—H bend	a_2	819	721
ν_{12}	Out of plane C—H bend	a_2	524	514
ν_{13}	Out of plane C—H bend	b_1	886	894
ν_{14}	Out of plane C—H bend	b_1	723	819
ν_{15}	Out of plane C—H bend	b_1	678	679
ν_{16}	Out of plane C—H bend	b_1	489	499
ν_{17}	C—H stretch	b_2	3216	3232
ν_{18}	C—H stretch	b_2	3202	3204
ν_{19}	In plane C—H bend	b_2	1395	1528
ν_{20}	In plane C—H bend	b_2	1294	1295
ν_{21}	In plane C—H bend	b_2	1215	1217
ν_{22}	In plane C—H bend	b_2	968	1071
ν_{23}	In plane C—H bend	b_2	920	928
ν_{24}	In plane ring distortion	b_2	69	60

Table 3.4 C_5H_5• fundamental vibrational frequencies obtained from B3LYP/6-311++G(d,p) calculations.

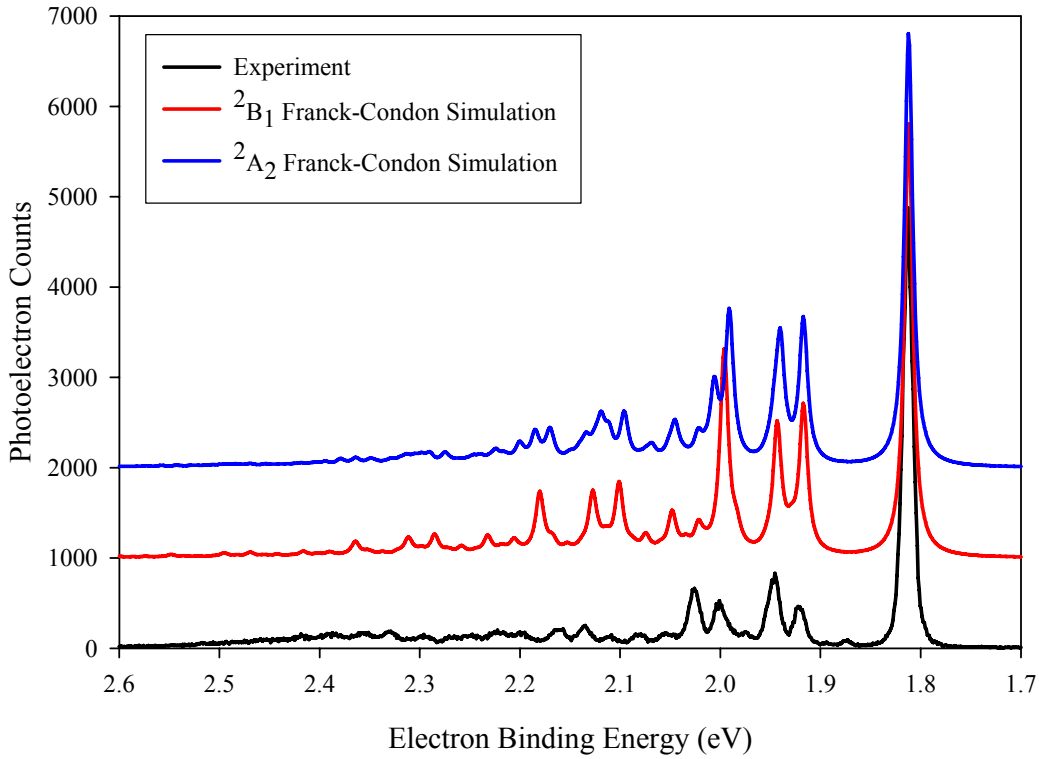

Figure 3.4 351.1 nm magic angle photoelectron spectrum of $C_5H_5^-$ taken at 200 K (black) and Franck-Condon simulations of detachment of $^1A_1'$ $C_5H_5^-$ to $^2A_2$ (blue) and $^2B_1$ (red) C_5H_5•.

this is not totally unexpected, since the Franck-Condon simulation was performed assuming the $^2A_2$ and $^2B_1$ states are stationary points, that the vibrational modes are harmonic oscillators, and that the system is free from non-adiabatic effects. These assumptions do not necessarily describe the C_5H_5• system well.

Despite these inconsistencies, several conclusions can be drawn from the simulations. It is clear which peak corresponds to the band origin and that the strong features in the experimental spectrum most likely correspond to totally symmetric (a_1) vibrations within the C_{2v} point group. In D_{5h}, these modes have a_1', e_1', or e_2' symmetry. Additionally, it can be concluded that the actual geometry displacements in the detachment must be smaller than the DFT calculations predict. This would result in more of the intensity appearing in the origin peak, as experimentally observed. Careful examination of the simulated Franck-Condon factors and the DFT vibrational frequencies of C_5H_5•, coupled with a comparison between the DFT computed vibrational motions of $C_5H_5^-$ and C_5H_5•, reveal that the vibrational modes appearing in the photoelectron spectrum are primarily due the Jahn-Teller active modes (e_2'). Although they are allowed, the two totally symmetric (a_1') modes do not appear in the Franck-Condon simulations with significant intensity.

3.4 Discussion

The peak labeled A in Figures 3.1-3.3 is identified as the C_5H_5• $\tilde{X}\,^2E_1'' \leftarrow C_5H_5^-$ $\tilde{X}\,^1A_1'$ band origin. The binding energy of this peak corresponds to the electron affinity of C_5H_5•, 1.812 ± 0.005 eV. Considering the discrepancies between the experimental spectra and the Franck-Condon simulations, unambiguous assignment of the vibrational features observed here requires further analysis.

Previously,[32] the EA of C_5H_5• was assigned as 1.786 ± 0.020 eV and an 800 ± 40 cm^{-1} vibration was observed and assigned to the totally symmetric mode (a_1') of D_{5h} C_5H_5•. This assignment was based on the 983 cm^{-1} totally symmetric mode observed in $K^+(C_5H_5^-)$.

Considering the smallest $C_5H_5^-$ a_1' DFT vibrational frequency is 1143 cm^{-1} and the corresponding a_1 frequency in both $^2A_2$ and $^2B_1$ C_5H_5• is 1142 cm^{-1}, this peak must be reassigned. This feature must correspond to the vibration of 890 ± 15 cm^{-1} observed here, which is attributed to a Jahn-Teller active mode. A vibrational frequency of 1170 ± 40 cm^{-1} was also observed previously. This most likely corresponds to the vibration of 1080 ± 10 cm^{-1} observed here. Finally, a vibrational frequency of 1690 ± 40 cm^{-1} was previously observed in the photoelectron spectrum of $C_5H_5^-$, which must correspond to the 1520 ± 15 and 1720 ± 15 cm^{-1} vibrations observed here.

Additional simulations which include non-adiabatic effects are currently underway;[35] without these simulations, definitive assignment of the majority of the smaller features observed in the photoelectron spectra presented here is difficult. However, based on the Franck-Condon simulation results the following tentative assignments are made: the peak labeled E in Figures 3.1-3.3 corresponds to one quantum of ν_9 in $^2A_2$ or $^2B_1$ C_5H_5•; the peak labeled F corresponds to one quantum of ν_8 in $^2A_2$ or one quantum of ν_7 in $^2B_1$; the peak labeled H corresponds to one quantum of ν_5 in $^2A_2$ or one quantum of ν_4 in $^2B_1$.

Alternatively, the frequencies observed here can be compared with those observed in other experiments to allow for more reliable assignments. In their recent laser induced fluorescence measurements,[6, 30] Miller et al. observed many of the fundamental vibrational frequencies of C_5H_5•. In particular, they observed a single a_1' mode of 1071 cm^{-1} and three of the four e_2' modes of 1320, 1041, and 872 cm^{-1}. They also observed a_2', and e_1' modes of 1244 and 1001 cm^{-1}, respectively. Overtones of the a_2'', e_1'', and two e_2'' modes were also observed and their frequencies were halved to obtain fundamental frequencies of 681, 766, 861, and 576 cm^{-1}, respectively. These frequencies all compare reasonably well with those obtained for $C_5H_5^-$ from the DFT calculations (Table 3.2).

Although the photoelectron spectrum is expected to be composed of the origin band and vibrational features corresponding to only totally symmetric (a_1') and Jahn-Teller active (e_2') modes, it is possible for other vibrational modes to appear in the photoelectron spectrum since overtones of non-totally symmetric modes are explicitly allowed. Fundamentals are also vibronically allowed and can often be seen if off-diagonal coupling is strong. Considering that Miller et al. observed fundamentals of forbidden modes, it is likely that off-diagonal coupling in C_5H_5• is strong enough to induce appearance of these modes in the photoelectron spectrum. Considering this and the above observations, assignments of the bands labeled in Figures 3.1-3.3 are made in Table 3.5. Peaks H and I are not assigned here but are most likely overtones of peaks E and F with strong anharmonicity.

The EA determined for C_5H_5• can be used to obtain the C—H bond dissociation energy (D_0) of C_5H_6 using the methods outlined in Chapter 2. Literature values[36] for the 298 K deprotonation enthalpy and heat of formation of C_5H_6 are 353.9 ± 2.2 and 33.2 kcal mol^{-1}. Using thermodynamic information from Gaussian output files and Equation 2.3, $D_0(C_5H_5—H)$ = 80.6 ± 2.3 kcal mol^{-1}. Assuming an error bar of ± 1.0 kcal mol^{-1} for the C_5H_6 heat of formation, the heat of formation of C_5H_5• can be determined from Equations 2.4 and 2.5, $\Delta_f H_{298}(C_5H_5•)$ = 64.6 ± 2.7 kcal mol^{-1}.

3.5 Conclusion

The $C_5H_5^-$ photoelectron spectra presented here suggest only the slightest change in the molecular structure upon photodetachment, resulting in a spectrum dominated by an intense origin peak. Considering that the Jahn-Teller modes will be significantly anharmonic and possibly have extensive mixing, it is difficult to make assignments of the vibrational features without performing additional simulations which include non-adiabatic effects. These simulations are currently underway.[35] Regardless of these difficulties, the EA of C_5H_5•

is unequivocally assigned as 1.812 ± 0.005 eV and many of the vibrational features observed in the photoelectron spectrum have been assigned to modes of $^2E_1''$ C_5H_5•.

Mode	Nuclear Motions	Label in Figures 3.1-3.3	Observed Frequency (cm^{-1})	Symmetry
ν_1	C—H stretch	—	*	a_1'
ν_2	C—C stretch	—	*	a_1'
ν_3	In plane C—H bend	—	*	a_2'
ν_4	Out of plane C—H bend	C	650 ± 30	a_2''
ν_5	In plane C—H stretch	—	*	e_1'
ν_6	In plane ring distortion	—	*	e_1'
ν_7	In plane C—H bend	—	*	e_1'
ν_8	Out of plane C—H bend	D	790 ± 10	e_1''
ν_9	In plane C—H stretch	—	*	e_2'
ν_{10}	In plane ring distortion	G	1325 ± 35	e_2'
ν_{11}	In plane C—H bend	F	1080 ± 10	e_2'
ν_{12}	In plane ring bend	E	890 ± 15	e_2'
ν_{13}	Out of plane C—H bend	—	*	e_2''
ν_{14}	Out of plane ring bend	B	500 ± 15	e_2''

* These vibrational modes were not observed in the photoelectron spectrum.

Table 3.5 Assignments of C_5H_5• vibrational features observed in the photoelectron spectrum of $C_5H_5^-$.

Chapter 3 References

[1] W.D. Hobey and A.D. McLachlan, *Dynamical Jahn-Teller effect in hydrocarbon radicals.* Journal of Chemical Physics, 1960. **33**: p. 1695-1703.

[2] L.C. Snyder, *Jahn-Teller distortions in cyclobutadiene, cyclopentadienyl radical, and benzene positive and negative ions.* Journal of Chemical Physics, 1960. **33**: p. 619-621.

[3] W.T. Borden and E.R. Davidson, *Potential Surfaces for the Planar Cyclopentadienyl Radical and Cation.* Journal of the American Chemical Society, 1979. **101**(14): p. 3771-3775.

[4] R. Meyer, F. Graf, T.K. Ha, and H.H. Gunthard, *Jahn-Teller Effect in Cyclopentadienyl Radical - Delocalized Vibronic Valence Isomerization.* Chemical Physics Letters, 1979. **66**(1): p. 65-71.

[5] M.J. Bearpark, M.A. Robb, and N. Yamamoto, *A CASSCF study of the cyclopentadienyl radical: conical intersections and the Jahn-Teller effect.* Spectrochimica Acta Part A - Molecular and Biomolecular Spectroscopy, 1999. **55**(3): p. 639-646.

[6] B.E. Applegate, T.A. Miller, and T.A. Barckholtz, *The Jahn-Teller and related effects in the cyclopentadienyl radical. I. The ab initio calculation of spectroscopically observable parameters.* Journal of Chemical Physics, 2001. **114**(11): p. 4855-4868.

[7] J.H. Kiefer, R.S. Tranter, H. Wang, and A.F. Wagner, *Thermodynamic functions for the cyclopentadienyl radical: The effect of Jahn-Teller distortion.* International Journal of Chemical Kinetics, 2001. **33**(12): p. 834-845.

[8] T.L. Nguyen, T.N. Le, and A.M. Mebel, *Thermochemistry of cyclopentadienylidene (c-C_5H_4, C_{2v}, $^3B_1$), cyclopentadienyl radical (c-C_5H_5•, C_{2v}, $^2B_1$) and 1,3-cyclopentadiene (c-C_5H_6, C_{2v}, $^1A_1$): a theoretical study by the G2M(RCC,MP2) method.* Journal of Physical Organic Chemistry, 2001. **14**(3): p. 131-138.

[9] G. Katzer and A.F. Sax, *Numerical determination of pseudorotation constants.* Journal of Chemical Physics, 2002. **117**(18): p. 8219-8228.

[10] S. Zilberg and Y. Haas, *A valence bond analysis of electronic degeneracies in Jahn-Teller systems: Low-lying states of the cyclopentadienyl radical and cation.* Journal of the American Chemical Society, 2002. **124**(36): p. 10683-10691.

[11] T. Sato, K. Tokunaga, and K. Tanaka, *Vibronic coupling in cyclopentadienyl radical: A method for calculation of vibronic coupling constant and vibronic coupling density analysis.* Journal of Chemical Physics, 2006. **124**(2). 024314.

[12] B.A. Thrush, *Spectrum of the cyclopentadienyl radical.* Nature, 1956. **178**: p. 155-156.

[13] G. Bermudez and L. Pfefferle, *Laser Ionization Time-of-Flight Mass-Spectrometry Combined with Residual-Gas Analysis for the Investigation of Moderate Temperature Benzene Oxidation.* Combustion and Flame, 1995. **100**(1-2): p. 41-51.

[14] M.J. Fadden, C. Barckholtz, and C.M. Hadad, *Computational study of the unimolecular decomposition pathways of phenylperoxy radical.* Journal of Physical Chemistry A, 2000. **104**(13): p. 3004-3011.

[15] M.J. Fadden and C.M. Hadad, *Unimolecular decomposition of the 2-oxepinoxy radical: A key seven-membered ring intermediate in the thermal oxidation of benzene.* Journal of Physical Chemistry A, 2000. **104**(34): p. 8121-8130.

[16] A. D'Anna, A. D'Alessio, and J. Kent, *A computational study of hydrocarbon growth and the formation of aromatics in coflowing laminar diffusion flames of ethylene.* Combustion and Flame, 2001. **125**(3): p. 1196-1206.

[17] D. Hodgson, H.Y. Zhang, M.R. Nimlos, and J.T. McKinnon, *Quantum chemical and RRKM investigation of the elementary channels of the reaction $C_6H_6+O(^3P)$.* Journal of Physical Chemistry A, 2001. **105**(17): p. 4316-4327.

[18] N. Kunioshi, M. Touda, and S. Fukutani, *Computational study on the formation of five-membered rings in PAH through reaction with O_2.* Combustion and Flame, 2002. **128**(3): p. 292-300.

[19] C.S. McEnally and L.D. PFefferle, *The effects of slight premixing on fuel decomposition and hydrocarbon growth in benzene-doped methane nonpremixed flames.* Combustion and Flame, 2002. **129**(3): p. 305-323.

[20] D.M. Matheu, A.M. Dean, J.M. Grenda, and W.H. Green, *Mechanism generation with integrated pressure dependence: A new model for methane pyrolysis.* Journal of Physical Chemistry A, 2003. **107**(41): p. 8552-8565.

[21] M.S. Skjoth-Rasmussen, P. Glarborg, M. Ostberg, J.T. Johannessen, H. Livbjerg, A.D. Jensen, and T.S. Christensen, *Formation of polycyclic aromatic hydrocarbons and soot in fuel-rich oxidation of methane in a laminar flow reactor.* Combustion and Flame, 2004. **136**(1-2): p. 91-128.

[22] R. Engleman and D.A. Ramsay, *Electronic Absorption Spectrum of Cyclopentadienyl Radical (C_5H_5) and Its Deuterated Derivatives.* Canadian Journal of Physics, 1970. **48**(8): p. 964-969.

[23] A.G. Harrison, L.R. Honnen, H.J. Dauben, Jr., and F.P. Lossing, *Free Radicals by Mass Spectrometry. XX. Ionization Potentials of Cyclopentadienyl and Cycloheptatrienyl Radicals.* Journal of the American Chemical Society, 1960. **82**(21): p. 5593-5598.

[24] G.R. Liebling and H.M. McConnell, *Study of molecular orbital degeneracy in C_5H_5.* Journal of Chemical Physics, 1965. **42**(11): p. 3931-3934.

[25] H.H. Nelson, L. Pasternack, and J.R. Mcdonald, *Excitation and Emission-Spectra of the $^2A_2'' \leftrightarrow {}^2E_1''$ System of the Gas-Phase Cyclopentadienyl Radical.* Chemical Physics, 1983. **74**(2): p. 227-237.

[26] L. Yu, S.C. Foster, J.M. Williamson, M.C. Heaven, and T.A. Miller, *Rotationally Resolved Electronic-Spectrum of Jet-Cooled Cyclopentadienyl Radical.* Journal of Physical Chemistry, 1988. **92**(15): p. 4263-4266.

[27] L. Yu, J.M. Williamson, and T.A. Miller, *Rotationally Resolved Electronic-Spectrum of Jet-Cooled Deuterated Cyclopentadienyl Radical.* Chemical Physics Letters, 1989. **162**(6): p. 431-436.

[28] L.A. Yu, D.W. Cullin, J.M. Williamson, and T.A. Miller, *High-Resolution Laser Spectroscopy of Asymmetrically Deuterated Cyclopentadienyl Radicals - a Study of Vibronic Degeneracy Resolution and Jahn-Teller Distortion.* Journal of Chemical Physics, 1993. **98**(4): p. 2682-2698.

[29] S. Sun and E.R. Bernstein, *Vibronic Structure of the Cyclopentadienyl Radical and Its Nonrigid Van-Der-Waals Cluster with Nitrogen.* Journal of Chemical Physics, 1995. **103**(11): p. 4447-4454.

[30] B.E. Applegate, A.J. Bezant, and T.A. Miller, *The Jahn-Teller and related effects in the cyclopentadienyl radical. II. Vibrational analysis of the $A\ ^2A_2''$ - $X\ ^2E_1''$ electronic transition.* Journal of Chemical Physics, 2001. **114**(11): p. 4869-4882.

[31] K. Roy, M. Braun-Unkhoff, P. Frank, and T. Just, *Kinetics of the cyclopentadiene decay and the recombination of cyclopentadienyl radicals with H-atoms: Enthalpy of formation of the cyclopentadienyl radical.* International Journal of Chemical Kinetics, 2002. **34**(3): p. 209-222.

[32] P.C. Engelking and W.C. Lineberger, *Laser Photoelectron Spectrometry of $C_5H_5^-$ - Determination of Electron-Affinity and Jahn-Teller Coupling in Cyclopentadienyl.* Journal of Chemical Physics, 1977. **67**(4): p. 1412-1417.

[33] H.A. Jahn and E. Teller, *Stability of polyatomic molecules in degenerate electronic states. I. Orbital degeneracy.* Proc. R. Soc. (London), 1937. **A161**: p. 220-235.

[34] R.B. Moffett, *Cyclopentadiene and 3-chlorocyclopentene.* Organic Syntheses, 1952. **32**: p. 41-44.

[35] T. Ichino, A.J. Gianola, W.C. Lineberger, and J.F. Stanton, *Manuscript in preparation.*

[36] J.E. Bartmess, *"Negative Ion Energetics Data"*, in *NIST Chemistry Webbook, NIST Standard Reference Database Number 69*, J.P. Linstrom and W.G. Mallard, Editors. June 2005, National Institue of Standards and Technology: Gaithersburg MD, 20899.

4 Pyrrolide, $C_4H_4N^-$

4.1 Introduction

Substitution of an N—H group for the CH_2 group in cyclopentadiene results in the pyrrole molecule (C_4H_5N) which is isoelectronic with cyclopentadiene. The analogous deprotonated anions, pyrrolide ($C_4H_4N^-$) and cyclopentadienide, are isoelectronic with each other. The corresponding neutrals, the pyrrolyl radical and the cyclopentadienyl radical, are also isoelectronic with one another. In addition, the substitution lowers the symmetry from D_{5h} to C_{2v}. Considering this, it is surprising that there have been few studies on pyrrolyl as a perturbation to the cyclopentadienyl system.[1]

Photodetachment of pyrrolide has been reported,[2] as has photoionization of pyrrole.[3] A short time ago, photofragment velocity map imaging was applied to the pyrrole system to determine the N—H bond dissociation energy (D_0) of pyrrole.[4] More recently, H Rydberg atom photofragment translational spectroscopy was employed to very precisely measure the N—H bond dissociation energy of pyrrole.[5] Here, the electron affinity (EA) and the vibrational and electronic structure of the pyrrolyl radical are determined. Combining the pyrrolyl EA with the pyrrole N—H bond dissociation energy, a precise gas-phase acidity for the pyrrole molecule is obtained. The work presented here is also available as a publication[6] (*J. Phys. Chem. A*, **2004**, 108, 10326-10335).

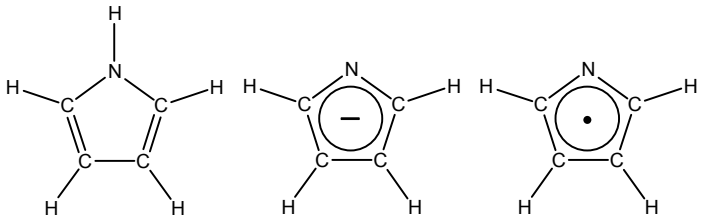

4.2 Experiment

Hydroxide ions (HO^-), created using the microwave discharge ion source as described in Chapter 2, were used to deprotonate pyrrole (Sigma, 98%), introduced downstream, to create pyrrolide. Typical pyrrolide ion beam currents were ~150 pA. In some experiments, liquid nitrogen was used to cool the flow tube and produce vibrationally cooler ions; in these experiments, slightly smaller ion beams were produced (~75 pA). The laser wavelength used for photodetachment of pyrrolide was 363.8 nm and measurement of the EA of oxygen was used to calibrate the absolute energy scale.

4.3 Results

The 363.8 nm (3.408 eV) magic-angle photoelectron spectrum of pyrrolide at ~298 K is shown in Figure 4.1. The spectrum shows a Franck-Condon envelope with at least three active vibrations. The peak at 2.145 ± 0.010 eV is assigned as the electronic band origin, corresponding to the EA of pyrrolyl. This value is close to that of 2.39 ± 0.13 eV obtained by Brauman in a very early, low-resolution threshold photodetachment measurement.[2] Three pyrrolyl vibrational frequencies are resolved in the spectrum at 925 ± 65, 1012 ± 25, and 1464 ± 20 cm^{-1} from the band origin. A weak peak at lower binding energy is identified as a pyrrolide vibrational hot-band with a frequency of 874 ± 95 cm^{-1}.

Figure 4.2 shows the 298 K photoelectron spectrum with the laser polarization parallel ($\theta = 0°$) and perpendicular ($\theta = 90°$) to the photoelectron collection axis. A value of –0.5 ± 0.1 was obtained for the anisotropy parameter, β, for the strong features in the spectrum. The β value, however, is smaller across the weak continuous portion of the spectrum (eBE > 2.5 eV), approaching zero. This variation of β suggests that the spectrum may represent electron detachment from more than one molecular orbital of pyrrolide.

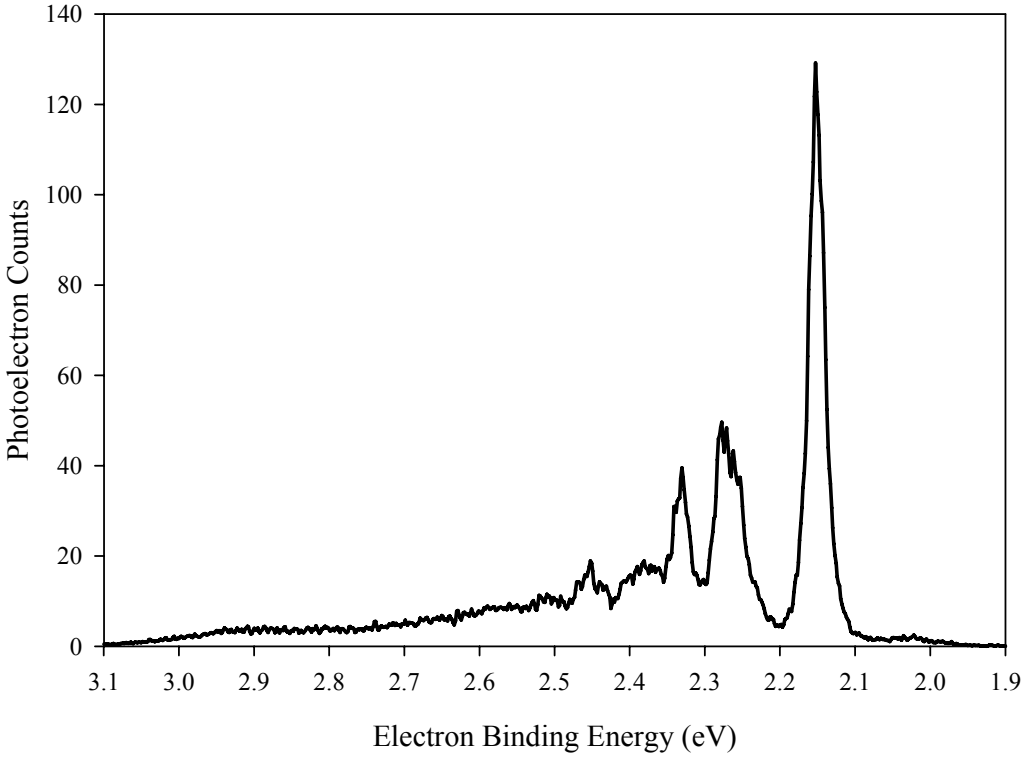

Figure 4.1 363.8 nm magic angle photoelectron spectrum of pyrrolide at 298 K.

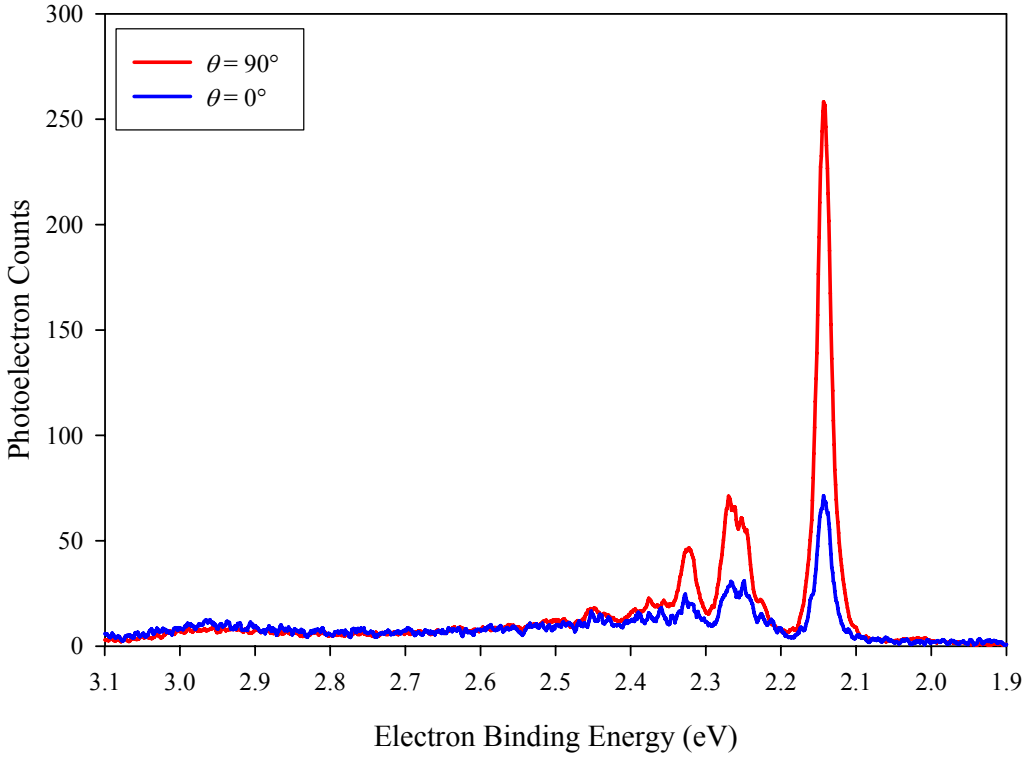

Figure 4.2 363.8 nm photoelectron spectra of pyrrolide taken at 298 K. The blue curve was obtained with the laser at vertical polarization ($\theta = 0°$), and the red curve was obtained with the laser at horizontal polarization ($\theta = 90°$).

To aid in the assignment and interpretation of the photoelectron spectra, electronic structure calculations were carried out on the pyrrole/pyrrolide/pyrrolyl system as outlined in Chapter 2. Geometry optimizations and frequency calculations were performed at the B3LYP/6-311++G(d,p) level of Density Functional Theory (DFT) for ground state pyrrolide ($^1A_1$), as well as the ground ($^2A_2$) and first excited ($^2B_1$) states of pyrrolyl. The optimized geometries for these three stationary points are listed in Table 4.1 and vibrational frequencies are listed in Table 4.2; these results compare well with a recent DFT study.[7]

The DFT calculations show that these states all have C_{2v} symmetry. Figure 4.3 depicts the highest occupied molecular orbitals of pyrrolide. Detachment of an electron from the highest occupied molecular orbital forms the ground state of pyrrolyl, which has A_2 electronic symmetry. Likewise, detachment from the second highest occupied molecular orbital forms excited state pyrrolyl, with B_2 electronic symmetry. Detachment from the $a_1(\sigma)$ orbital is inaccessible with the photon energy used in this experiment. The DFT calculations find a minimum for $^2A_2$ pyrrolyl and a transition state for $^2B_1$ pyrrolyl, as indicated by the imaginary frequency listed in Table 4.2. These two stationary points are connected via a pseudorotation path on the ground adiabatic potential energy surface.[6]

Examination of the geometries provides insight into which vibrational modes will be activated upon photodetachment. There are significant differences of the bond lengths in the ring between the anion ground state and the two states of the radical. It is therefore expected that those vibrational modes which contain significant motion along the ring coordinates will be active in the Franck-Condon profile.

Using the geometry and frequency results from the DFT calculations, Franck-Condon simulations were performed for the transitions between $^1A_1$ pyrrolide and $^2A_2$ or $^2B_1$ pyrrolyl, as outlined in Chapter 2. The simulation, depicted in Figure 4.4, assumes identical total photodetachment cross sections for the two radical states and neglects the imaginary frequency in the $^2B_1$ state. Three totally symmetric vibrational modes in each state of

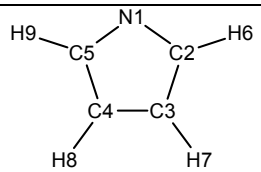		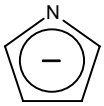	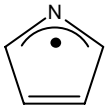	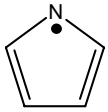
		Pyrrolide	Pyrrolyl	
Electronic State		$^1A_1$	$^2A_2$	$^2B_1$
N—C Bonds (Å)	1-2	1.3625	1.3441	1.3856
C—C Bonds (Å)	2-3	1.4035	1.4598	1.3639
	3-4	1.4195	1.3610	1.4947
C—H Bonds (Å)	2-6	1.0865	1.0834	1.0794
	3-7	1.0847	1.0798	1.0806
∠CNC (°)	5-1-2	105.13	104.74	106.84
∠NCC (°)	1-2-3	112.06	112.38	111.04
∠CCC (°)	2-3-4	105.38	105.25	105.54
∠HCN (°)	6-2-1	120.54	120.99	120.17
∠HCC (°)	7-3-2	127.20	126.26	128.29

Table 4.1 Pyrrolide and pyrrolyl geometries obtained from the B3LYP/6-311++G(d,p) calculations.

Mode	Symmetry	Pyrrolide	Pyrrolyl	
		$^1A_1$ Frequency (cm^{-1})	$^2A_2$ Frequency (cm^{-1})	$^2B_1$ Frequency (cm^{-1})
ν_1	A_1	3174	3245	3248
ν_2	A_1	3131	3201	3225
ν_3	A_1	1462	1556	1477
ν_4	A_1	1375	1433	1368
ν_5	A_1	1168	1203	1137
ν_6	A_1	1104	1090	1071
ν_7	A_1	1018	1043	936
ν_8	A_1	879	882	870
ν_9	A_2	764	904	887
ν_{10}	A_2	683	817	753
ν_{11}	A_2	608	488	505
ν_{12}	B_1	753	836	878
ν_{13}	B_1	679	710	702
ν_{14}	B_1	652	540	326
ν_{15}	B_2	3152	3226	3240
ν_{16}	B_2	3126	3197	3217
ν_{17}	B_2	1444	1355	1456
ν_{18}	B_2	1300	1293	1285
ν_{19}	B_2	1229	1079	1079
ν_{20}	B_2	1031	935	931
ν_{21}	B_2	893	817	2167*i*

Table 4.2 Pyrrolide and pyrrolyl fundamental vibrational frequencies obtained from B3LYP/6-311++G(d,p) calculations.

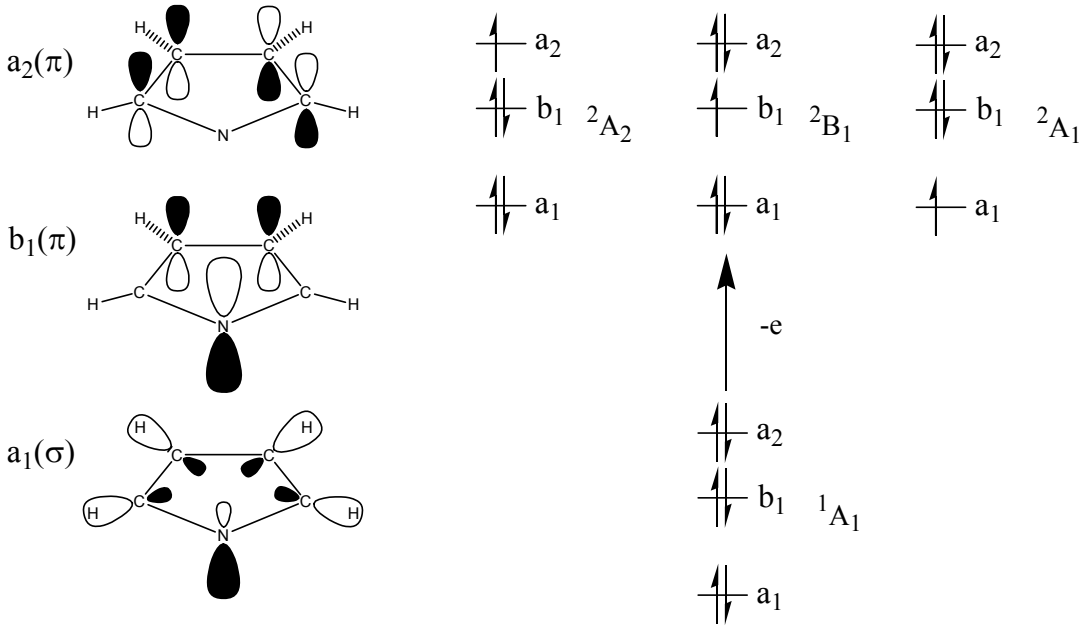

Figure 4.3 Three highest occupied molecular orbitals of pyrrolide and the schematic representation of electron photodetachment from pyrrolide to form three electronic states of pyrrolyl radical.

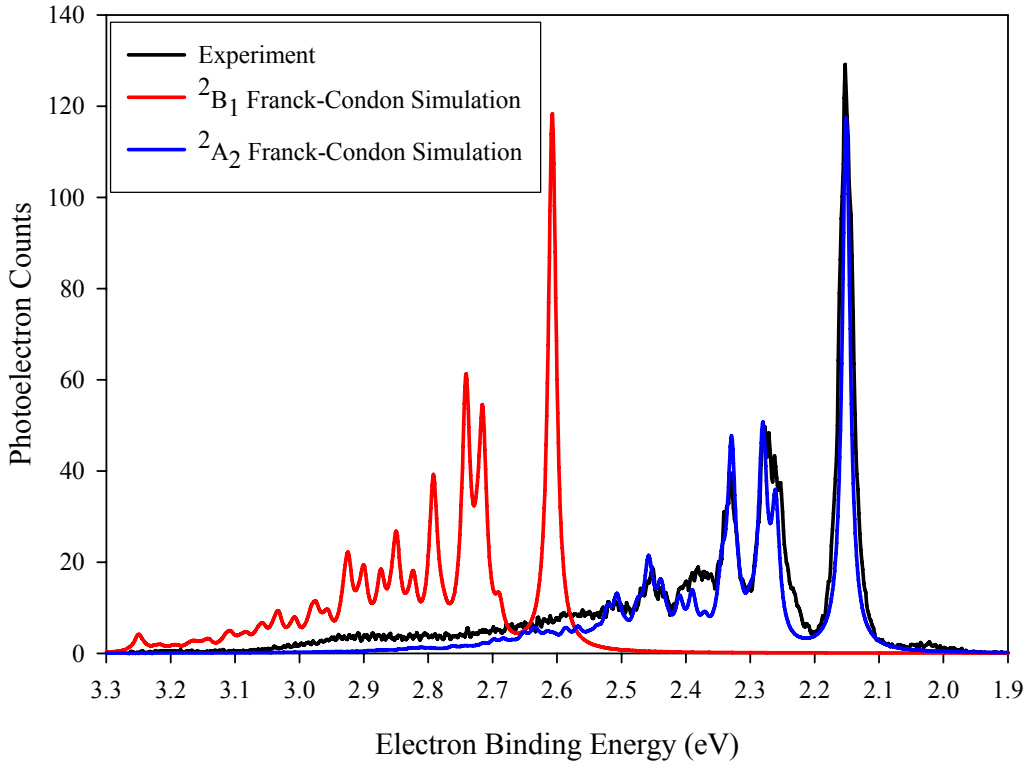

Figure 4.4 Franck-Condon simulations of detachment of $^1A_1$ pyrrolide to $^2A_2$ (blue) and $^2B_1$ (red) pyrrolyl. The binding energy for the $^2A_2$ origin peak was adjusted to match the experimental spectrum (black) while the $^2B_1$ origin peak position was adjusted to match the DFT term energy (~0.49 eV).

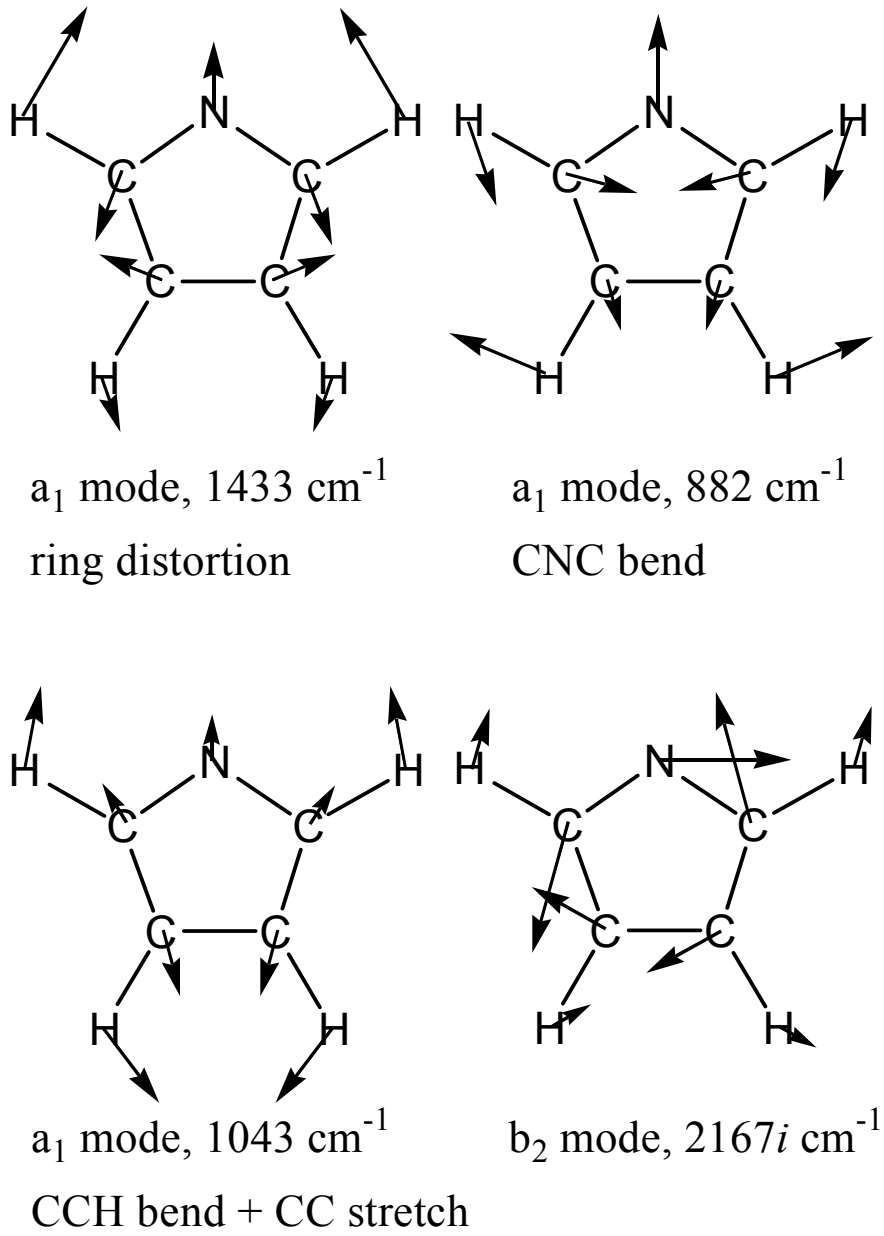

Figure 4.5 Relative atomic displacements in the normal modes for pyrrolyl radical. Three a_1 modes for the $^2A_2$ state of pyrrolyl which are active in the photoelectron spectrum, and one b_2 mode for the $^2B_1$ state of pyrrolyl which has an imaginary frequency.

pyrrolyl are determined to be active in the Franck-Condon profile; the corresponding normal mode displacements for the $^2A_2$ state are depicted in Figure 4.5. Fundamentals, overtones, and combination bands of the three active modes make up the vibrational features observed in the spectra.

Comparison between the experimental photoelectron spectrum and the Franck-Condon simulations (Figure 4.4) makes it clear that the main features in the photoelectron spectrum are due to detachment to the $^2A_2$ ground state of pyrrolyl. The DFT calculations predict a pyrrolyl EA of 2.116 eV, in excellent agreement with the experimental value of 2.145 ± 0.010 eV. The Franck-Condon analysis also predicts the $^2B_1$ state to appear in the spectrum with a term energy of 0.49 eV according to the DFT calculations. No such prominent features appear in the spectrum which can be ascribed to the $^2B_1$ state. The absence of such features must originate from the lifetime broadening along the vibrational mode with an imaginary frequency.

4.4 Discussion

The pyrrolyl radical is isoelectronic with the cyclopentadienyl radical, C_5H_5•. The highest occupied molecular orbitals in C_5H_5• are doubly degenerate, have e_1'' symmetry, and are analogous to the a_2 and b_1 orbitals illustrated in Figure 4.3. Replacement of one C—H group with a nitrogen atom converts C_5H_5• into pyrrolyl and reduces the maximum symmetry from D_{5h} to C_{2v}. As a consequence, the highest occupied molecular orbitals in pyrrolyl are no longer required by symmetry to be degenerate. Since the b_1 orbital of pyrrolyl has a large contribution from the nitrogen p orbital it will be more stable than the a_2 orbital which has a node at the nitrogen position. This will result in pyrrolyl having a ground state of $^2A_2$, as confirmed by the Franck-Condon analysis. ESR measurements of the pyrrolyl radical in aqueous solution also find a $^2A_2$ ground state.[8]

It is straightforward to rationalize the geometry change between the anion ground state and the radical ground state by recognizing the bonding character of the anion orbital from which electron detachment takes place. The a_2 orbital has bonding character between C2 and C3 and between C4 and C5, while antibonding character is found between C3 and C4 (Figure 4.3; see the figure in Table 4.1 for atom numbering). Detachment of an electron from this orbital reduces these bonding and antibonding effects. Thus, the C2—C3 and C4—C5 bonds lengthen, while the C3—C4 bond shortens upon electron detachment to form the $^2A_2$ state of the radical, as found in the DFT calculations (Table 4.1)

The anisotropy parameter (β) for the intense features assigned to the $^2A_2$ state is about –0.5. As outlined in Chapter 1, this anisotropy is consistent with electron photodetachment from a π type molecular orbital, lending additional support to the assignment made here. The observed change of the β value from –0.5 to near zero hints at contribution to the spectrum from another electronic state of pyrrolyl. Figure 4.4 shows that the Franck-Condon simulation of detachment to the $^2B_1$ state of pyrrolyl predicts a prominent, well-resolved photoelectron spectrum beginning about 0.5 eV above the ground-state origin. No such spectrum is observed, but there appears to be a weak continuum in this region.

This state is "missing" because of a large imaginary frequency at the $^2B_1$ stationary point. DFT predicts a first order transition state for the $^2B_1$ state with a single b_2 mode with a large imaginary frequency of 2167*i* cm^{-1}. All other calculated frequencies are real, with the smallest frequency being 326 cm^{-1}. The displacements for the imaginary mode are depicted in Figure 4.5. This vibration corresponds to the pseudorotation coordinate between the $^2B_1$ and $^2A_2$ stationary points. Following this coordinate from the $^2B_1$ stationary point, it is downhill in energy all the way to the $^2A_2$ potential minimum.

The magnitude of the imaginary frequency shows the steepness of the potential energy surface along this normal coordinate. The shape of the potential surface is directly

related to lifetime broadening in transition-state spectra.[9] Such a large magnitude imaginary frequency for the pyrrolyl $^2B_1$ state suggests that the spectrum would be broadened *substantially*. The Franck-Condon simulation in Figure 4.4 was performed with a full width at half maximum of 15 meV. This linewidth represents the instrument resolution and is appropriate for the $^2A_2$ ground state but not for the $^2B_1$ transition state. If the $^2B_1$ state has both substantial lifetime broadening and a photodetachment cross section comparable to the ground state, then the spectrum would appear as a weak, broad, featureless continuum, as observed. The Franck-Condon simulation for the $^2A_2$ ground state shows little intensity above 2.7 eV electron binding energy, and yet the experimental spectrum exhibits a weak tail up to about 2.1 eV, with a significantly different β value. All of these observations lead to the conclusion that the broad tail of the photoelectron spectrum above an electron binding energy of 2.6 eV reflects transitions to the $^2B_1$ state of pyrrolyl, with an intrinsic width of perhaps 0.1 eV.

The imaginary frequency of the $^2B_1$ state arises from non-adiabatic (vibronic coupling) effects with the nearby $^2A_2$ ground state. Comparing pyrrolyl with C_5H_5• may help illustrate the problem at hand. Figure 4.6 shows a qualitative picture of the adiabatic potential energy surfaces of C_5H_5• along two first-order Jahn-Teller active normal coordinates, as discussed recently by Miller et al.[10, 11] The degenerate ground states, $^2E_1''$ in D_{5h} symmetry, are subject to Jahn-Teller effects, resulting in lower symmetry (C_{2v}) stationary points which are no longer degenerate. The C_{2v} minima are connected by a pseudorotation path (the moat in Figure 4.6), and there is a small barrier along this coordinate. For pyrrolyl, the corresponding adiabatic potential energy surfaces can be drawn along a_1 and b_2 normal coordinates, as shown in Figure 4.7. The picture reflects the fact that the symmetry is reduced from D_{5h} to C_{2v}, lifting the degeneracy, and giving rise to two stationary points, a minimum (a_2 electronic symmetry) and a transition state (b_1 electronic symmetry).

Looking at a pseudorotation path similar to C_5H_5•, it is clear that it is indeed downhill in energy from the $^2B_1$ saddle point on the potential surface to the $^2A_2$ minimum. The imaginary frequency of 2167*i* cm^{-1} is consistent with a time of ca. 10 fs to move away from the saddle point, which can be taken as an estimate of the lifetime of the transition state. With such a small lifetime, any population which arrives at the $^2B_1$ transition state point on the potential surface will quickly relax toward the $^2A_2$ minimum.

Figure 4.8 shows a one-dimensional slice of the potential energy surfaces of pyrrolyl along the C_{2v} (a_1) axis. DFT calculations were employed to evaluate the energetic relation between the $^2A_2$ and $^2B_1$ electronic symmetries at the stationary points. At the $^2A_2$ minimum geometry, the upper potential ($^2B_1$) is 1.3 eV higher. In contrast, at the $^2B_1$ saddle point geometry, the upper potential energy ($^2A_2$) is located only 0.17 eV above the $^2B_1$ saddle point. In terms of the potential energy surface expansion in Equation 1.11, b_2 vibrations can vibronically couple the $^2A_2$ and $^2B_1$ states. At the $^2B_1$ stationary point, the energy separation is small, and the coupling term in Equation 1.11 becomes large and negative. If the magnitude of the coupling term exceeds the other quadratic term, the stationary point will become a saddle point. The imaginary frequency of 2167*i* cm^{-1} for a b_2 mode is consistent with this. At the $^2A_2$ stationary point, however, there is a relatively large energy separation, which suggests that vibronic coupling effects will be minimal. This region is, of course, the portion of the configuration space explored in the photoelectron spectrum of the pyrrolyl $^2A_2$ ground state. As discussed before, the band origin of the $^2A_2$ state (corresponding to the pyrrolyl radical EA) is 2.145 ± 0.010 eV. Without resolvable features for the $^2B_1$ excited state, assignment of the term energy is difficult. According to the DFT calculations this value is 0.49 eV.

With the above measurement of the pyrrolyl EA, the bond dissociation energy can now be determined for breaking the pyrrole N—H bond, as outlined in Chapter 2. However, the recently determined pyrrole N—H bond dissociation energy[5] (93.92 ± 0.11 kcal mol^{-1})

has an error bar much smaller than usually obtained through the methods of Chapter 2. Consequently, the EA determined here can be combined with this bond dissociation energy to determine a precise value for the 0 K pyrrole deprotonation enthalpy, $\Delta_{acid}H_0(C_4H_4N—H)$ = 358.0 ± 0.4 kcal mol^{-1}. Using thermodynamic information from the Gaussian output files, conversion to the 298 K deprotonation enthalpy and gas phase acidity yields $\Delta_{acid}H_{298}(C_4H_4N—H)$ = 359.4 ± 0.4 kcal mol^{-1} and $\Delta_{acid}G_{298}(C_4H_4N—H)$ = 351.9 ± 0.4 kcal mol^{-1}, respectively. This compares well with but improves upon the literature values[12] of $\Delta_{acid}H_{298}(C_4H_4N—H)$ = 358.6 ± 2.2 kcal mol^{-1} and $\Delta_{acid}G_{298}(C_4H_4N—H)$ = 350.9 ± 2.0 kcal mol^{-1}.

4.5 Conclusion

The photoelectron spectrum of pyrrolide reveals the EA of pyrrolyl radical to be 2.145 ± 0.010 eV. This EA value and the pyrrole N—H bond dissociation energy were combined in a thermochemical cycle to yield the gas-phase acidity of pyrrole, $\Delta_{acid}G_{298}(C_4H_4N—H)$ = 351.9 ± 0.4 kcal mol^{-1}. The Franck-Condon simulation of the photoelectron spectrum confirms that the ground state of pyrrolyl is $^2A_2$ and identifies three harmonic vibrational frequencies active in the spectrum (925 ± 65, 1012 ± 25, and 1464 ± 20 cm^{-1}). These totally symmetric modes of $^2A_2$ pyrrolyl have large displacements along the ring coordinates. The first excited state of pyrrolyl, $^2B_1$, appears broad and featureless, overlapping the tail of the $^2A_2$ portion of the spectrum. DFT calculations predict a saddle point for the $^2B_1$ stationary point, with a b_2 imaginary frequency of 2167*i* cm^{-1} indicating that the potential energy surface is rather steep along this coordinate. Substantial lifetime broadening is responsible for the appearance of the $^2B_1$ state in the photoelectron spectrum. The term energy for the $^2B_1$ state is 0.49 eV according to the DFT calculations, but this energy cannot be determined from the spectrum.

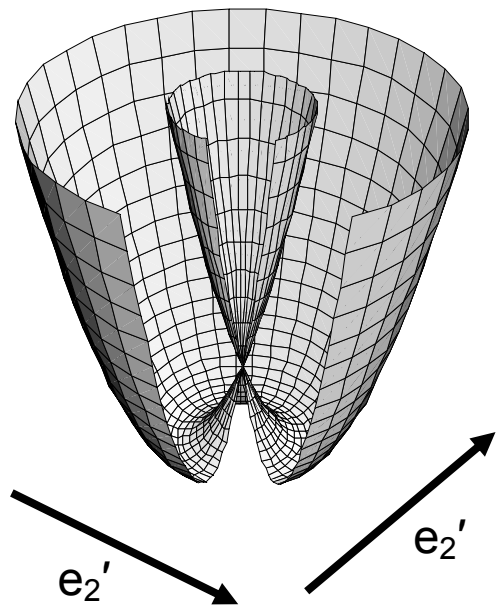

Figure 4.6 Adiabatic potential energy surface of the two lowest electronic states of cyclopentadienyl radical.

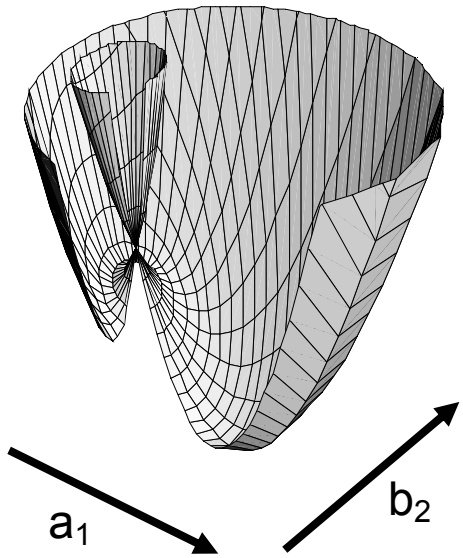

Figure 4.7 Adiabatic potential energy surface of the two lowest electronic states of the pyrrolyl radical.

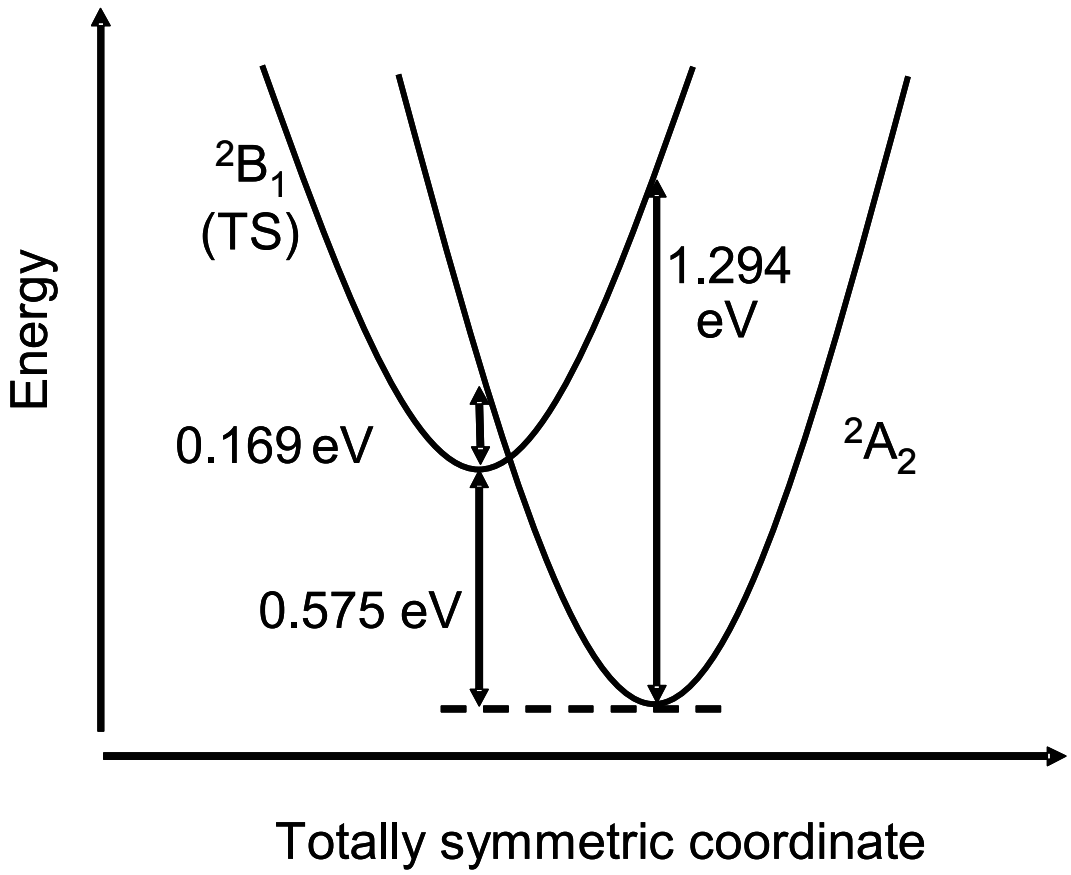

Figure 4.8 Schematic illustration of the potential energy curves of the two lowest electronic states of the pyrrolyl radical, corresponding to a slice of the potential energy surfaces shown in Figure 4.7 along the totally symmetric coordinate. The potential energy separations were calculated at the B3LYP/6-311++G(d,p) level.

Chapter 4 References

[1] G.B. Bacskay, M. Martoprawiro, and J.C. Mackie, *An ab initio quantum chemical study of the electronic structure and stability of the pyrrolyl radical: Comparison with the isoelectronic cyclopentadienyl radical.* Chemical Physics Letters, 1998. **290**(4-6): p. 391-398.

[2] J.H. Richardson, L.M. Stephenson, and J.I. Brauman, *Photodetachment of Electrons from Large Molecular Systems - Pyrrolate Ion - Electron Affinity of C_4H_4N.* Journal of the American Chemical Society, 1975. **97**(5): p. 1160-1162.

[3] P.J. Derrick, L. Asbrink, O. Edqvist, and E. Lindholm, *Photoelectron-Spectroscopical Study of Vibrations of Furan, Thiophene, Pyrrole and Cyclopentadiene.* Spectrochimica Acta, Part A: Molecular Spectroscopy, 1971. **A 27**(12): p. 2525-2537.

[4] J. Wei, A. Kuczmann, J. Riedel, F. Renth, and F. Temps, *Photofragment velocity map imaging of H atom elimination in the first excited state of pyrrole.* Physical Chemistry Chemical Physics, 2003. **5**(2): p. 315-320.

[5] B. Cronin, M.G.D. Nix, R.H. Qadiri, and M.N.R. Ashfold, *High resolution photofragment translational spectroscopy studies of the near ultraviolet photolysis of pyrrole.* Physical Chemistry Chemical Physics, 2004. **6**(21): p. 5031-5041.

[6] A.J. Gianola, T. Ichino, R.L. Hoenigman, S. Kato, V.M. Bierbaum, and W.C. Lineberger, *Thermochemistry and electronic structure of the pyrrolyl radical.* Journal of Physical Chemistry A, 2004. **108**(46): p. 10326-10335.

[7] J.C. Rienstra-Kiracofe, D.E. Graham, and H.F. Schaefer, *Medium ring compounds and their anions: a systematic density functional theory study.* Molecular Physics, 1998. **94**(5): p. 767-787.

[8] A. Samuni and P. Neta, *Electron-Spin Resonance Study of Reaction of Hydroxyl Radicals with Pyrrole, Imidazole, and Related Compounds.* Journal of Physical Chemistry, 1973. **77**(13): p. 1629-1635.

[9] D.M. Neumark, *Transition-State Spectroscopy Via Negative-Ion Photodetachment.* Accounts of Chemical Research, 1993. **26**(2): p. 33-39.

[10] B.E. Applegate, T.A. Miller, and T.A. Barckholtz, *The Jahn-Teller and related effects in the cyclopentadienyl radical. I. The ab initio calculation of spectroscopically observable parameters.* Journal of Chemical Physics, 2001. **114**(11): p. 4855-4868.

[11] B.E. Applegate, A.J. Bezant, and T.A. Miller, *The Jahn-Teller and related effects in the cyclopentadienyl radical. II. Vibrational analysis of the $A\,^2A_2''$ - $X\,^2E_1''$ electronic transition.* Journal of Chemical Physics, 2001. **114**(11): p. 4869-4882.

[12] J.E. Bartmess, *"Negative Ion Energetics Data"*, in *NIST Chemistry Webbook, NIST Standard Reference Database Number 69*, J.P. Linstrom and W.G. Mallard, Editors. June 2005, National Institue of Standards and Technology: Gaithersburg MD, 20899.

5 Imidazolide, $C_3H_3N_2^-$

5.1 Introduction

Substitution of a N atom for a C—H group in cyclopentadiene results in the pyrrole molecule; substitution of a second N atom for another C—H group can result in two isomers depending upon the arrangement of the two N atoms in the ring. If the two N atoms are adjacent in the ring, the result is the pyrazole molecule; if the two N atoms are spaced in the ring, the result is the imidazole molecule. As in the pyrrole system, deprotonation of imidazole takes place at the N site to form 1-imidazolide anion. In imidazole, however, a carbon site is also quite acidic[1, 2] and is deprotonated by HO^- to form an imidazolide isomer, 5-imidazolide. The gas phase acidities ($\Delta_{acid}G_{298}$) of the imidazole N and C5 protons are 342.6 ± 0.4 and 380 ± 4 kcal mol^{-1}, respectively. Although these ions have the same mass, they should have different photoelectron signatures and, if formed in the flow tube, both should appear in the photoelectron spectrum. The photoelectron spectra obtained reveal vibrational and electronic structure of the corresponding neutral radicals. The results presented here are also available in a recent publication[3] (*J. Phys. Chem. A*, **2005**, 109, 11504-11514).

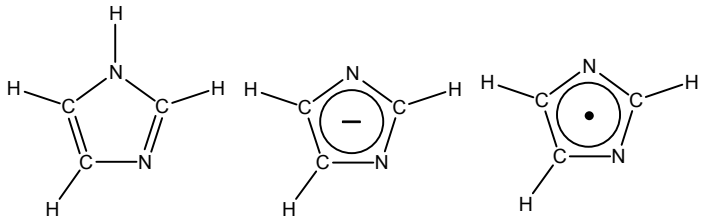

Imidazole 1-Imidazolide 1-Imidazolyl Radical

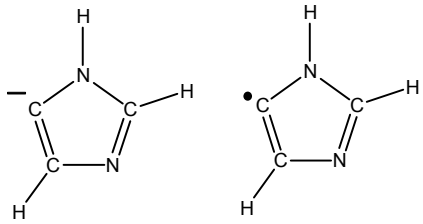

5-Imidazolide 5-Imidazolyl Radical

5.2 Experiment

Hydroxide ions are created using the microwave discharge ion source as described in Chapter 2. Imidazole (Sigma, 99%) is introduced downstream by flowing a stream of helium through a crystalline imidazole sample heated to ~50 °C. The imidazole is deprotonated by HO^- to form imidazolide ions. Typical imidazolide ion beam currents were ~150 pA. The laser wavelength used for photodetachment of imidazolide was 351.1 nm. In some experiments O^- was used as the deprotonation agent. Measurement of the EA of oxygen was used in calibration of the absolute energy scale.

5.3 Results

The 351.1 nm (3.531 eV) magic angle photoelectron spectrum of 1-imidazolide is shown in Figure 5.1. The most intense peak, labeled A, is assigned as the ground state band origin, and the EA of 1-imidazolyl is determined to be 2.613 ± 0.006 eV. Several peaks are observed to higher binding energy, representing vibrational levels of 1-imidazolyl. Table 5.1 lists the energies of the observed peaks relative to the origin. Figure 5.2 shows the 298 K photoelectron spectrum with the laser polarization parallel (θ = 0°) and perpendicular (θ = 90°) to the photoelectron collection axis. A value of –0.30 ± 0.08 was obtained for the anisotropy parameter (β) of the major features in the spectrum.

DFT calculations were performed to make assignments of the photoelectron spectra, as outlined in Chapter 2. Geometry optimizations and frequency calculations were performed

Peak Label	Peak Position (cm^{-1})
A	0
B	955 ± 15
C	1365 ± 20
D	1575 ± 30
E	1925 ± 25
F	2325 ± 30

Table 5.1 Relative experimental peak positions for peaks labeled in Figure 5.1.

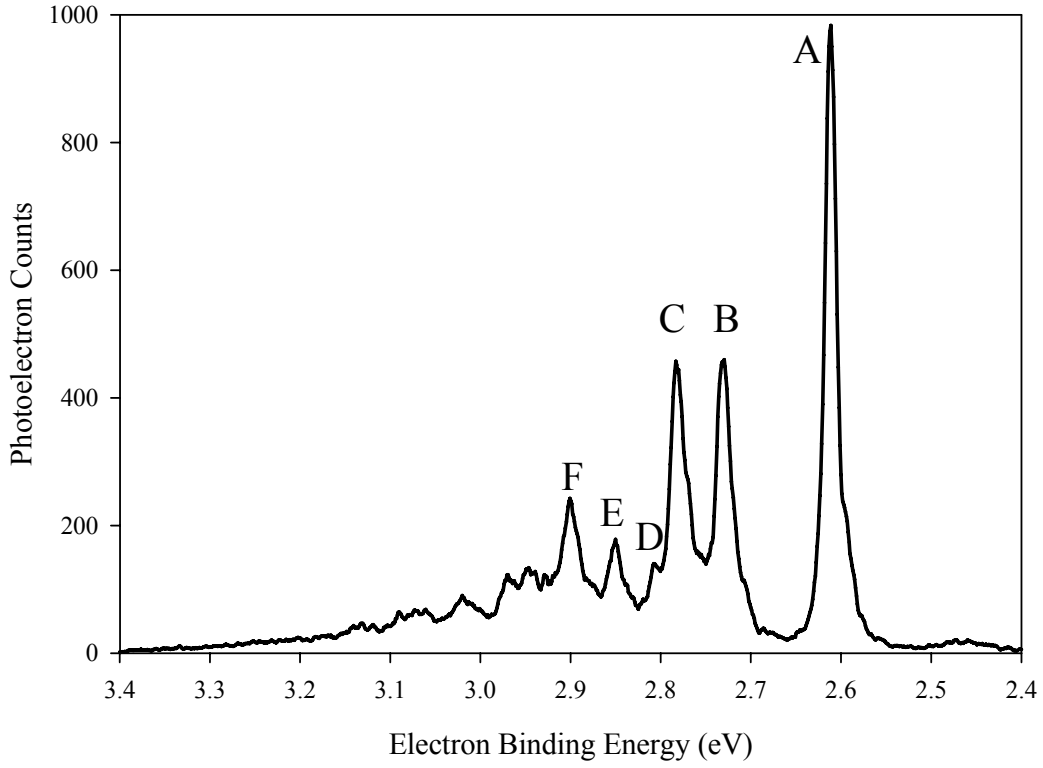

Figure 5.1 351.1 nm magic angle photoelectron spectrum of 1-imidazolide at 298 K.

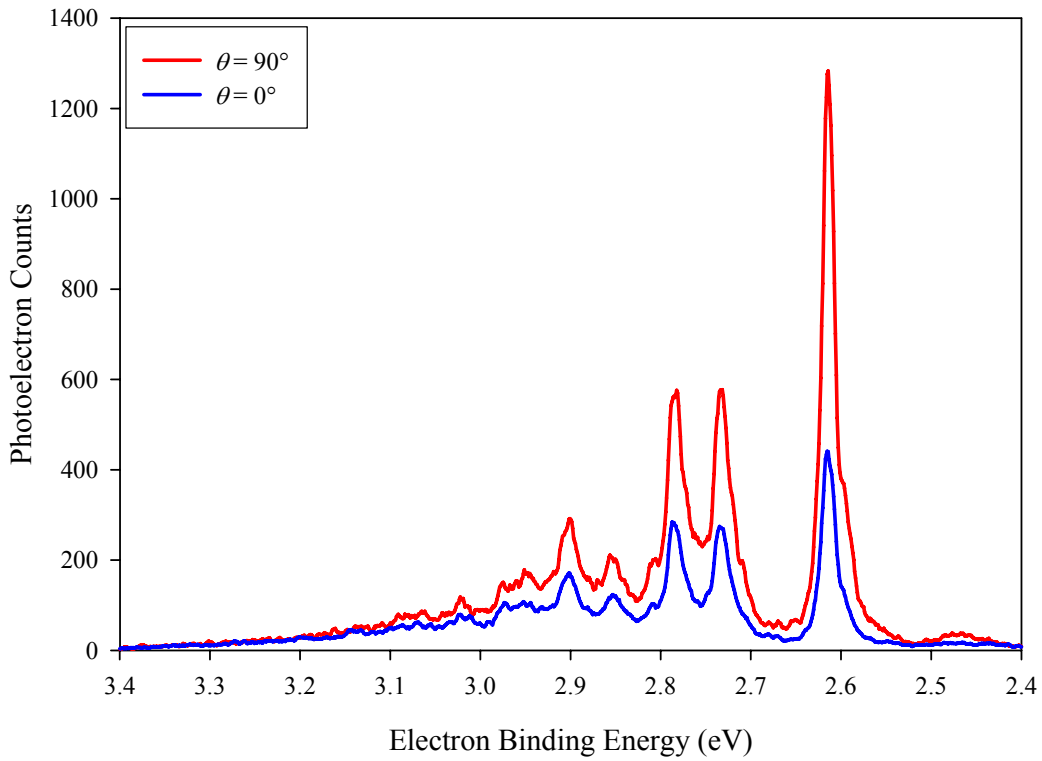

Figure 5.2 351.1 nm photoelectron spectra of 1-imidazolide taken at 298 K. The blue curve was obtained with the laser at vertical polarization ($\theta = 0°$), and the red curve was obtained with the laser at horizontal polarization ($\theta = 90°$).

at the B3LYP/6-311++G(d,p) level of DFT for ground state 1-imidazolide ($^1A_1$), and the $^2B_1$, $^2B_2$, and $^2A_1$ states of 1-imidazolyl. Table 5.2 lists the optimized geometries and Table 5.3 lists the harmonic vibrational frequencies obtained at these four stationary points. As with the pyrrole system, these stationary points all have C_{2v} symmetry. Figure 5.3 depicts the molecular orbitals of 1-imidazolide, illustrating how the orbitals have been reordered for this system. Detachment from the highest occupied molecular orbital of 1-imidazolide will result in the ground state of 1-imidazolyl, $^2B_1$. Detachment from lower energy molecular orbitals of 1-imidazolide results in excited states of 1-imidazolyl, $^2B_2$ and $^2A_2$. The DFT calculations find a minimum for $^2B_1$ 1-imidazolyl, but transition states for both $^2B_2$ and $^2A_2$ 1-imidazolyl as indicated by the b_1 vibrations with imaginary frequencies.

A Franck-Condon simulation was performed for detachment of $^1A_1$ 1-imidazolide to $^2B_1$ 1-imidazolyl and is depicted in Figure 5.4. The simulation reproduces the observed experimental spectrum reasonably well. The DFT calculations predict an EA of 2.592 eV, in good agreement with the experimental value. Thus, the observed spectrum is assigned to the $^2B_1$ ground state of 1-imidazolyl. A $^2B_1$ ground state for 1-imidazolyl was also observed in aqueous solution.[4] With the Franck-Condon simulation, assignments of the vibrational peaks can now be made. Peak A corresponds to the vibrationless origin. A small 1-imidazolide hot-band peak appears to lower binding energy of peak A with a frequency of 1165 ± 45 cm^{-1}. The first vibrational peak, B, is a totally symmetric C—C stretching mode (ν_6). The next peak, C, is another totally symmetric mode with C—N stretching motions (ν_3). The overtone of ν_6 and the $\nu_3 + \nu_6$ combination band appear as peaks E and F, respectively.

Peak D, however, does not appear in the Franck-Condon simulation. Comparing the position of this peak with the DFT computed vibrational frequencies for $^2B_1$ 1-imidazolyl, this mode could correspond to an overtone of a b_1 mode ($2\nu_{11}$) or a b_2 mode ($2\nu_{18}$). Even

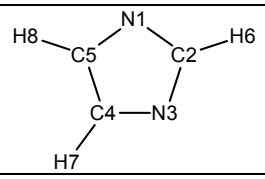		1-Imidazolide	1-Imidazolyl		
Electronic State		$^1A_1$	$^2B_1$	$^2B_2$	$^2A_2$
N—C Bonds (Å)	1-2 / 3-2	1.3489	1.3717	1.3320	1.3398
	1-5 / 3-4	1.3708	1.3172	1.3794	1.4428
C—C Bonds (Å)	4-5	1.3917	1.4744	1.3634	1.3383
C—H Bonds (Å)	2-9	1.0860	1.0816	1.0751	1.0804
	4-7 / 5-8	1.0847	1.0825	1.0765	1.0779
∠NCN (°)	1-2-3	116.30	116.03	105.61	115.31
∠CNC (°)	2-1-5 / 2-3-4	102.69	103.10	111.23	103.64
∠NCC (°)	1-5-4 / 3-4-5	109.16	108.88	105.96	108.70
∠HCN (°)	6-2-1 / 6-2-3	121.85	121.98	127.20	122.35
	7-4-3 / 8-5-1	121.65	123.00	121.05	119.98

Table 5.2 1-Imidazolide and 1-imidazolyl geometries obtained from B3LYP/6-311++G(d,p) calculations.

Mode	Symmetry	1-Imidazolide	1-Imidazolyl		
		$^1A_1$ Frequency (cm^{-1})	$^2B_1$ Frequency (cm^{-1})	$^2B_2$ Frequency (cm^{-1})	$^2A_2$ Frequency (cm^{-1})
ν_1	a_1	3172	3231	3298	3274
ν_2	a_1	3147	3218	3280	3236
ν_3	a_1	1443	1436	1530	1594
ν_4	a_1	1254	1313	1371	1302
ν_5	a_1	1184	1166	1159	1131
ν_6	a_1	1085	982	1116	1037
ν_7	a_1	935	919	906	922
ν_8	a_2	777	974	833	891
ν_9	a_2	666	560	647	454
ν_{10}	b_1	809	867	787	848
ν_{11}	b_1	734	756	758	746
ν_{12}	b_1	696	511	403*i*	924*i*
ν_{13}	b_2	3145	3205	3258	8436
ν_{14}	b_2	1466	1523	1396	3248
ν_{15}	b_2	1304	1289	1269	1345
ν_{16}	b_2	1231	1188	1227	1275
ν_{17}	b_2	1100	1016	1045	956
ν_{18}	b_2	931	780	733	904

Table 5.3 1-Imidazolide and 1-imidazolyl fundamental vibrational frequencies obtained from B3LYP/6-311++G(d,p) calculations.

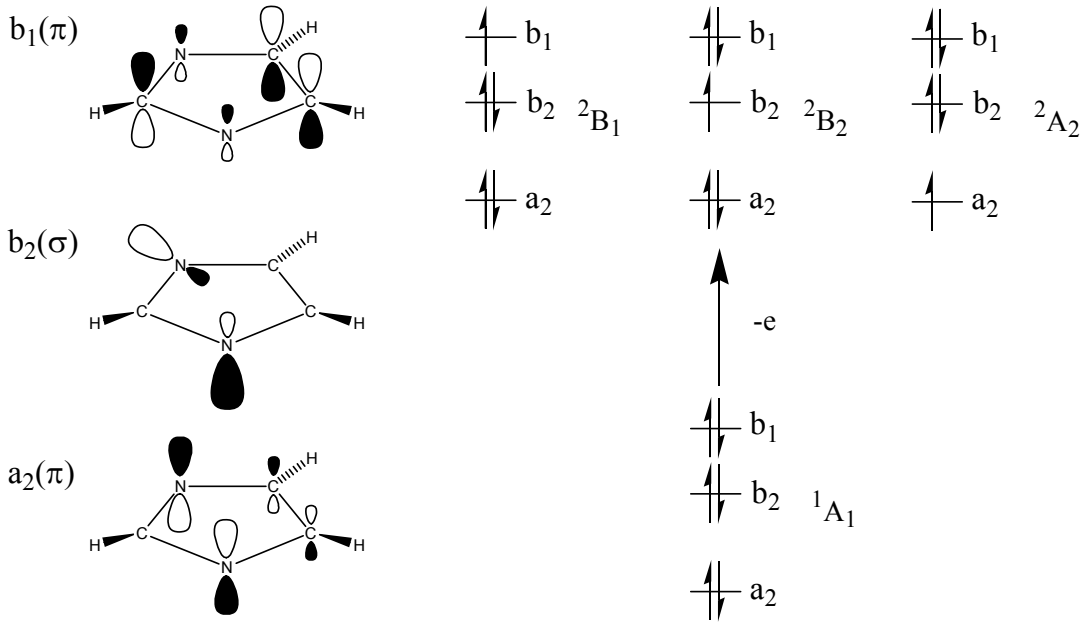

Figure 5.3 Three highest occupied molecular orbitals of 1-imidazolide and the schematic representation of electron photodetachment from 1-imidazolide to form three electronic states of 1-imidazolyl.

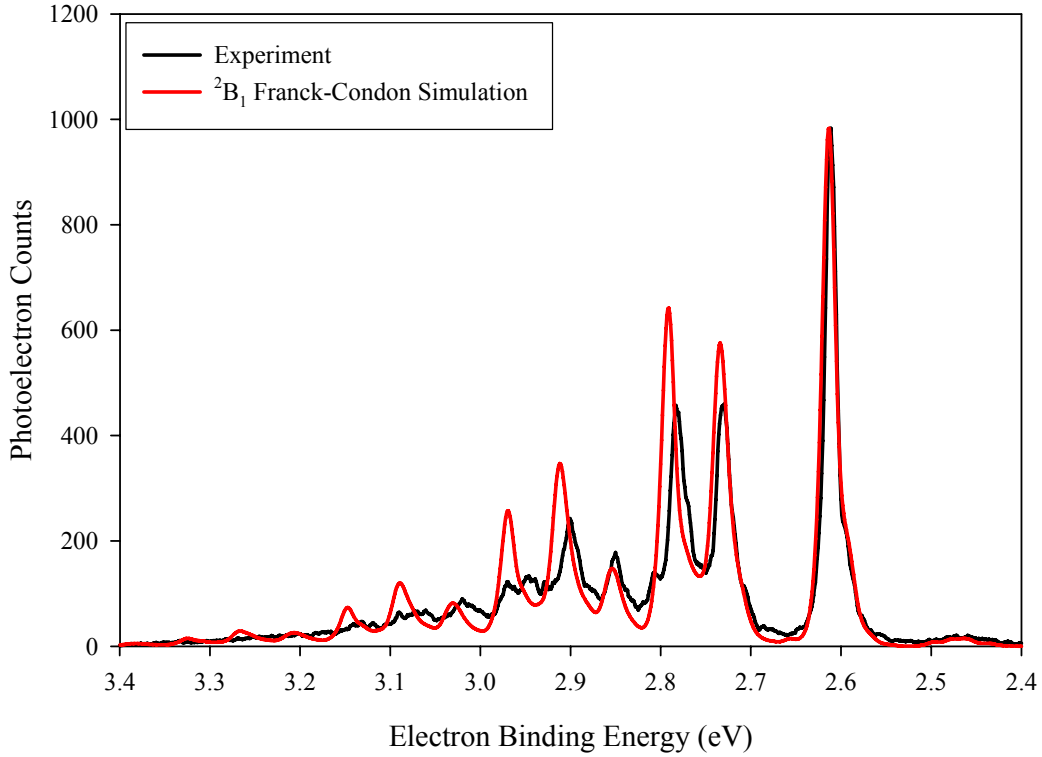

Figure 5.4 Franck-Condon simulation of detachment from $^1A_1$ 1-imidazolide to $^2B_1$ 1-imidazolyl (red) overlaid on the experimental spectrum (black).

quanta of nontotally symmetric modes are symmetry-allowed and can be observed in the spectra. A nonzero Franck-Condon factor for these overtones originates from a large change in the corresponding vibrational frequencies between the initial and final states of the transition. In the 1-imidazolide system, however, there is no significant Franck-Condon factor for either $2\nu_{11}$ or $2\nu_{18}$, as seen by the lack of a vibrational peak in the region of peak D.

Alternatively, overtone peaks can gain intensity from Fermi resonance.[5] The Fermi resonance mixes two vibrational levels of the same vibrational symmetry, and the extent of the mixing is larger when the energy separation of the two unperturbed vibrational levels is smaller. Peak D is located very close to peak C whose Franck-Condon factor is very large according to the simulation. The two peaks are separated by only ~200 cm^{-1}. The mixing of the two levels takes place through anharmonic coupling.

Numerical differentiation of the analytic second derivatives is implemented in the Gaussian 03 program package to obtain cubic force constants. The cubic force constants for the $^2B_1$ state of 1-imidazolyl were calculated at the stationary point and are transformed into the basis of the dimensionless normal coordinates. The calculated force constants for (ν_3, ν_{11}, ν_{11}) and (ν_3, ν_{18}, ν_{18}) are 25 and 209 cm^{-1}, respectively. A simple 2 by 2 matrix is set up for each anharmonic coupling to evaluate the corresponding Fermi resonance mixing, using the DFT harmonic frequencies. The mixing between ν_3 and $2\nu_{11}$ is less than 1%, with an energy shift of less than 1 cm^{-1}. The mixing between ν_3 and $2\nu_{18}$, however, is about 10%, with an energy shift of 19 cm^{-1}. These calculations suggest that the Fermi resonance effects are much larger for ν_3 and $2\nu_{18}$ despite the larger separation of the energy levels. Therefore, peak D is assigned as $2\nu_{18}$, borrowing intensity from the Franck-Condon factor of peak C (ν_3) through the Fermi resonance.

Figure 5.5 shows a portion of the photoelectron spectrum observed at lower binding energy which displays several small features. When O^- was used to deprotonate imidazole,

these features are absent from the spectra and only the spectrum of 1-imidazolide is observed, virtually identical to Figure 5.1. Since HO^- is a stronger base than O^-, deprotonation of a less acidic site of imidazole may be possible with HO^- but not with O^-. DFT calculations were performed to explore the different acidities of imidazole, with the results depicted in Figure 5.6. The DFT calculations predict $\Delta_{acid}H_{298}$ to be 349.6 kcal mol^{-1} for the N1 position, in excellent agreement with an experimental value[3] of 349.7 ± 0.5 kcal mol^{-1}. Combined with a reported deprotonation enthalpy[6] of H_2O ($\Delta_{acid}H_{298}$ = 390.27 ± 0.03), the enthalpy of HO^- reaction with imidazole to yield 1-imidazolide and H_2O is –40.6 kcal mol^{-1} (experimental value is –40.6 ± 0.5 kcal mol^{-1}). The DFT calculations find the other protons in imidazole to be much less acidic. The calculated deprotonation enthalpies, $\Delta_{acid}H_{298}$, are 389.8, 404.4, and 387.9 kcal mol^{-1} for the C2, C4, and C5 positions, respectively. As shown in Figure 5.6, HO^- deprotonation of imidazole is slightly exothermic at C2 and C5, but endothermic for C4 deprotonation. The deprotonation enthalpy of the hydroxyl radical[7] is 382.70 ± 0.10 kcal mol^{-1}, and the DFT calculation results suggest that deprotonation at all of the carbon sites of imidazole by O^- is endothermic. These DFT results suggest that 5-imidazolide detachment is most likely responsible for the small features observed in the spectrum.

To assign these features, DFT geometry optimizations and frequency calculations were performed on 5-imidazolide and 5-imidazolyl. Table 5.4 lists the geometries obtained from these calculations and Table 5.5 lists the frequencies. Using these results, a Franck-Condon simulation was performed and is overlaid on the experimental spectrum in Figure 5.5. DFT predicts an EA of 5-imidazolyl of 1.986 eV, in excellent agreement with the peak located at 1.992 ± 0.010 eV. A progression with a frequency of 900 ± 70 cm^{-1} is observed in the spectrum and the simulation predicts two in-plane ring bending modes to be active in the photoelectron spectrum. These modes have harmonic frequencies of 859 and 931 cm^{-1} and

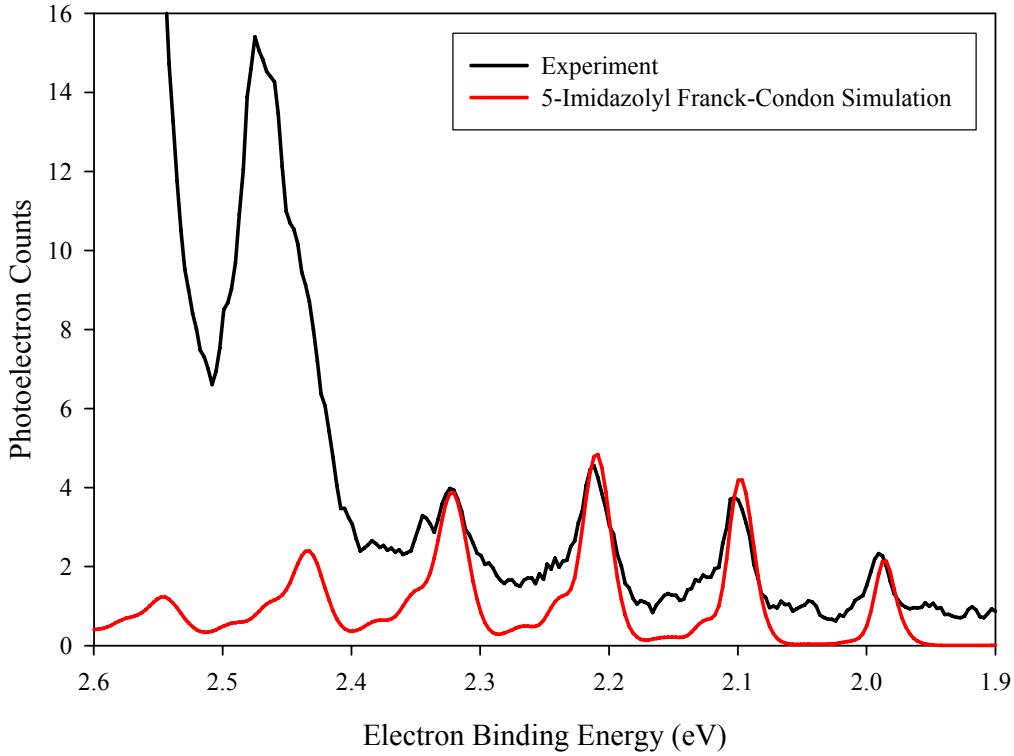

Figure 5.5 Portion of the 351.1 nm magic angle photoelectron spectrum of imidazolide anions produced from the imidazole + HO^- reaction at 298 K (black) and simulation of detachment of 5-imidazolide (red). The peak at ~2.45 eV is the 1-imidazolide hot band and the intense origin peak of 1-imidazolyl grows in at >2.5 eV.

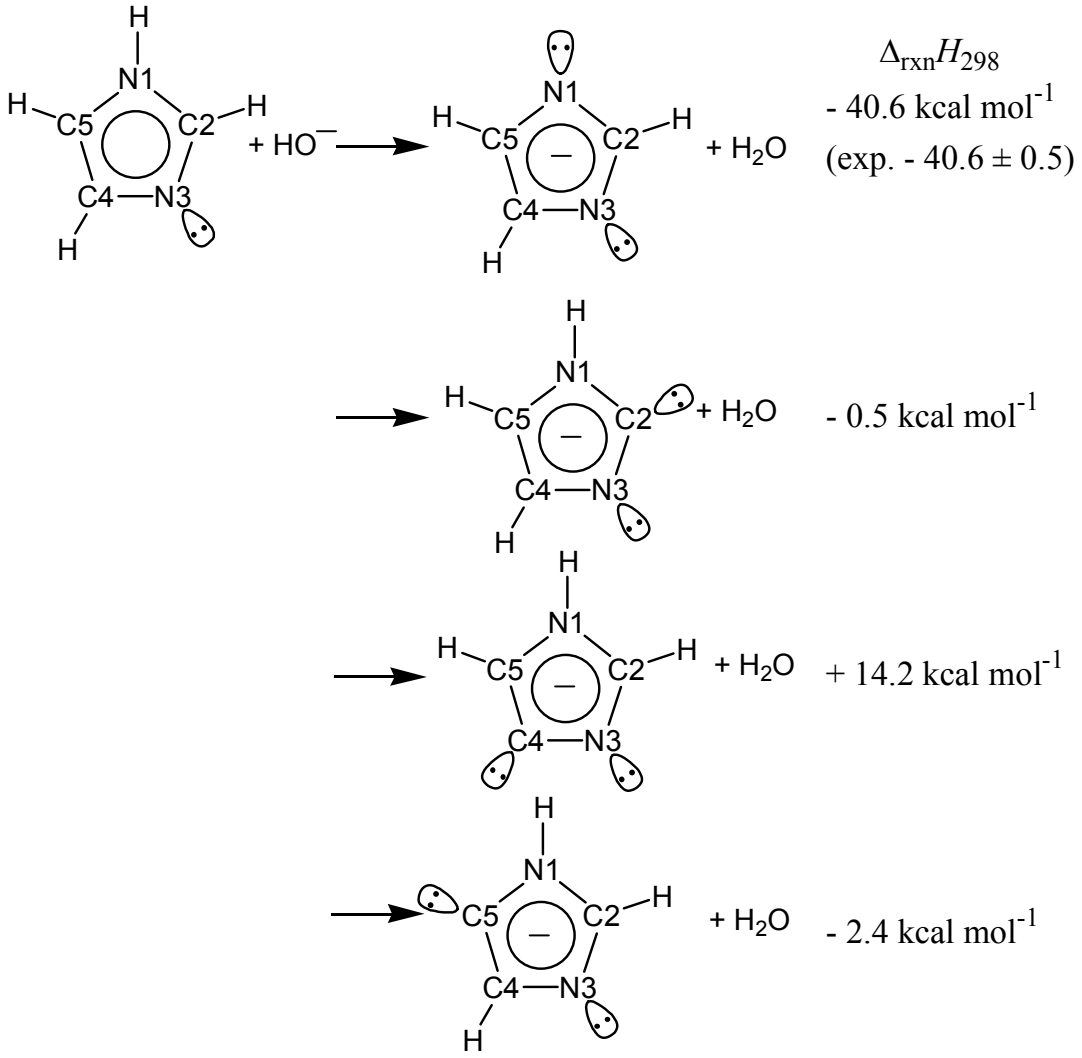

Figure 5.6 B3LYP/6-311+G(d,p) reaction enthalpies for proton transfer reactions at different positions of imidazole.

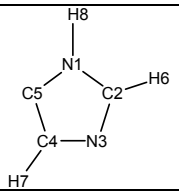		5-Imidazolide	5-Imidazolyl
Electronic State		$^{1}A'$	$^{2}A'$
N—C Bonds (Å)	1-2	1.377	1.368
	2-3	1.317	1.315
	3-4	1.396	1.384
	5-1	1.406	1.370
C—C Bonds (Å)	4-5	1.400	1.363
N—H Bonds (Å)	1-8	1.007	1.007
C—H Bonds (Å)	2-6	1.084	1.079
	4-7	1.084	1.076
∠NCN (°)	1-2-3	110.4	111.1
∠CNC (°)	2-1-5	111.8	105.7
	2-3-4	103.9	107.2
∠NCC (°)	1-5-4	99.0	108.5
	3-4-5	115.0	107.5
∠HNC (°)	8-1-2	124.5	127.8
∠HCN (°)	6-2-1	123.8	123.2
∠HCN (°)	7-4-5	126.3	130.0

Table 5.4 5-Imidazolide and 5-imidazolyl geometries obtained from B3LYP/6-311++G(d,p) calculations.

Mode	Symmetry	1-Imidazolide $^1A'$ Frequency (cm^{-1})	1-Imidazolyl $^2A'$ Frequency (cm^{-1})
ν_1	a'	3638	3656
ν_2	a'	3171	3277
ν_3	a'	3164	3246
ν_4	a'	1509	1518
ν_5	a'	1387	1434
ν_6	a'	1328	1408
ν_7	a'	1271	1315
ν_8	a'	1190	1249
ν_9	a'	1100	1149
ν_{10}	a'	1070	1106
ν_{11}	a'	1022	1056
ν_{12}	a'	941	931
ν_{13}	a'	892	859
ν_{14}	a''	784	818
ν_{15}	a''	687	784
ν_{16}	a''	674	673
ν_{17}	a''	655	556
ν_{18}	a''	507	439

Table 5.5 5-Imidazolide and 5-imidazolyl fundamental vibrational frequencies obtained from B3LYP/6-311++G(d,p) calculations.

are ν_{13} and ν_{12}, respectively. This progression reflects the differences in the angles of the five-membered ring between the anion and the neutral, particularly the N1-C5-C4 angle.

5.4 Discussion

With two N atoms in the five-membered ring, the relative energies of the highest occupied molecular orbitals of 1-imidazolide are different compared to the pyrrolide system. Since the a_2 orbital of 1-imidazolide is mainly composed of nitrogen p orbitals it will be stabilized relative to the b_1 orbital which has only minor contributions from the nitrogen p orbitals. This stabilization is in fact much larger than in the pyrrolide system, such that the a_2 orbital is lower in energy than a b_2 orbital. The energetic ordering of the 1-imidazolide molecular orbitals is illustrated in Figure 5.3. Not including zero point energies, the DFT calculations predict that the term energy for the $^2B_2$ state is 0.84 eV, while that of the $^2A_2$ state is 0.95 eV. Either the laser photon energy is insufficient for detachment to these excited states or the kinetic energy of the photoelectrons may be too low (< 0.15 eV) for efficient detection.

With these electronic states lying so closely together, non-adiabatic effects can become important. For the 1-imidazolyl radical ground state, there is reasonable agreement of the Franck-Condon simulation with the experimental spectrum, indicating that non-adiabatic effects are minimal in the vicinity of the $^2B_1$ ground state. Near the $^2B_2$ and $^2A_2$ stationary points, the non-adiabatic effects become more significant. These two excited states couple strongly with each other through b_1 vibrational modes and are transformed into transition states. There is also significant vibronic coupling between the $^2B_1$ ground state and the $^2A_2$ state, as evidenced by the unexpected 8436 cm^{-1} b_2 vibration calculated for the $^2A_2$ state.

Coupling between the $^2B_1$ ground state and $^2A_2$ excited state may also be responsible for the appearance of the Fermi resonance peak in the spectrum of the $^2B_1$ state. Looking at

the potential energy surface expansion of Equation 1.11, vibronic coupling between the $^2B_1$ and $^2A_2$ states occurs through b_2 vibrational modes. Vibronic coupling effects on the $^2B_1$ surface near its equilibrium geometry are marginal because of the relatively large energy separation with the $^2A_2$ state. The DFT calculations show that the $^2A_2$ surface lies 1.9 eV higher in energy than the $^2B_1$ surface at its equilibrium geometry.

The cubic force constant for $\Phi_{3,18,18}$ is explicitly written as:

$$\Phi_{3,18,18} = \frac{\partial^3 V}{\partial Q_3 \partial Q_{18} \partial Q_{18}} = \frac{\partial}{\partial Q_3}\left(\frac{\partial^2 V}{\partial Q_{18}{}^2}\right) \tag{5.1}$$

This cubic force constant is a gradient of the quadric force constant for the ν_{18} b_2 mode along the totally symmetric ν_3 mode. Looking again to Equation 1.11, the ν_{18} quadratic force constant depends on the vibronic coupling between the $^2B_1$ and $^2A^2$ states. Consequently, the cubic force constant $\Phi_{3,18,18}$ can exhibit the dependence of the vibronic coupling on the ν_3 motion.

In the Franck-Condon simulation shown in Figure 5.4, the parameters of the following equation are calculated.[8]

$$Q = JQ' + K \tag{5.2}$$

Here, Q' and Q are matrices for the normal coordinates of the imidazolide and imidazolyl ground states, respectively; J is a matrix for Duschinsky rotation of the two sets of normal coordinates; K is a column vector representing the geometry displacement between the two states. The components of the K vector for all of the a_1 modes of the $^2B_1$ state of 1-imidazolyl are shown in Table 5.6. The largest displacement takes place along ν_3, and the magnitude of the displacement is 1.249 in dimensionless units. The second largest value is ν_6, with a displacement of 0.919. These large displacements manifest themselves in the photoelectron spectrum as vibrational progressions for these modes.

a_1 mode	$K(^2B_1 - {}^1A_1)$	$K(^2B_1 - {}^2A_2)$
1	0.036	0.075
2	0.031	0.081
3	1.249	2.768
4	0.376	1.094
5	0.322	0.026
6	0.919	1.488
7	0.534	1.322

Table 5.6 Geometry displacement parameters, K, in dimensionless normal coordinates for $^2B_1$ 1-imidazolyl – $^1A_1$ 1-imidazolide and $^2B_1$ 1-imidazolyl – $^2A_2$ 1-imidazolyl.

In the same way, the *K* vector can be calculated for the geometry shift from the $^2B_1$ ground state to the $^2A_2$ excited state of imidazolyl; its components are also shown in Table 5.6. The geometry shift along ν_3 is by far the largest between the two imidazolyl states, having a displacement of 2.768. The large *K* vector component for the N—C stretching mode is not surprising as Table 5.2 shows that the N1—C5 (N3—C4) is very different between the $^2B_1$ and $^2A_2$ states. Assuming for a moment that the $^2B_1$ and $^2A_2$ states have identical normal modes (i.e. parallel modes) and that the potential energy surfaces are harmonic, the *K* vector represents the slopes of the $^2A_2$ potential energy surface along the a_1 modes at the equilibrium geometry of the $^2B_2$ state. Under this assumption, the energy separation between the $^2B_1$ and $^2A_2$ states changes by ~0.6 eV as the geometry shifts along the ν_3 mode by one dimensionless unit. The nuclear motions for this mode is asymmetric NCN stretching, and the corresponding mode in pyrrolyl was found to be responsible for strong vibronic coupling between the $^2A_2$ and $^2B_1$ states of pyrrolyl.[9] Taking the magnitude of the vibronic coupling matrix as 0.15 eV, which represents moderately strong vibronic coupling,[10-14] the quadratic coupling constant for the ν_{18} mode of 1-imidazolyl changes by 90 cm^{-1} as the energy separation decreases from 1.9 to 1.3 eV. Thus it is reasonable that vibronic coupling between the $^2B_1$ and the $^2A_2$ states of imidazolyl contributes to the relatively large anharmonicity, which causes the Fermi resonance effects.

Thermodynamics

Using the experimentally determined EA for 1-imidazolyl, it is now possible to derive the imidazole N—H bond dissociation energy using the methods outlined in Chapter 2. Experimental values[3] for the imidazole gas phase acidity and deprotonation enthalpies are $\Delta_{acid}G_{298}$ = 342.6 ± 0.4 kcal mol^{-1}, $\Delta_{acid}H_{298}$ = 349.7 ± 0.5 kcal mol^{-1}, and $\Delta_{acid}H_0$ = 348.4 ± 0.5 kcal mol^{-1}. Combining the EA with the 0 K deprotonation enthalpy yields D_0(imidazole N-H)

= 95.1 ± 0.5 kcal mol^{-1}. In turn, the bond dissociation energy can be combined with the imidazole heat of formation[7] ($\Delta_f H_{298}$ = 31.8 ± 0.1 kcal mol^{-1}) to determine the heat of formation of 1-imidazolyl radical, $\Delta_f H_{298}$ = 76.2 ± 0.6 kcal mol^{-1}.

With an experimental value for the imidazole C5 gas phase acidity, it would be possible to determine the imidazole C5—H bond dissociation in a similar way. Experimental considerations make it difficult to directly measure the acidity of a proton in the presence of more acidic protons in the same molecule. The photoelectron measurements on 5-imidazolide, however, definitively show that it is energetically possible to deprotonate imidazole at the C5 position using HO^-. Since these measurements also indicate that it is not energetically possible to deprotonate imidazole at the C5 position using O^-, the gas phase acidity of the C5 proton of imidazole is bracketed between the acidities of H_2O and HO, yielding $\Delta_{acid}G_{298}$(imidazole C5—H) = 380 ± 4 kcal mol^{-1}. Combining this value with the 5-imidazolyl EA of 1.992 ± 0.010 eV and thermal corrections from the DFT results, D_0(imidazole C5—H) = 119 ± 4 kcal mol^{-1}. From D_0, the heat of formation of 5-imidazolyl radical can also be determined, $\Delta_f H_{298}$ = 100 ± 4 kcal mol^{-1}.

5.5 Conclusion

The photoelectron spectrum of imidazolide, produced by HO^- deprotonation of imidazole in helium buffer gas, has been measured. The EA of 1-imidazolyl radical is determined to be 2.613 ± 0.006 eV. Franck-Condon simulations based on DFT calculations for the ground states of 1-imidazolide and 1-imidazolyl reproduce the observed spectrum reasonably well, indicating that two totally symmetric vibrations are active in the spectrum with C—C stretching and C—N stretching motions. The experimental frequencies of these vibrations are 955 ± 15 and 1365 ± 20 cm^{-1}, respectively. Additionally, a small overtone feature is observed in the spectrum with a frequency of 1575 ± 30 cm^{-1}, gaining intensity due to a Fermi resonance. Combining the EA of 1-imidazolyl with a value for the N—H bond

deprotonation enthalpy of imidazole in a thermodynamic cycle, the imidazole N—H bond dissociation energy is determined to be $D_0 = 95.1 \pm 0.5$ kcal mol^{-1}.

The imidazolide photoelectron spectrum also included several peaks originating from 5-imidazolide. These features reveal the EA of 5-imidazolyl radical to be 1.992 ± 0.010 eV. When O^- was used as the deprotonation agent, these signals were absent from the spectrum, suggesting that the acidity of the proton at the C5 position of imidazole is bracketed by those of H_2O and OH radical and is $\Delta_{acid}G_{298} = 380 \pm 4$ kcal mol^{-1}. The acidity is corrected for thermal effects and combined with the EA of 5-imidazolyl in a thermodynamic cycle to yield the C5—H bond dissociation energy of imidazole, $D_0 = 119 \pm 4$ kcal mol^{-1}. The relatively large error bar arises from the uncertainty of the acidity, and experiments on 1-methylimidazole are underway to allow for more accurate determination of the C—H bond dissociation energy.[15]

Chapter 5 References

[1] J. Catalan, R.M. Claramunt, J. Elguero, J. Laynez, M. Menendez, F. Anvia, J.H. Quian, M. Taagepera, and R.W. Taft, *Basicity and Acidity of Azoles - the Annelation Effect in Azoles.* Journal of the American Chemical Society, 1988. **110**(13): p. 4105-4111.

[2] R.W. Taft, F. Anvia, M. Taagepera, J. Catalan, and J. Elguero, *Electrostatic Proximity Effects in the Relative Basicities and Acidities of Pyrazole, Imidazole, Pyridazine, and Pyrimidine.* Journal of the American Chemical Society, 1986. **108**(12): p. 3237-3239.

[3] A.J. Gianola, T. Ichino, R.L. Hoenigman, S. Kato, V.M. Bierbaum, and W.C. Lineberger, *Photoelectron spectra and ion chemistry of imidazolide.* Journal of Physical Chemistry A, 2005. **109**(50): p. 11504-11514.

[4] A. Samuni and P. Neta, *Electron-Spin Resonance Study of Reaction of Hydroxyl Radicals with Pyrrole, Imidazole, and Related Compounds.* Journal of Physical Chemistry, 1973. **77**(13): p. 1629-1635.

[5] G. Herzberg, *Molecular Specta and Molecular Structure. Vol. II. Infrared and Raman Spectra of Polyatomic Molecules*. 1950, New York: Van Nostrand.

[6] K.M. Ervin and V.F. DeTuro, *Anchoring the gas-phase acidity scale.* Journal of Physical Chemistry A, 2002. **106**(42): p. 9947-9956.

[7] J.E. Bartmess, *"Negative Ion Energetics Data"*, in *NIST Chemistry Webbook, NIST Standard Reference Database Number 69*, J.P. Linstrom and W.G. Mallard, Editors. June 2005, National Institue of Standards and Technology: Gaithersburg MD, 20899.

[8] P. Chen, *Photoelectron Spectroscopy of Reactive Intermediates*, in *Unimolecular and Bimolecular Reaction Dynamics*, C.Y. Ng, T. Baer, and I. Powis, Editors. 1994, Wiley & Sons: New York. p. 371-425.

[9] A.J. Gianola, T. Ichino, R.L. Hoenigman, S. Kato, V.M. Bierbaum, and W.C. Lineberger, *Thermochemistry and electronic structure of the pyrrolyl radical.* Journal of Physical Chemistry A, 2004. **108**(46): p. 10326-10335.

[10] J. Eiding, R. Schneider, W. Domcke, H. Koppel, and W. Vonniessen, *Abinitio Investigation of the Multimode Dynamic Jahn-Teller Effect in the $X\,^2E_{1g}$ State of the Benzene Cation.* Chemical Physics Letters, 1991. **177**(3): p. 345-351.

[11] H. Muller, H. Koppel, and L.S. Cederbaum, *Topology and Dynamics of Vibronically Coupled Potential-Energy Surfaces - General-Aspects and Application to the Ozone Cation.* New Journal of Chemistry, 1993. **17**(1-2): p. 7-29.

[12] M. Mayer, L.S. Cederbaum, and H. Koppel, *Ground-State Dynamics of NO_3 - Multimode Vibronic Borrowing Including Thermal Effects.* Journal of Chemical Physics, 1994. **100**(2): p. 899-911.

[13] S. Mahapatra, H. Koppel, and L.S. Cederbaum, *Impact of nonadiabatic coupling between the conically intersecting $X\,^2A_1$ and $A\,^2B_2$ states of NO_2 on the negative ion photoelectron spectra of NO_2^-.* Journal of Chemical Physics, 1999. **110**(12): p. 5691-5701.

[14] B.E. Applegate, A.J. Bezant, and T.A. Miller, *The Jahn-Teller and related effects in the cyclopentadienyl radical. II. Vibrational analysis of the $A\,^2A_2''$ - $X\,^2E_1''$ electronic transition.* Journal of Chemical Physics, 2001. **114**(11): p. 4869-4882.

[15] S.M. Villano, A.J. Gianola, S. Kato, V.M. Bierbaum, and W.C. Lineberger, *Manuscript in preparation.*

6 Pyrazolide, $C_3H_3N_2^-$

6.1 Introduction

As previously discussed, pyrazole is an isomer of imidazole. In pyrazole the nitrogen atoms in the ring are adjacent whereas in imidazole they are separated. Deprotonation of pyrazole takes place primarily at the nitrogen site to form 1-pyrazolide, but as with imidazole, it is possible to deprotonate a pyrazole carbon site with HO^- to form 5-pyrazolide. The gas phase acidities ($\Delta_{acid}G_{298}$) of the pyrazole N and C5 protons are 346.4 ± 0.3 and 380 ± 4 kcal mol^{-1}, respectively. In contrast with imidazole, the removal of the proton at the pyrazole C5 position was facile, and quite large photoelectron signals from 5-pyrazolide were observed simultaneous with the 1-pyrazolide photoelectons. Here, the EA and vibrational structure of 1- and 5- pyrazolyl are measured. These results are newly available as a publication[1] (*J. Phys. Chem. A*, **2006**, DOI: 10.1021/jp057499+).

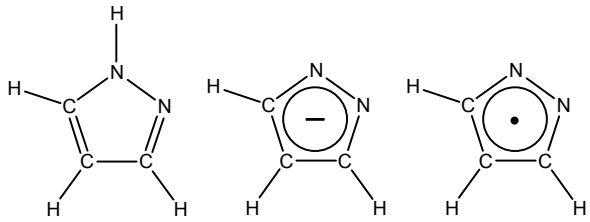

Pyrazole 1-Pyrazolide 1-Pyrazolyl Radical

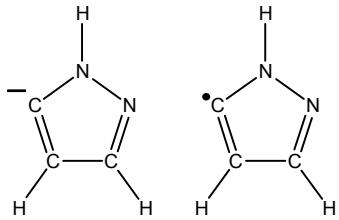

5-Pyrazolide 5-Pyrazolyl Radical

6.2 Experiment

Hydroxide ions are created using the microwave discharge ion source as described in Chapter 2. Pyrazole is introduced into the flow tube by flowing a stream of helium through a crystalline pyrazole sample at room temperature. Deprotonation of pyrazole forms pyrazolide ions, and typical ion beam currents were ~250 pA. In some experiments liquid nitrogen was used to cool the flow tube to aid in cooling of the ions. In these experiments, slightly smaller ion beam currents were observed, ~150 pA. Additionally, pyrazolide ions were also formed by reaction of pyrazole with oxygen anion (O^-) or fluoride (F^-) with similar ion beam currents. F^- is produced by adding a trace amount of NF_3 downstream of the microwave discharge. The laser wavelength used for photodetachment of pyrazolide was 351.1 nm. Measurements of the EAs of oxygen and iodine[2] (3.059 eV) were used to calibrate the absolute energy scale.

6.3 Results

Figure 6.1 shows the 351.1 nm magic angle photoelectron spectrum of pyrazolide ions produced from the reaction of pyrazole with HO^-. Intense peaks are observed at eBE > 2.9 eV, along with several weaker peaks at eBE < 2.6 eV. Spectra were also measured with pyrazolide ions produced from the reaction of pyrazole with O^- and F^-. The spectra obtained with these reactant ions are virtually identical with that in Figure 6.1 at eBE > 2.9 eV, but there are no photoelectron signals observed at eBE < 2.6 eV.

DFT calculations were performed to explore the acidities of pyrazole. Reaction enthalpies for deprotonation of pyrazole by HO^- were computed at the B3LYP/6-311++G(d,p) level. The DFT results were combined with an experimental value of the H_2O deprotonation enthalpy[3] ($\Delta_{acid}H_{298}$ = 390.27 ± 0.03 kcal mol^{-1}) to derive the reaction enthalpies listed in Figure 6.2. Deprotonation at the N1 site is the most exothermic, with a

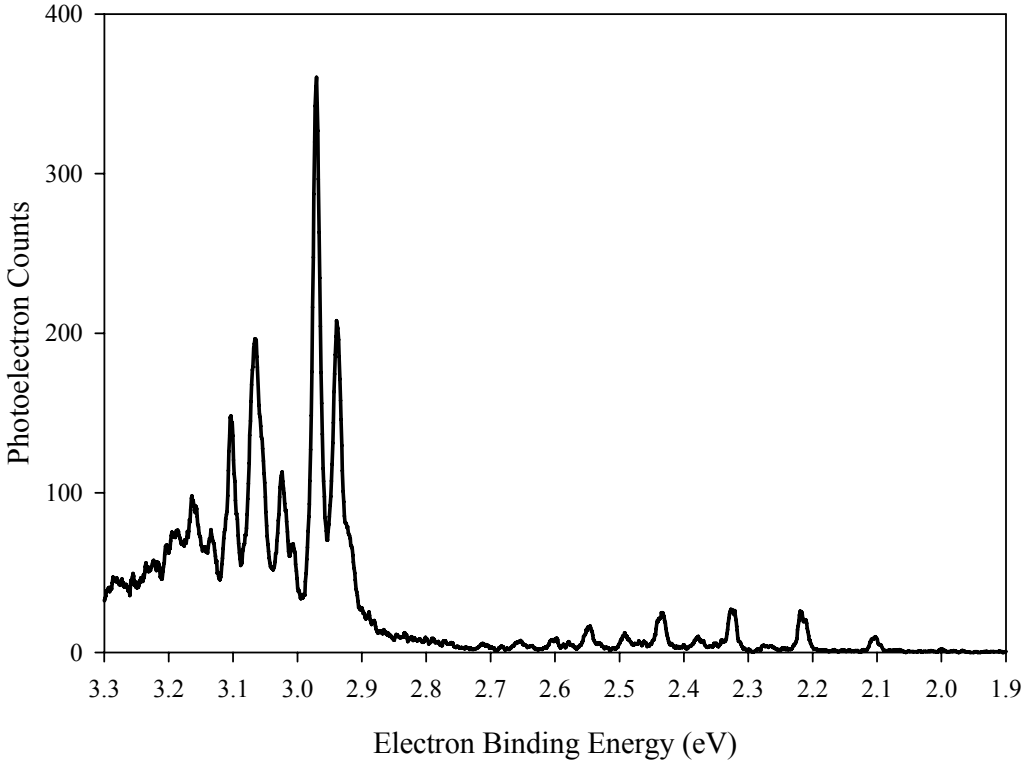

Figure 6.1 351.1 nm magic angle photoelectron spectrum of pyrazolide at 298 K.

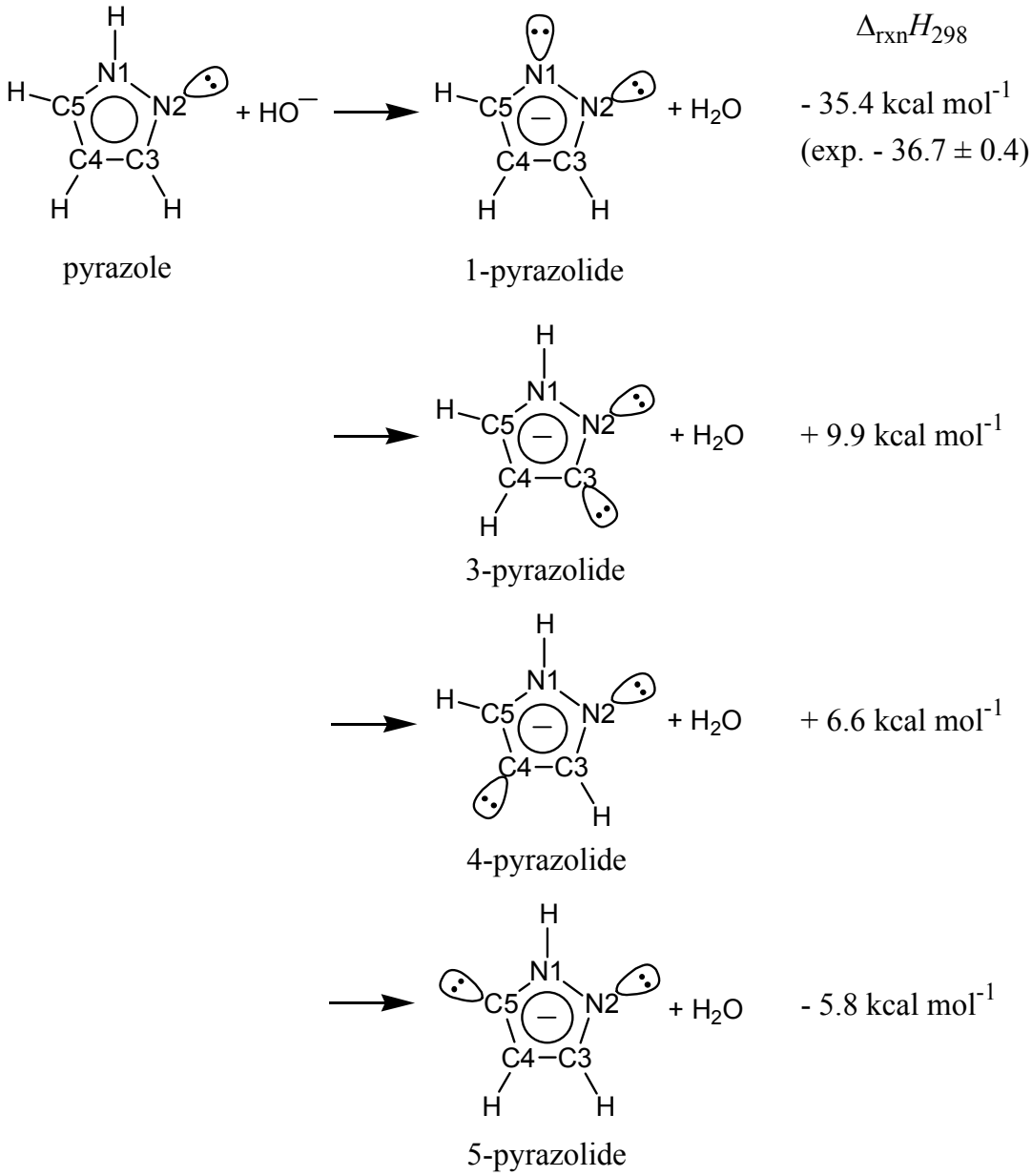

Figure 6.2 DFT reaction enthalpies evaluated for HO^- deprotonation of pyrazole at different positions.

reaction enthalpy of –35.4 kcal mol^{-1}. For deprotonation at the carbon sites, only formation of 5-pyrazolide is predicted to be exothermic, with a reaction enthalpy of –5.8 kcal mol^{-1}. When O^- [$\Delta_{acid}H_{298}$(OH) = 382.6 ± 0.07 kcal mol^{-1}] [4] or F^- [$\Delta_{acid}H_{298}$(HF) = 371.331 ± 0.003 kcal mol^{-1}] [3] is used, deprotonation at all carbon sites is endothermic. These results suggest assignment of the higher binding energy features to 1-pyrazolide detachment and the lower binding energy features to 5-pyrazolide detachment.

Figure 6.3 shows an expanded region of the higher binding energy portion of the spectrum, corresponding to detachment of 1-pyrazolide. This spectrum was taken with the same experimental conditions as used for the spectrum in Figure 6.1 except that the flow tube was cooled with liquid nitrogen to vibrationally cool the ions. Angular measurements were performed and anisotropy parameters (β) were measured for the different peaks in Figure 6.3, with β values ranging from -0.2 to -0.65. Intuitively, among all of the peaks observed, the one at the lowest binding energy (peak A) is expected to be the origin of the ground electronic state of 1-pyrazolyl. Table 6.1 lists the relative experimental peak positions and β values for features labeled in Figure 6.3. The peak labeled B has $\beta = -0.65 \pm 0.09$, which is significantly different from that of the origin peak, $\beta = -0.25 \pm 0.09$. Observation of distinct anisotropy parameters indicates detachment from different molecular orbitals of the anion, that is, access to different electronic states of the neutral.

To aid in the assignment of these features, DFT calculations were performed on 1-pyrazolide and 1-pyrazolyl. Geometry optimizations and frequency calculations were performed at the B3LYP/6-311++G(d,p) level and C_{2v} stationary points were located for $^1A_1$ 1-pyrazolide, and $^2A_2$, $^2B_1$, and $^2B_2$ 1-pyrazolyl. The DFT calculations predict a minimum for $^1A_1$ 1-pyrazolide, $^2A_2$ and $^2B_1$ 1-pyrazolyl, but a transition state for $^2B_2$ 1-pyrazolyl. Tables 6.2 and 6.3 list the geometries and frequencies obtained from these calculations. These results predict a $^2A_2$ ground state for 1-pyrazolyl, with an EA of 2.945 eV. This predicted EA

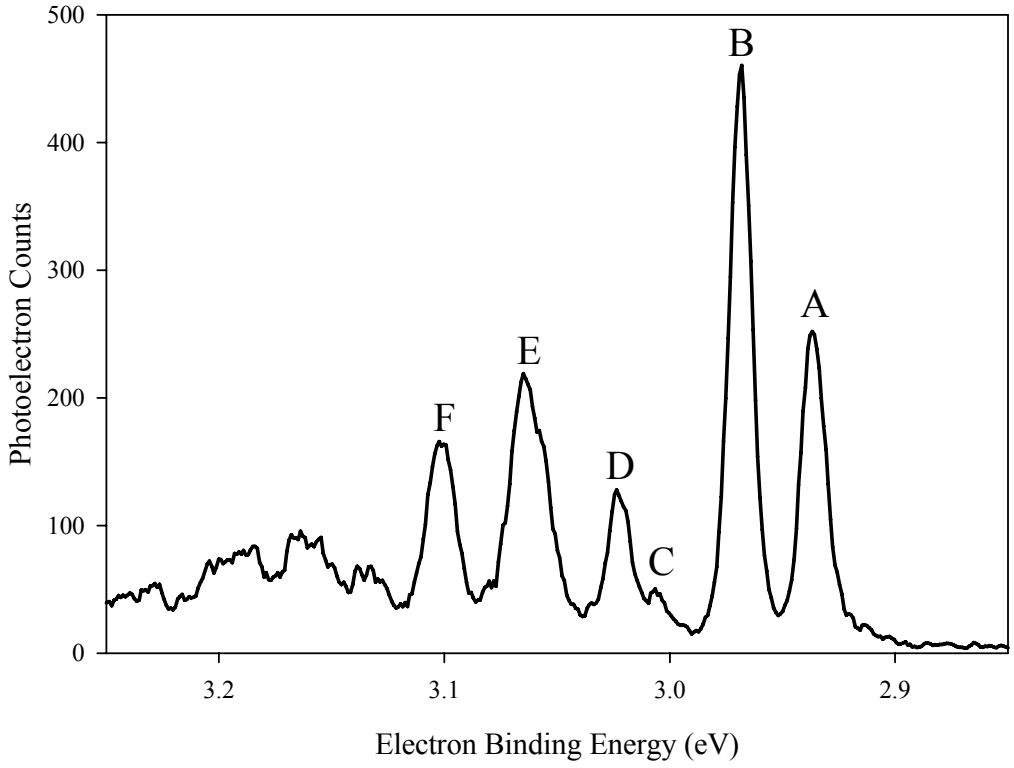

Figure 6.3 351.1 nm magic angle photoelectron spectrum of 1-pyrazolide produced under liquid nitrogen cooled flow tube conditions.

is close to the peak at 2.935 ± 0.005 eV. Considering this, the ground state of 1-pyrazolyl is assigned as $^2A_2$. The DFT results also predict term energies of 0.031 and ~0.1 eV for $^2B_1$ and $^2B_2$ 1-pyrazolyl, respectively. The term energy of the $^2B_1$ state is surprisingly close to the peak spacing between peaks A and B in Figure 6.3. More important than the good agreement with the experimental peak spacing is the observation of a near-degeneracy of the $^2A_2$ and $^2B_1$ states.

Franck-Condon simulations were performed for detachment of 1-pyrazolide to the $^2A_2$ and $^2B_1$ states of 1-pyrazolyl, as outlined in Chapter 2. Fixing the $^2A_2$ origin position and intensity to those of peak A and the $^2B_1$ origin position and intensity to those of peak B yields the simulations found in Figure 6.4, where the agreement between the Franck-Condon simulation and the experimental spectrum is generally poor. The peaks labeled C and D are completely missed by the simulations and the intensity of the bands at higher eBE are severely overestimated. Switching of the assignments (i.e. $^2B_1$ as the ground state and $^2A_2$ as the excited state) does not alleviate the discrepancy. This disagreement is surprising, considering that Franck-Condon simulations of pyrrolide and imidazolide detachment reproduce the experimental spectra rather well. This simulation, however, is reminiscent of the Franck-Condon simulation of cyclopentadienide detachment, where several bands were missing from the spectrum while the intensities of other bands were overestimated.

These observations lead to the conclusion that the geometry displacements from $^1A_1$ 1-pyrazolide to $^2A_2$ and $^2B_1$ 1-pyrazolyl may be overestimated by the DFT calculations. Additionally, vibronic coupling (a.k.a. Pseudo-Jahn-Teller) effects contribute to the disagreement between the Franck-Condon simulation and the experimental spectrum. Simulations of the 1-pyrazolide photoelectron spectrum are currently being carried out by establishing a diabatic model Hamiltonian[5-7] for the neutral states around the equilibrium geometry of the anion ground state. This model Hamiltonian takes into account nonadiabatic effects which are neglected in the Franck-Condon simulation in Figure 6.4. Parameterization

Peak Label	β	Peak Position Relative to peak A	Peak Position Relative to peak B
A	– 0.25 ± 0.09	—	–0.032 ± 0.001 eV
B	– 0.65 ± 0.09	0.032 ± 0.001 eV	—
C	– 0.45 ± 0.15	554 ± 15 cm^{-1}	289 ± 15 cm^{-1}
D	– 0.20 ± 0.09	697 ± 15 cm^{-1}	435 ± 15 cm^{-1}
E	– 0.45 ± 0.13	1016 ± 20 cm^{-1}	754 ± 20 cm^{-1}
F	– 0.30 ± 0.12	1323 ± 20 cm^{-1}	1060 ± 20 cm^{-1}

Table 6.1 Experimental peak positions and anisotropy parameters for peaks appearing in the photoelectron spectrum of 1-pyrazolide.

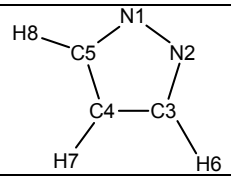		1-Pyrazolide	1-Pyrazolyl		
Electronic State		$^1A_1$	$^2A_2$	$^2B_1$	$^2B_2$
N—N Bonds (Å)	1-2	1.3621	1.2750	1.4676	1.2396
N—C Bonds (Å)	1-5 / 2-3	1.3491	1.4300	1.2991	1.3577
C—C Bonds (Å)	3-4 / 4-5	1.4044	1.3861	1.4374	1.4051
C—H Bonds (Å)	4-7	1.0853	1.0805	1.0816	1.0759
	3-6 / 5-8	1.0824	1.0773	1.0813	1.0789
∠NNC (°)	1-2-3 / 2-1-5	107.89	108.34	107.53	111.54
∠NCC (°)	2-3-4 / 1-5-4	110.85	109.98	110.96	105.72
∠CCC (°)	3-4-5	102.52	103.36	103.02	105.48
∠HCN (°)	6-3-2 / 8-5-1	120.36	119.63	121.39	122.04
∠HCC (°)	7-4-3 / 7-4-5	128.74	128.32	128.49	127.26

Table 6.2 1-Pyrazolide and 1-pyrazolyl geometries obtained from B3LYP/6-311++G(d,p) calculations.

Mode	Symmetry	1-Pyrazolide	1-Pyrazolyl		
		$^1A_1$ Frequency (cm^{-1})	$^2A_2$ Frequency (cm^{-1})	$^2B_1$ Frequency (cm^{-1})	$^2B_2$ Frequency (cm^{-1})
ν_1	a_1	3194	3269	3234	3285
ν_2	a_1	3148	3235	3212	3243
ν_3	a_1	1471	1510	1521	1609
ν_4	a_1	1215	1390	1300	1391
ν_5	a_1	1127	1121	1054	1199
ν_6	a_1	1026	1007	924	1075
ν_7	a_1	930	912	786	913
ν_8	a_2	756	835	859	794
ν_9	a_2	693	564	188	286*i*
ν_{10}	b_1	785	860	882	863
ν_{11}	b_1	696	700	705	765
ν_{12}	b_1	631	408	480	101
ν_{13}	b_2	3151	3239	3216	3279
ν_{14}	b_2	1404	1336	1477	1422
ν_{15}	b_2	1363	1287	1283	1283
ν_{16}	b_2	1165	990	1180	1161
ν_{17}	b_2	1031	950	946	1039
ν_{18}	b_2	914	599	539	627

Table 6.3 1-Pyrazolide and 1-pyrazolyl fundamental vibrational frequencies obtained from B3LYP/6-311++G(d,p) calculations.

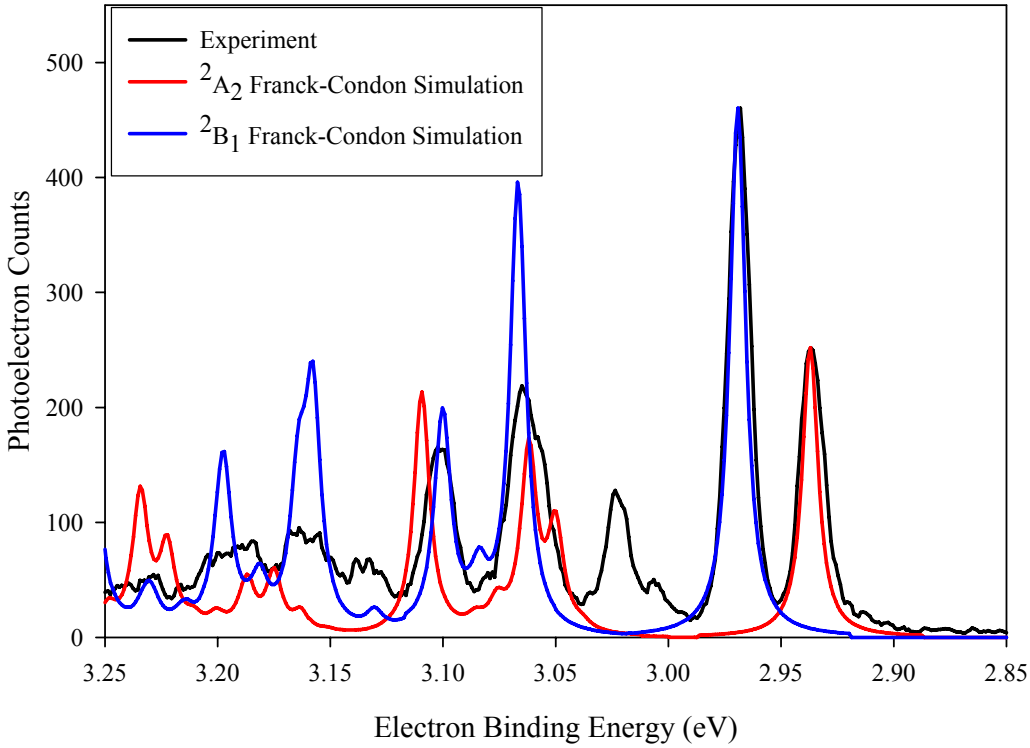

Figure 6.4 Franck-Condon simulation of detachment of 1-pyrazolide. The red curve is the simulation for detachment to $^2A_2$ 1-pyrazolyl, the blue curve is the simulation for detachment to $^2B_1$ 1-pyrazolyl.

of the model Hamiltonian is accomplished with *ab initio* calculations using the equations-of-motion coupled-cluster theory (EOMIP-CCSD).[8, 9] The simulation reproduces the observed spectrum very well and confirms the assignment of the origin peak is correct; that is, the ground state of 1-pyrazolyl is $^2A_2$ and $^2B_1$ is the first excited state. Details of this simulation procedure as well as the results of the simulation will be presented in a forthcoming paper.[10]

As explained before, the lower eBE portion of the spectrum in Figure 6.1 is attributed to detachment from 5-pyrazolide. Figure 6.5 shows an expanded view of the lower energy portion of the photoelectron spectrum of pyrazolide produced from the HO^- reaction with pyrazole. The experimental conditions for this spectrum are virtually identical with those from Figure 6.1, but with a longer data integration time. Table 6.4 lists the observed peak positions of peaks labeled in Figure 6.5. Angular measurements yield an anisotropy parameter of 0.35 ± 0.05 for the features in Figure 6.5. DFT calculations were carried out to obtain the optimized geometries and harmonic vibrational frequencies of the 5-pyrazolide anion and 5-pyrazolyl ground states. The calculations find minima in C_s symmetry for the electronic ground states of both 5-pyrazolide ($^1A'$) and 5-pyrazolyl ($^2A'$). The optimized geometries are listed in Table 6.4 and the frequencies are listed in Table 6.5. The DFT calculations predict an EA of 5-pyrazolyl of 2.109 eV, very close to the experimental peak at 2.104 ± 0.005 eV.

Using these results, a Franck-Condon simulation was performed for the transition from 5-pyrazolide to 5-pyrazolyl and is depicted in Figure 6.6, where the agreement with the experimental spectrum is nearly perfect. This simulation utilizes a vibrational temperature of 400 K for the anion, and shows a small hot-band transition near a binding energy of 2.0 eV, corresponding to one quanta of an in-plane C4-C5-N1 bending mode (ν_{13}) of 5-pyrazolide; the experimental frequency of this mode is 880 ± 20 cm^{-1}. The Franck-Condon simulation identifies the peak labeled *a* in Figure 6.5 as the band origin and also predicts three vibrations

to be strongly active in the photoelectron spectrum, ν_6, ν_9, and ν_{12}. There is also some activation of the ν_{13} vibrational mode which does not become significant until higher quantum numbers. This mode is very close in frequency to ν_{12} and not resolvable in the experimental spectrum. The experimental fundamental frequencies of 890 ± 15, 1110 ± 35, and 1345 ± 30 cm^{-1} compare well with the ν_{12}, ν_9, and ν_6 DFT frequencies of 914, 1162, and 1372, respectively. These modes correspond to ring breathing, asymmetric C3-C4-C5 stretching, and C4-C5-N1 bending, respectively. The DFT computed atomic displacements for these modes are depicted in Figure 6.7. Table 6.4 summarizes the assignments of the 5-pyrazolide photoelectron spectrum.

6.4 Discussion

As mentioned in the results section, the photoelectron spectrum of 1-pyrazolide demonstrates noadiabatic effects in the low-lying electronic states of 1-pyrazolyl. This subject will be discussed in detail elsewhere,[10] so only a brief, qualitative account will be given here.

Comparing 1-pyrazolide with 1-imidazolide, the change in arrangement of the N atoms in the 5-membered ring affects the energetic relationship between the highest occupied molecular orbitals. In 1-imidazolide, the highest occupied π molecular orbital has b_1 symmetry (within the C_{2v} point group), and is mainly composed of C atom p orbitals. The next highest occupied π molecular orbital of 1-imidazolide has a_2 symmetry, and has large contributions from N atom p orbitals which stabilize this molecular orbital by a large amount. This results in a $^2B_1$ ground state and a $^2A_2$ excited state for 1-imidazolyl radical with a large energy separation between these two states. This large spacing leads to very small nonadiabatic effects in the ground state around its equilibrium geometry, with little effect on the photoelectron spectrum.

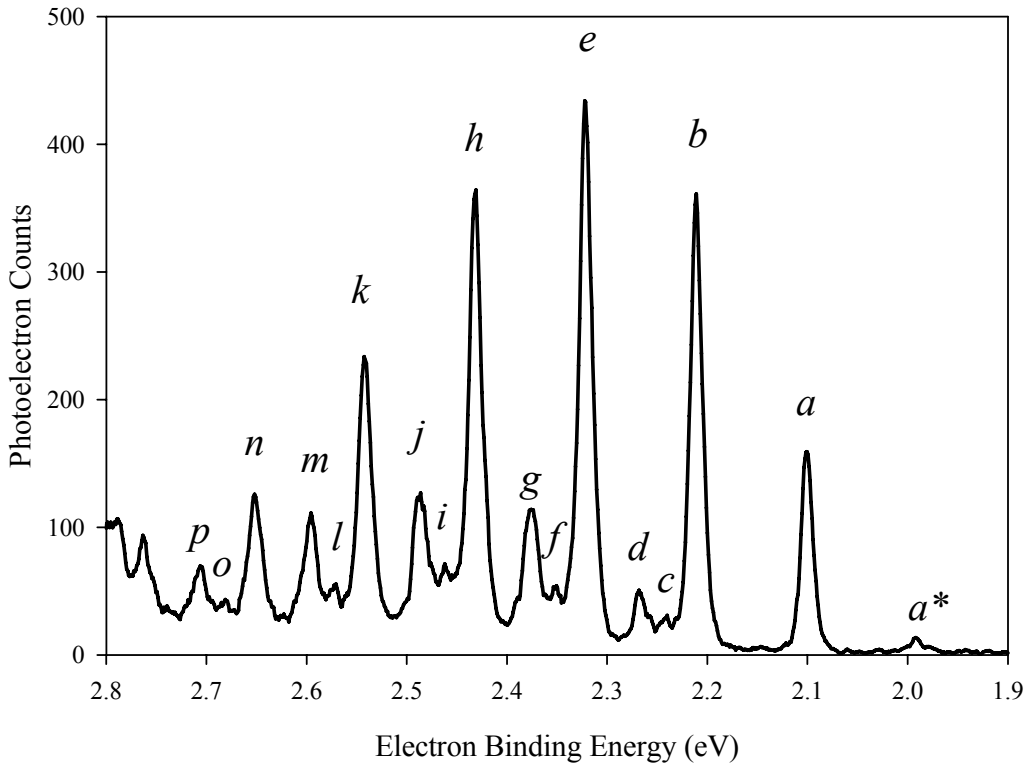

Figure 6.5 351.1 nm magic angle photoelectron spectrum of 5-pyrazolide produced in the reaction of HO^- with pyrazole.

Peak Label	Peak Position Relative to peak a (cm^{-1})	assignment
*a**	-880 ± 20	13_1^0
a	0	0_0^0
b	890 ± 15	12_0^1
c	1110 ± 35	9_0^1
d	1345 ± 30	6_0^1
e	1780 ± 20	12_0^2
f	1990 ± 35	$9_0^1 12_0^1$
g	2225 ± 35	$6_0^1 12_0^1$
h	2665 ± 25	12_0^3
i	2990 ± 50	$9_0^1 12_0^2$
j	3115 ± 25	$6_0^1 12_0^2$
k	3555 ± 35	12_0^4
l	3790 ± 35	$9_0^1 12_0^3$
m	4000 ± 45	$6_0^1 12_0^3$
n	4440 ± 35	12_0^5
o	4670 ± 35	$9_0^1 12_0^4$
p	4880 ± 35	$6_0^1 12_0^4$

Table 6.4 Experimental peak positions and assignments for peaks appearing in the photoelectron spectrum of 5-pyrazolide (Figure 6.5).

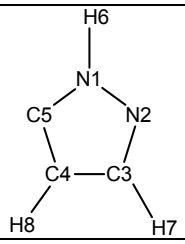		5-Pyrazolide	5-Pyrazolyl
Electronic State		^{1}A'	^{2}A'
N—N Bonds (Å)	1-2	1.380	1.363
N—C Bonds (Å)	1-5	1.371	1.340
	2-3	1.335	1.333
C—C Bonds (Å)	3-4	1.414	1.417
	4-5	1.412	1.374
C—H Bonds (Å)	1-6	1.006	1.006
	3-7	1.086	1.080
	4-8	1.084	1.076
∠NNC (°)	1-2-3	101.7	104.4
∠NCC (°)	2-3-4	111.7	112.8
∠CCC (°)	3-4-5	108.5	102.2
∠CCN (°)	4-5-1	100.1	109.8
∠CNN (°)	5-1-2	118.1	110.8
∠NNH (°)	2-1-6	116.6	119.9
∠NCH (°)	2-3-7	118.9	119.1
∠CCH (°)	5-4-8	125.6	128.5

Table 6.5 5-Pyrazolide and 5-pyrazolyl geometries obtained from B3LYP/6-311++G(d,p) calculations.

Mode	Symmetry	5-Pyrazolide $^1A'$ Frequency (cm^{-1})	5-Pyrazolyl $^2A'$ Frequency (cm^{-1})
ν_1	a'	3654	3676
ν_2	a'	3175	3275
ν_3	a'	3149	3232
ν_4	a'	1492	1526
ν_5	a'	1391	1442
ν_6	a'	1348	1372
ν_7	a'	1247	1317
ν_8	a'	1178	1261
ν_9	a'	1104	1162
ν_{10}	a'	1056	1048
ν_{11}	a'	1030	1038
ν_{12}	a'	922	914
ν_{13}	a'	901	886
ν_{14}	a"	840	884
ν_{15}	a"	753	770
ν_{16}	a"	696	670
ν_{17}	a"	650	572
ν_{18}	a"	527	440

Table 6.6 5-Pyrazolide and 5-pyrazolyl fundamental vibrational frequencies obtained from B3LYP/6-311++G(d,p) calculations.

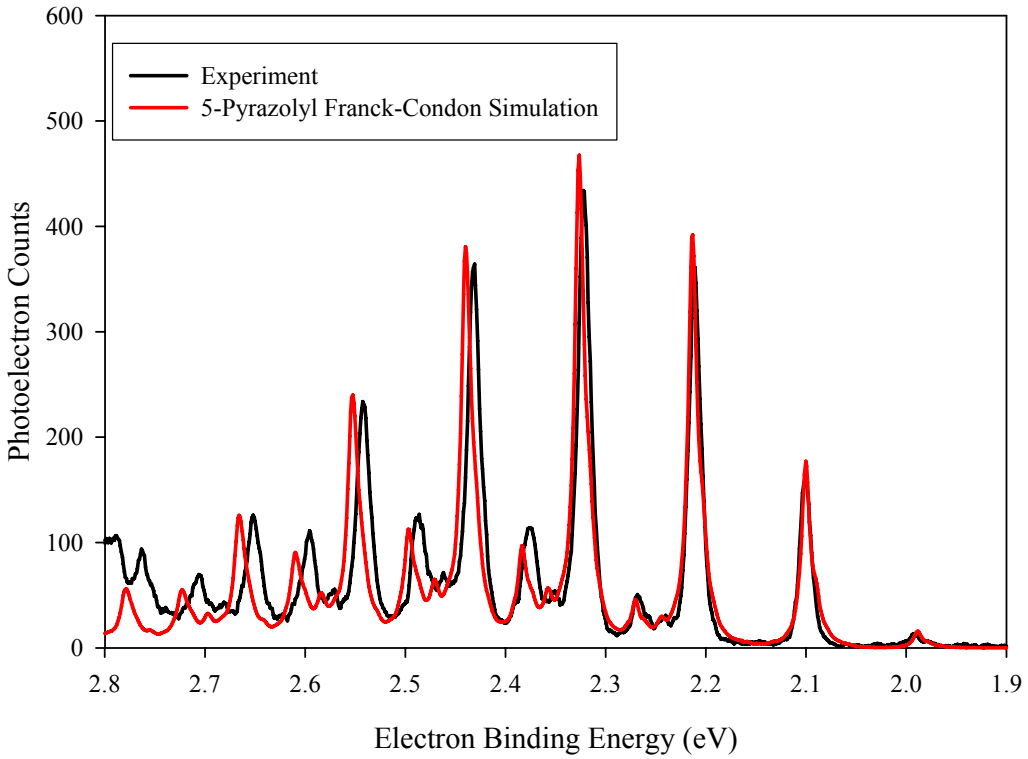

Figure 6.6 Franck-Condon simulation (red) of detachment of 5-pyrazolide based on the optimized geometries and vibrational frequencies obtained from the B3LYP/6-311++G(d,p) calculations overlaid on the experimental spectrum (black).

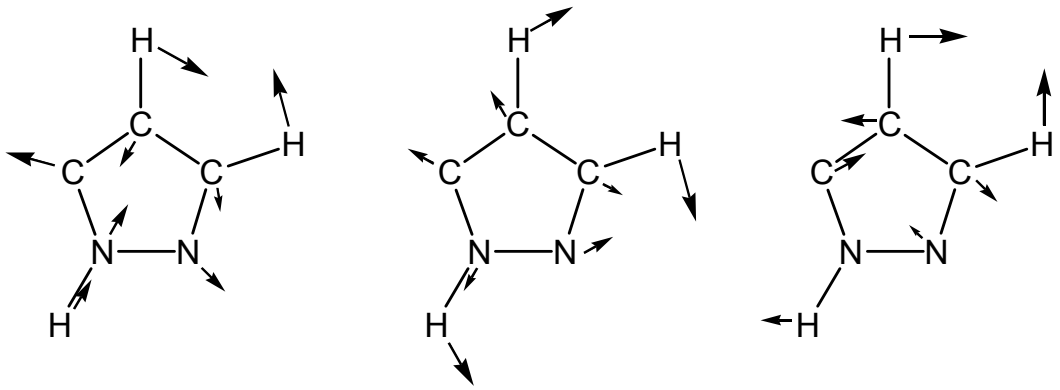

a' mode, 914 cm^{-1}
ring distortion

a' mode, 1162 cm^{-1}
ring breathing

a' mode, 1372 cm^{-1}
C-C stretch

Figure 6.7 Relative atomic displacements and harmonic frequencies of normal modes of 5-pyrazolyl active in the photoelectron spectrum evaluated at the B3LYP/6-311++G(d,p) level of theory.

With the N atoms adjacent in the 1-pyrazolide ring, the energetic relationship between the two highest occupied π orbitals is changed. Figure 6.8 illustrates the photodetachment process for 1-pyrazolide. Here, both the a_2 and b_1 orbitals have comparable contributions from the p orbitals of the two N atoms, resulting in π orbitals which are very close in energy. Thus the $^2A_2$ and $^2B_1$ states of 1-pyrazolyl, formed by electron detachment from the corresponding orbitals of 1-pyrazolide, are nearly degenerate. Because they are so close in energy, vibronic interactions of the pseudo-Jahn-Teller type[11, 12] (a.k.a. vibronic coupling) between the two π states becomes significant around the equilibrium geometries of both states. Therefore, Franck-Condon simulation based on the Born-Oppenheimer approximation fails, as seen in Figure 6.4. The near-degeneracy might have prevented observation of a clear electron spin resonance spectrum of 1-pyrazolyl radical in alkaline aqueous solution.[13] Further vibronic interactions arise from the participation of another nearby electronic state, $^2B_2$, as shown in Figure 6.8. This three-state[14] interaction will be fully investigated in a forthcoming paper.[10]

The change in the arrangement of the N atoms and, thus, the highest occupied molecular orbitals also becomes apparent in the EA of 1-pyrazolyl radical. Since the highest occupied molecular orbital has large contributions from N atom p orbitals, it is stabilized, resulting in a larger EA for 1-pyrazolyl when compared with 1-imidazolyl (2.938 ± 0.005 eV vs. 2.613 ± 0.006 eV).

Using Equation 2.3, the EA of 1-pyrazolyl can be combined in a thermodynamic cycle with the pyrazole deprotonation enthalpy[1] ($\Delta_{acid}H_0$ = 106.4 ± 0.4 kcal mol^{-1}) to obtain the pyrazole N—H bond dissociation energy: D_0 = 106.4 ± 0.4 kcal mol^{-1}. With the 298 K heat of formation of pyrazole[15] [$\Delta_f H_{298}$(pyrazole) = 42.88 ± 0.20 kcal mol^{-1}], and thermal corrections from the DFT calculations, the heat of formation of 1-pyrazolyl radical can now be determined using Equation 2.5: $\Delta_f H_{298}$(1-pyrazolyl) = 98.7 ± 0.5 kcal mol^{-1}.

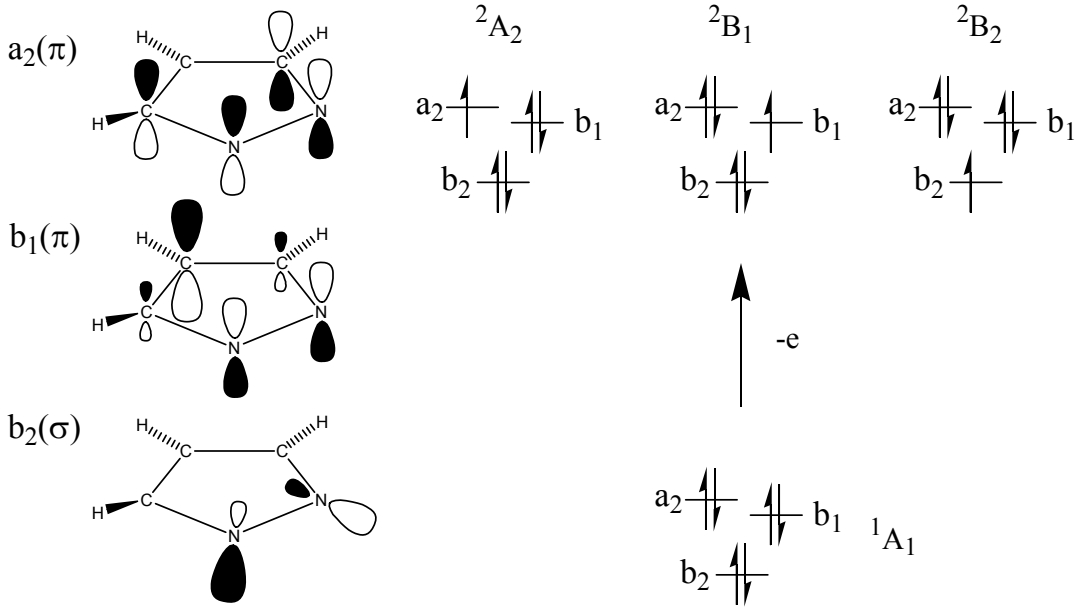

Figure 6.8 Three highest occupied molecular orbitals of 1-pyrazolide and the schematic representation of electron photodetachment from 1-pyrazolide to form three electronic states of 1-pyrazolyl.

In a similar way, the pyrazole C5—H bond dissociation energy can be obtained if the pyrazole C5—H deprotonation enthalpy is available. The results described above indicate that 5-pyrazolide was formed in the flow tube by HO^- deprotonation of pyrazole but it was not formed in the flow tube when O^- or F^- was used as the deprotonation agent. This observation allows bracketing of the pyrazole C5—H gas phase acidity between that of H_2O[3] (383.68 ± 0.02 kcal mol^{-1}) and HO[4] (376.7 ± 0.2 kcal mol^{-1}) or HF[3] (365.577 ± 0.003 kcal mol^{-1}). This yields a pyrazole C5—H gas phase acidity of $\Delta_{acid}G_{298}$ = 380 ± 4 kcal mol^{-1}. With thermal corrections from the DFT calculations, Equation 2.3 yields the pyrazole C5—H bond dissociation energy: D_0 = 121 ± 4 kcal mol^{-1}. Similar to above, the 5-pyrazolyl radical heat of formation can be determined using Equation 2.5: $\Delta_f H_{298}$(5-pyrazolyl) = 113 ± 4 kcal mol^{-1}.

Reaction 6.1 below shows proton transfer between 5-imidazolide and pyrazole to form imidazole and 5-pyrazolide. The C5 proton acidity of imidazole was bracketed between the acidities of H_2O and HO, identical to that of the C5 proton of pyrazole described above, resulting in identical gas phase acidities for the C5 protons of imidazole and pyrazole. Taft and coworkers developed an electrostatic model[16, 17] to predict the difference in acidity between different nitrogen heterocycles. This model predicts a difference in acidity between the C5 protons of imidazole and pyrazole of zero. The DFT predicted free energy difference for Reaction 6.1 is –3.5 kcal mol^{-1}. The observation of larger photoelectron intensities from 5-pyrazolide versus 5-imidazolide may also support the idea that the C5 position of pyrazole is slightly more acidic than that of imidazole.

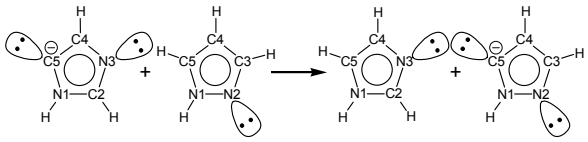

$$\Delta_{rxn}G_{298} = 0 \pm 6 \text{ kcal mol}^{-1} \qquad (6.1)$$

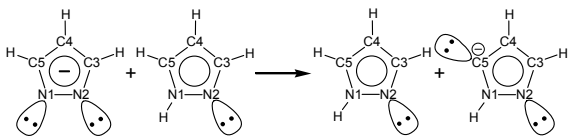

$$\Delta_{rxn}G_{298} = 33.6 \pm 4.0 \text{ kcal mol}^{-1} \quad (6.2)$$

Reaction 6.2 represents proton transfer between pyrazolide and pyrazole to form pyrazole and 5-pyrazolide. The large difference in acidity between the N1 and C5 positions of pyrazole[1] can easily be recognized as arising from extensive conjugation in 1-pyrazolide which is not present in 5-pyrazolide. In 1-pyrazolide, the negative charge is free to move around the ring (see Figure 6.9); in 5-pyrazolide, however, the negative charge is effectively localized on C5.

6.5 Conclusion

The photoelectron spectrum of 1-pyrazolide has been measured, and the EA of the 1-pyrazolyl radical is determined to be 2.938 ± 0.005 eV, with a $^2A_2$ ground state. Combining the EA in a thermodynamic cycle with the pyrazole N—H deprotonation enthalpy, the N—H bond dissociation energy of pyrazole is determined to be 106.4 ± 0.4 kcal mol^{-1}. The photoelectron spectrum of 1-pyrazolide indicates non-adiabatic effects are significant between low-lying states of 1-pyrazolyl, based on the poor agreement of the Franck-Condon simulations with the experimental spectrum. A term energy for the 1-pyrazolyl first excited state ($^2B_1$) of 0.032 ± 0.001 eV is also observed. The detailed analysis of the vibronic structure of the 1-pyrazolide photoelectron spectrum will be given in a separate paper.[10]

The HO^- deprotonation of pyrazole yields a minor product ion, 5-pyrazolide, as identified by Franck-Condon fitting of the photoelectron spectrum based on the results of B3LYP/6-311++G(d,p) DFT calculations. The EA of 5-pyrazolyl radical is 2.104 ± 0.005 eV. Fundamental vibrational frequencies of 890 ± 15, 1110 ± 35, and 1345 ± 30 cm^{-1} have been assigned to an in-plane CCN bending mode and two in-plane ring stretching modes,

respectively of ^{2}A' 5-pyrazolyl. An extensive vibrational progression appears in the spectrum, suggesting a substantial change in the CCN angle from the anion to the neutral. This change in angle is corroborated by the DFT calculations. Formation of 5-pyrazolide is not observed in the O^- or F^- reactions with pyrazole, which allows the gas phase acidity of the pyrazole C5—H to be bracketed between the acidities of H_2O and HO, yielding $\Delta_{acid}G_{298}$(pyrazole, C5—H) = 380 ± 4 kcal mol^{-1}. The EA of 5-pyrazolyl and the pyrazole C5—H gas phase acidity are combined in a thermodynamic cycle to yield the C5—H bond dissociation energy of pyrazole D_0 = 121 ± 4 kcal mol^{-1}. To more precisely determine a C5-H bond dissociation energy, experiments on 1-methylpyrazole are currently underway.[18]

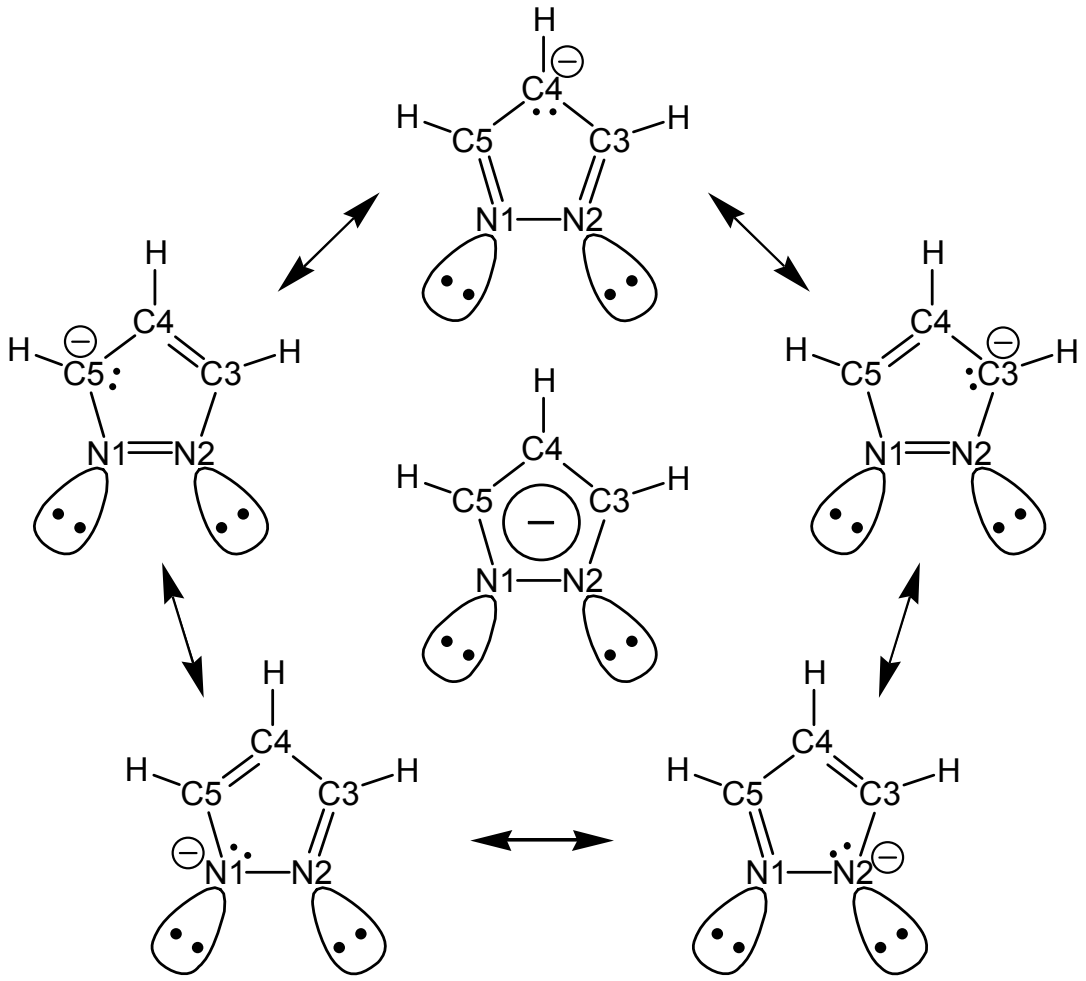

Figure 6.9 Resonance structures of 1-pyrazolide showing migration of the negative charge around the ring.

Chapter 6 References

[1] A.J. Gianola, T. Ichino, S. Kato, V.M. Bierbaum, and W.C. Lineberger, *Thermochemical Studies of Pyrazolide.* Journal of Physical Chemistry A, 2006. 10.1021/jp057499+.

[2] D. Hanstorp and M. Gustafsson, *Determination of the Electron-Affinity of Iodine.* Journal of Physics B-Atomic Molecular and Optical Physics, 1992. **25**(8): p. 1773-1783.

[3] K.M. Ervin and V.F. DeTuro, *Anchoring the gas-phase acidity scale.* Journal of Physical Chemistry A, 2002. **106**(42): p. 9947-9956.

[4] J.E. Bartmess, *"Negative Ion Energetics Data"*, in *NIST Chemistry Webbook, NIST Standard Reference Database Number 69*, J.P. Linstrom and W.G. Mallard, Editors. June 2005, National Institue of Standards and Technology: Gaithersburg MD, 20899.

[5] H. Koppel, W. Domcke, and L.S. Cederbaum, *Multimode Molecular-Dynamics Beyond the Born-Oppenheimer Approximation.* Advances in Chemical Physics, 1984. **57**: p. 59-246.

[6] Y.J. Bomble, K.W. Sattelmeyer, J.F. Stanton, and J. Gauss, *On the vertical excitation energy of cyclopentadiene.* Journal of Chemical Physics, 2004. **121**(11): p. 5236-5240.

[7] A. Hazra and M. Nooijen, *Comparison of various Franck-Condon and vibronic coupling approaches for simulating electronic spectra: The case of the lowest photoelectron band of ethylene.* Physical Chemistry Chemical Physics, 2005. **7**(8): p. 1759-1771.

[8] J.F. Stanton and J. Gauss, *Analytic Energy Derivatives for Ionized States Described by the Equation-of-Motion Coupled-Cluster Method.* Journal of Chemical Physics, 1994. **101**(10): p. 8938-8944.

[9] J.F. Stanton, *Coupled-cluster theory, pseudo-Jahn-Teller effects and conical intersections.* Journal of Chemical Physics, 2001. **115**(22): p. 10382-10393.

[10] T. Ichino, A.J. Gianola, W.C. Lineberger, and J.F. Stanton, *Nonadiabatic effects in the photoelectron spectrum of the pyrazolide anion: Three-state interactions of the pyrazolyl radical.* Submitted.

[11] R.G. Pearson, *A symmetry rule for predicting molecular structure.* Journal of the American Chemical Society, 1969. **91**: p. 4947-4955.

[12] G. Fischer, *Vibronic Coupling*. 1984, London: Academic Press.

[13] A. Samuni and P. Neta, *Electron-Spin Resonance Study of Reaction of Hydroxyl Radicals with Pyrrole, Imidazole, and Related Compounds.* Journal of Physical Chemistry, 1973. **77**(13): p. 1629-1635.

[14] S. Matsika and D.R. Yarkony, *Conical intersections of three electronic states affect the ground state of radical species with little or no symmetry: Pyrazolyl.* Journal of the American Chemical Society, 2003. **125**(41): p. 12428-12429.

[15] P. Jimenez, M.V. Roux, C. Turrion, and F. Gomis, *Thermochemical Properties of N-Heterocyclic Compounds .1. Enthalpies of Combustion, Vapor-Pressures and Enthalpies of Sublimation, and Enthalpies of Formation of Pyrazole, Imidazole, Indazole, and Benzimidazole.* Journal of Chemical Thermodynamics, 1987. **19**(9): p. 985-992.

[16] R.W. Taft, F. Anvia, M. Taagepera, J. Catalan, and J. Elguero, *Electrostatic Proximity Effects in the Relative Basicities and Acidities of Pyrazole, Imidazole, Pyridazine, and Pyrimidine.* Journal of the American Chemical Society, 1986. **108**(12): p. 3237-3239.

[17] J. Catalan, R.M. Claramunt, J. Elguero, J. Laynez, M. Menendez, F. Anvia, J.H. Quian, M. Taagepera, and R.W. Taft, *Basicity and Acidity of Azoles - the Annelation Effect in Azoles.* Journal of the American Chemical Society, 1988. **110**(13): p. 4105-4111.

[18] S.M. Villano, A.J. Gianola, S. Kato, V.M. Bierbaum, and W.C. Lineberger, *Manuscript in preparation.*

7 Vinyldiazomethyl Anion, $C_3H_3N_2^-$

7.1 Introduction

Formation of substituted and unsubstituted pyrazoles can be accomplished by reactions of alkynes with diazomethanes.[1-3] Both 1H- and 3H- pyrazoles are formed from these reactions. Once formed, 1H-pyrazoles have very stable ring structures, due to their aromatic character, but collision induced dissociation (CID) studies of 1-pyrazolide have shown ring opening followed by rapid fragmentation.[4] The ring opening typically results from rupture of the N—N bond. Thermal ring opening of the non-aromatic 3H-pyrazole compounds at a C—N bond to form vinyldiazo compounds has been known for quite some time.[3] Ring opening is most likely when steric effects favor it, as well as when the resulting vinyldiazo compound is stabilized by conjugation. These vinyldiazo compounds are often an intermediate to loss of N_2 and formation of a vinylcarbene, followed by subsequent cyclopropene formation.

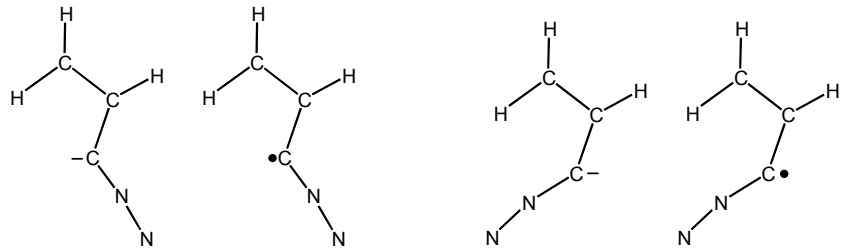

E-Vinyldiazomethyl Anion | E-Vinyldiazomethyl Radical | Z-Vinyldiazomethyl Anion | Z-Vinyldiazomethyl Radical

Bierbaum and coworkers succeeded in synthesizing deprotonated vinyldiazomethane (the vinyldiazomethyl anion) in the gas phase in 1977.[5] The vinyldiazomethyl anion, a ring opened isomer of pyrazolide and imidazolide, was synthesized in the flow tube here and its photoelectron spectrum has been measured. The method used for its synthesis is briefly reviewed, and is followed by a description of the experimental spectra obtained. DFT

calculations suggest that two isomers of the vinyldiazomethyl anion should be formed in the flow tube, but Franck-Condon simulations show that only one is formed in detectable amounts. The thermodynamics of ring closure of vinyldiazomethane and the vinyldiazomethyl anion are discussed.

7.2 Experiment

Vinyldiazomethyl anions are produced in a three step process by first reacting O^- with an excess amount of propene (C_3H_6) introduced downstream of the microwave discharge to produce HO^- in a hydrogen transfer reaction, similar to the reaction of O^- with methane:

$$O^- + C_3H_6 \rightarrow HO^- + C_3H_5 \tag{7.1}$$

The propene which remains unreacted is deprotonated by HO^- to produce allyl anions ($C_3H_5^-$):

$$HO^- + C_3H_6 \rightarrow H_2O + C_3H_5^- \tag{7.2}$$

A trace amount of nitrous oxide (N_2O) is added further downstream, which reacts with the allyl anions to produce vinyldiazomethyl anions ($C_3H_3N_2^-$) and water:[5-8]

$$N_2O + C_3H_5^- \rightarrow C_3H_3N_2^- + H_2O \tag{7.3}$$

This method produces vinyldiazomethyl anion beams of ~200 pA. The laser wavelength used for photodetachment of vinyldiazomethyl anion was 351.1 nm, and the absolute energy scale was calibrated via the measurement of the EA of oxygen. In some experiments liquid nitrogen was used to cool the flow tube to aid in cooling the ions.

7.3 Results

The 351.1 nm magic angle spectrum of the vinyldiazomethyl anion at 298 K is shown in Figure 7.1. The spectrum shows two regions of detachment, one between binding energies of 1.7 and 2.4 eV and one between binding energies of 2.4 and 3.4 eV. Angular distribution

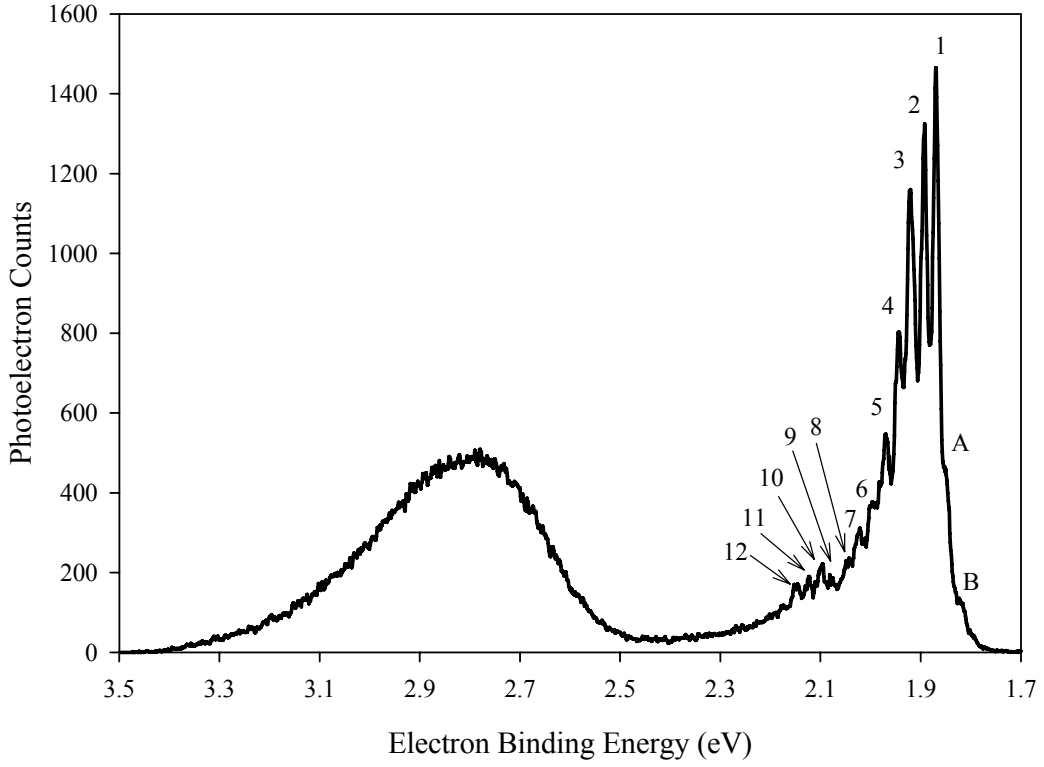

Figure 7.1 351.1 nm magic angle photoelectron spectrum of vinyldiazomethyl anion at 298 K. See Table 7.1 for assignments of labels.

Peak Label	Relative Peak Position (cm^{-1})	E-Vinyldiazomethyl Assignment
B	-414 ± 20	12_1^0
A	-179 ± 15	13_1^0
1	0	0_0^0
2	189 ± 10	13_0^1
3	410 ± 15	12_0^1
4	607 ± 15	$12_0^1 13_0^1$
5	818 ± 20	$12_0^1 13_0^2$
6	1030 ± 25	$12_0^2 13_0^1$
7	1250 ± 25	8_0^1
8	1451 ± 25	$8_0^1 13_0^1$
9	1687 ± 30	$8_0^1 12_0^1$
10	1868 ± 30	4_0^1
11	2051 ± 35	$4_0^1 13_0^1$
12	2273 ± 35	$4_0^1 12_0^1$

Table 7.1 Relative experimental peak positions and assignments for the peaks labeled in Figures 7.1 and 7.2.

measurements reveal different anisotropies for the different portions of the spectra. For the lower binding energy region, $\beta = 0.0 \pm 0.1$; for the higher binding energy region, $\beta = 0.52 \pm 0.06$. This suggests that the two different regions correspond to detachment to two different electronic states of vinyldiazomethyl radical.

The lower binding energy region shows resolvable vibrational structure, and the tallest peak is assigned as the band origin, yielding an EA of 1.867 ± 0.007 eV. Table 7.1 summarizes the relative peak positions for peaks labeled in Figures 7.1 and 7.2. The higher binding energy region has a vertical detachment energy of 2.809 ± 0.010 eV. It is very broad and without clearly resolvable structure, indicating that there is a large geometry change upon photodetachment to this state. It is not possible to precisely determine the band origin of this state, but the term energy is estimated as 0.6 eV – near the region where the photoelectron signals of this band begin.

To further aid in the assignments of the photoelectron spectrum, DFT calculations were performed on the vinyldiazomethyl anion and vinyldiazomethyl radical at the B3LYP/6-311++G(d,p) level. Ground state geometry optimizations and frequency calculations were performed which located E,Z isomers of the vinyldiazomethyl anion and radical. Minima of C_s symmetry were located for both isomers of the anion and the radical. The optimized geometries are listed in Table 7.2 and the frequencies are listed in Table 7.3. These radical states have a' (σ) electronic symmetry, which is consistent with the anisotropy observed for this portion of the spectrum. The E- and Z- labels reflect the positions of atoms relative to the C3—C4 bond. The DFT calculations predict an EA for E-vinyldiazomethyl radical of 1.869 eV and an EA for Z-vinyldiazomethyl radical of 1.872 eV. If formed in the flow tube, both isomers are expected to contribute to the photoelectron spectrum.

Using the geometry and frequency results, Franck-Condon simulations were performed for transitions from the E- or Z-vinyldiazomethyl anion to the E- or

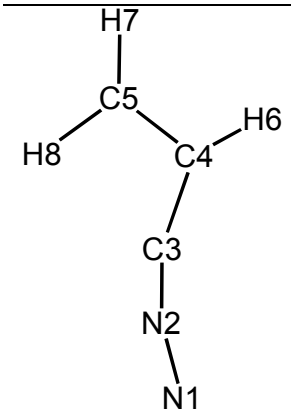	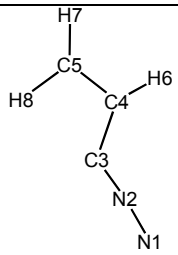 E-Vinyldiazomethyl		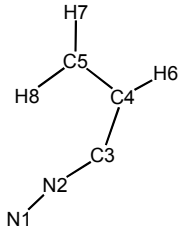 Z-Vinyldiazomethyl	
	Anion	radical	anion	Radical
Electronic State	^{1}A'	^{2}A'	^{1}A'	^{2}A'
N1—N2 (Å)	1.1690	1.1507	1.1671	1.1503
N2—C3 (Å)	1.2654	1.2815	1.2670	1.2803
C3—C4 (Å)	1.4243	1.4185	1.4298	1.4205
C4—C5 (Å)	1.3629	1.3586	1.3668	1.3609
C4—H6 (Å)	1.1009	1.0907	1.0925	1.0853
C5—H7 (Å)	1.0853	1.0834	1.0864	1.0839
C5—H8 (Å)	1.0858	1.0836	1.0861	1.0848
∠N1-N2-C3 (°)	186.77	189.98	173.15	169.88
∠N2-C3-C4 (°)	121.14	122.34	238.05	236.16
∠C3-C4-C5 (°)	127.42	121.16	130.16	126.01
∠C3-C4-H6 (°)	116.86	119.94	114.10	115.32
∠C4-C5-H7 (°)	121.01	121.27	120.86	121.01
∠C4-C5-H8 (°)	121.22	120.58	121.91	121.78

Table 7.2 E- and Z-vinyldiazomethyl anion and radical geometries obtained from B3LYP/6-311++G(d,p) calculations.

Mode	Symmetry	E-Vinyldiazomethyl		Z-Vinyldiazomethyl	
		Anion $^1A'$ Frequency (cm^{-1})	Radical $^2A'$ Frequency (cm^{-1})	Anion $^1A'$ Frequency (cm^{-1})	Radical $^2A'$ Frequency (cm^{-1})
ν_1	a'	3190	3244	3181	3230
ν_2	a'	3111	3146	3103	3161
ν_3	a'	2959	3095	3057	3136
ν_4	a'	2034	1955	2026	1951
ν_5	a'	1599	1540	1565	1542
ν_6	a'	1465	1425	1460	1421
ν_7	a'	1353	1366	1395	1376
ν_8	a'	1290	1288	1287	1293
ν_9	a'	1109	1100	1074	1073
ν_{10}	a'	897	890	904	888
ν_{11}	a'	622	584	663	615
ν_{12}	a'	445	439	475	469
ν_{13}	a'	183	186	146	158
ν_{14}	a"	962	984	983	1003
ν_{15}	a"	718	945	714	928
ν_{16}	a"	626	635	620	566
ν_{17}	a"	566	477	580	484
ν_{18}	a"	138	137	205	198

Table 7.3 E- and Z-vinyldiazomethyl anion and radical fundamental vibrational frequencies obtained from B3LYP/6-311++G(d,p) calculations.

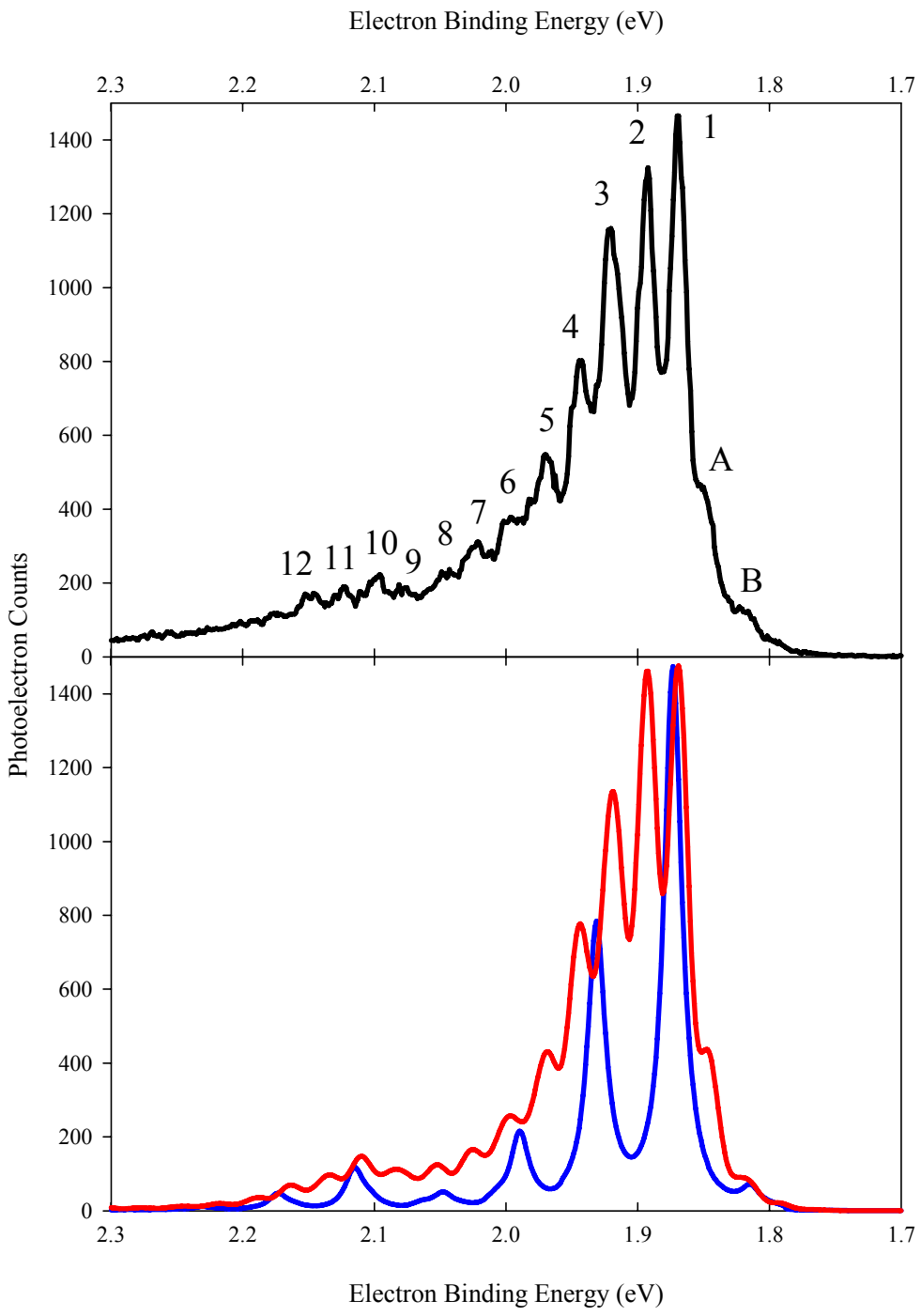

Figure 7.2 Expanded view of the 351.1 nm magic angle photoelectron spectrum of vinyldiazomethyl anion at 298 K (black) and Franck-Condon simulation of detachment of E-vinyldiazomethyl anion (red) and Z-vinyldiazomethyl anion (blue).

Z-vinyldiazomethyl radical. Figure 7.2 shows the Franck-Condon simulation of detachment of E-vinyldiazomethyl anion (red) and Z-vinyldiazomethyl anion (blue), as well as an expanded view of the experimental spectrum (black). To best match the appearance of hot bands in the experimental spectrum, the simulation used a vibrational temperature for the anions of 250 K. The simulations origin positions are set to match the DFT predicted EAs.

From Figure 7.2, it is clear that the spectrum matches the E-vinyldiazomethyl anion detachment simulation nearly perfectly, with little indication of contributions from Z-vinyldiazomethyl anion detachment. The most intense peak is confirmed to be the ground state band origin, verifying the EA of E-vinyldiazomethyl radical as 1.867 ± 0.007 eV. Detachment of E-vinyldiazomethyl anion results in activation of four vibrational modes of E-vinyldiazomethyl radical. The experimental fundamental frequencies extracted from the spectrum of 189 ± 10, 410 ± 15, 1250 ± 25, and 1868 ± 30 cm^{-1} compare well with the corresponding DFT frequencies of 186, 439, 1288, and 1955 cm^{-1}, respectively. Peak assignments are given in Table 7.1 and Figure 7.3 shows the relative atomic displacements for the vibrations active in the photoelectron spectrum.

7.4 Discussion

The Franck-Condon simulation of vinyldiazomethyl anion detachment shows that the photoelectron signals primarily originate from detachment of E-vinyldiazomethyl anion with little contribution from the Z-vinyldiazomethyl anion. The relative intensities of the experimental peaks labeled 1 and 2, however, do not match the relative intensities of the simulation of E-vinyldiazomethyl anion detachment perfectly. Assuming that the total photodetachment cross sections for E- and Z-vinyldiazomethyl anion are identical, if there is a 1:1 ratio of E- and Z-vinyldiazomethyl anion present in the ion beam, the origin intensity of the Z- isomer would be approximately twice that of the E- isomer. With ~7% of the Z-

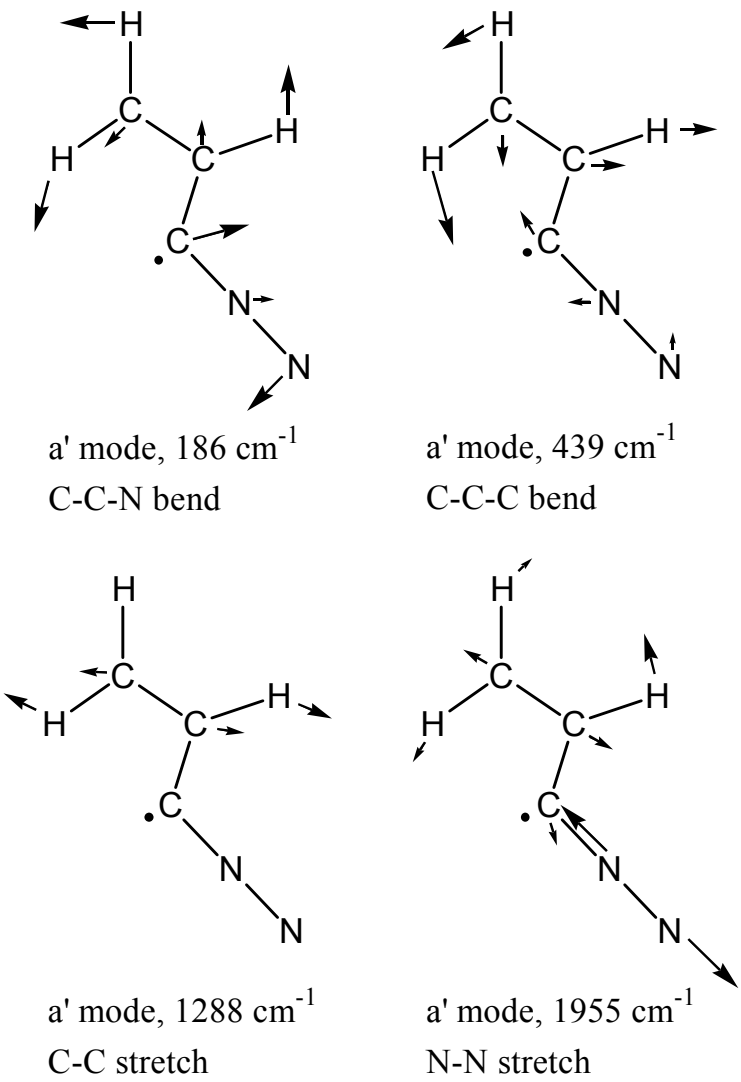

Figure 7.3 Relative atomic displacements and harmonic frequencies of normal modes of E-vinyldiazomethyl radical evaluated at B3LYP/6-311++G(d,p) level.

isomer present in the ion beam, the relative intensities of peaks 1 and 2 are better matched, with only marginal effects on the other features of the spectrum.

Franck-Condon simulations to the excited states of the vinyldiazomethyl radical were not performed here, due to the lower symmetry structures expected for these states. When C_s symmetry was imposed on π-type excited states of the E- and Z-vinyldiazomethyl radicals, only transition states were found. Since the ground states of the E- and Z- vinyldiazomethyl radical have C_s symmetry, any non-planar geometries input into the electronic structure calculations relax to the planar ground states regardless of the molecular orbital population chosen. Time dependent DFT methods were attempted to calculate structures and frequencies for the π-type excited states of the E- and Z-vinyldiazomethyl radicals; however, the processing time required to complete these calculations was prohibitive.

The DFT calculations on the anions suggest that the E-vinyldiazomethyl anion is more stable than Z-vinyldiazomethyl anion by ~1.8 kcal mol^{-1}. For mostly E-vinyldiazomethyl anion to be present in the ion beam suggests a significant barrier to prevent the conversion between the two isomers. DFT calculations were performed to explore the isomerization energetics. A structure of C_1 symmetry was located as the transition state between the E- and Z- vinyldiazomethyl anion isomers. This transition state was located approximately 8 kcal mol^{-1} above E-vinyldiazomethyl anion. This barrier must be large enough for preferential formation or stabilization of mostly the E- isomer in the flow tube.

As mentioned in the introduction, 3H-pyrazoles are known to ring open to form vinyldiazomethanes when heated.[3] Ring closure of deprotonated vinyldiazomethane, then, is expected to form a deprotonated 3H-pyrazole. DFT was again used to explore the energetics of such ring formation. C5 deprotonated 3H-pyrazole is the expected product of ring closure, and a C_s minimum was located for this ion, with an energy approximately 22 kcal mol^{-1} above

E-vinyldiazomethyl anion. A C_1 transition state was located between Z-vinyldiazomethyl anion and C5 deprotonated 3H-pyrazole. This barrier was located approximately 46 kcal mol^{-1} above E-vinyldiazomethyl anion. Such a large endothermicity and barrier suggests it is nearly impossible to form a 5-membered ring anion from vinyldiazomethyl anion under the current flow tube conditions. Figure 7.4 summarizes the potential surface points computed for this proposed ring closure.

Vinyldiazomethane, though, is known to slowly isomerize to 1-H pyrazole under room temperature conditions.[9] Ledwith and Parry[10] and Hart and Brewbaker[11, 12] studied the rate of cyclization and proposed a mechanism which involves 3H-pyrazole as an intermediate. DFT calculations were again used to study the energetics of the ring closing mechanism at various points along the reaction path, beginning with vinyldiazomethane and ending with 1H-pyrazole. According to these calculations, E-vinyldiazomethane is slightly more stable than Z-vinyldiazomethane (~0.6 kcal mol-1), with a barrier similar in height to the deprotonated form (~8 kcal mol^{-1}). The barrier to ring closure and formation of 3H-pyrazole is larger, about 27 kcal mol^{-1}. Overall, production of 3H-pyrazole from vinyldiazomethane is about 6 kcal mol^{-1} exothermic. The barrier to shifting a hydrogen atom from the pyrazole C3 to N1 position is similar to the ring closure barrier, about 27 kcal mol^{-1} higher than 3H-pyrazole. It is ~29 kcal mol^{-1} exothermic to form 1H-pyrazole from 3H-pyrazole. This large stabilization is presumably due to the aromatic character of 1H-pyrazole. These results seem to corroborate the experimental observation of slow formation of 1H-pyrazole from pure vinyldiazomethane. Figure 7.5 summarizes the computed potential surface points for this ring closure.

7.5 Conclusion

The photoelectron spectrum of vinyldiazomethyl anion has been obtained and the EA of vinyldiazomethyl radical is 1.867 ± 0.007 eV. Franck-Condon simulations indicate that the E-vinyldiazomethyl anion isomer is primarily formed in the flow tube; Z-vinyldiazomethyl anion is not formed in significant amounts to contribute to the spectrum. Vibrational frequencies of E-vinyldiazomethyl radical are observed in the photoelectron spectrum of 189 ± 10, 410 ± 15, 1250 ± 25, and 1868 ± 30 cm^{-1}. These modes respectively correspond to C-C-N bending, C-C-C bending, C—C stretching and N—N stretching modes of E-vinyldiazomethyl radical. Comparing the vinyldiazomethyl anion photoelectron spectrum with that of pyrazolide, there are no photoelectrons corresponding to detachment of vinyldiazomethyl anion in the pyrazolide spectrum, nor are there photoelectrons corresponding to detachment of pyrazolide in the vinyldiazomethyl anion spectrum. This indicates that of ring closure in the vinyldiazomethyl anion and ring opening of pyrazolide does not occur in the flow tube. Theoretical calculations suggest formation of pyrazolide in the flow tube is virtually impossible under the experimental conditions.

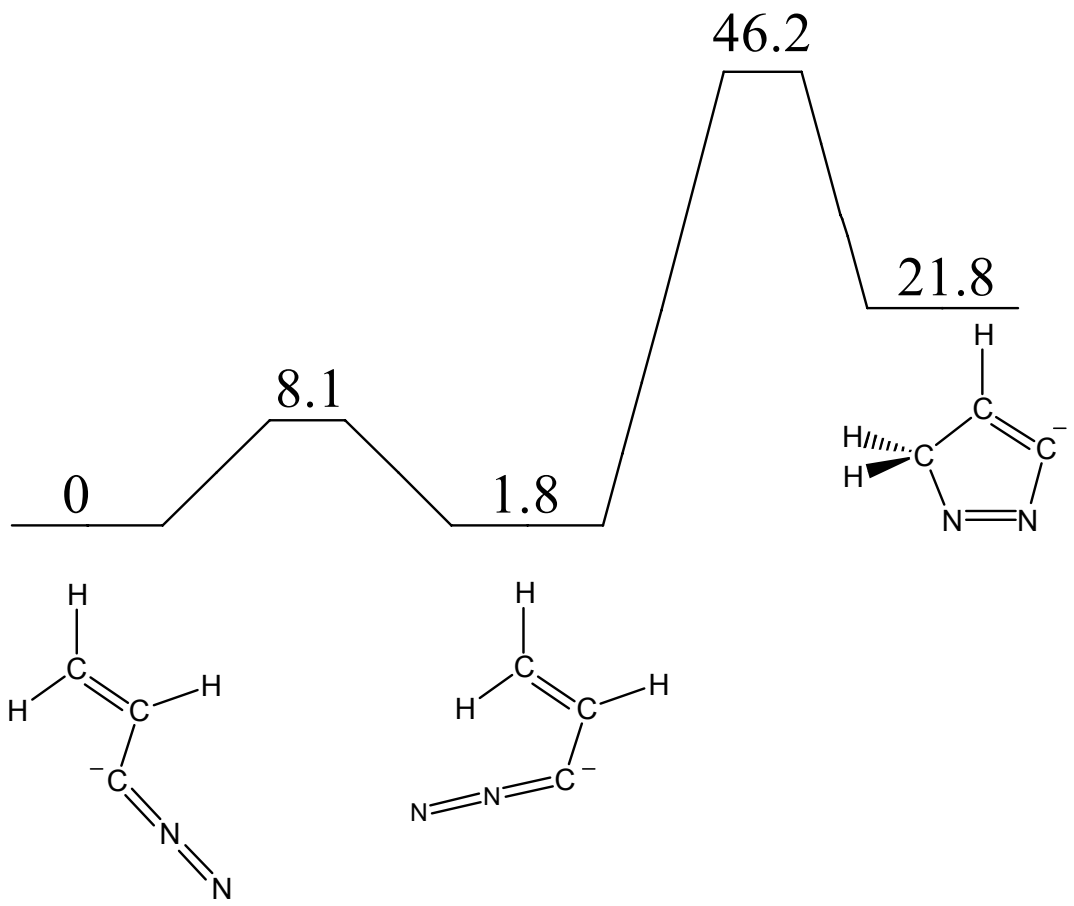

Figure 7.4 Reaction profile for ring-closure of vinyldiazomethyl anion. Potential surface energies are relative to E-vinyldiazomethyl anion and are computed at the B3LYP/6-311++G(d,p) level. Energies are in kcal mol^{-1}.

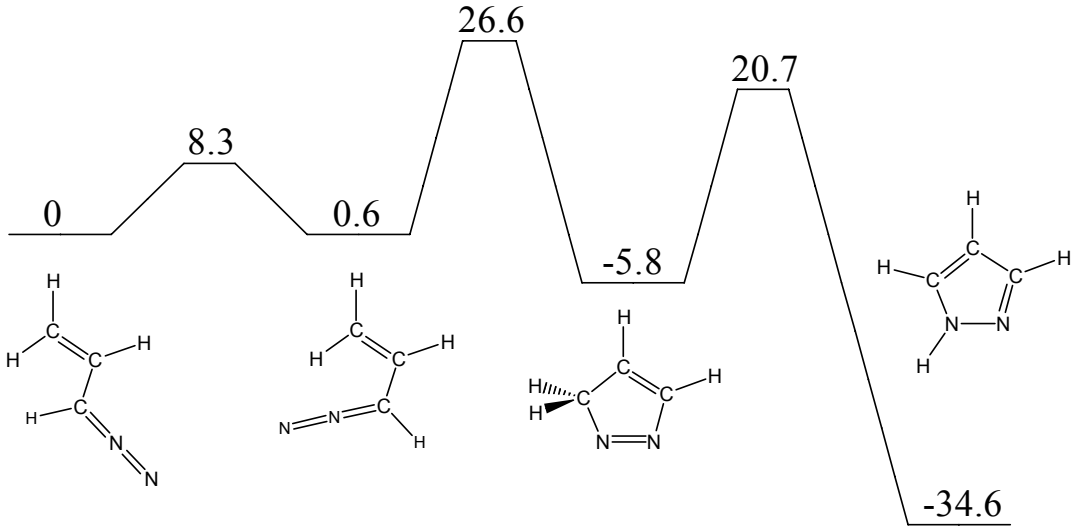

Figure 7.5 Reaction profile for ring-closure of vinyldiazomethane to ultimately form 1H-pyrazole. Potential surface energies are relative to E-vinyldiazomethane and are computed at the B3LYP/6-311++G(d,p) level. Energies are in kcal mol^{-1}.

Chapter 7 References

[1] A.N. Kost and I.I. Grandberg, *Progress in pyrazole chemistry.* Advances in Heterocyclic Chemistry, 1966. **6**: p. 347-429.

[2] R.H. Wiley, ed., *Chemistry of Heterocyclic Compounds, Vol. XXII: Pyrazoles, Pyrazolines, Pyrazolidines, Indazoles, and Condensed Rings*. 1967.

[3] M.P. Sammes and A.R. Katritzky, *The 3H-Pyrazoles.* Advances in Heterocyclic Chemistry, 1983. **34**: p. 1-52.

[4] G.W. Adams, J.H. Bowie, and R.N. Hayes, *Negative-Ion Fragmentations of Deprotonated Heterocycles - the Pyrazole and Imidazole Ring-Systems.* Rapid Communications in Mass Spectrometry, 1992. **6**(1): p. 54-57.

[5] V.M. Bierbaum, C.H. DePuy, and R.H. Shapiro, *Gas-Phase Reactions of Anions with Nitrous-Oxide and Carbon-Dioxide.* Journal of the American Chemical Society, 1977. **99**(17): p. 5800-5802.

[6] S.R. Kass, J. Filley, J.M. VanDoren, and C.H. DePuy, *Nitrous-Oxide in Gas-Phase Ion Molecule Chemistry - a Versatile Reagent for the Determination of Carbanion Structure.* Journal of the American Chemical Society, 1986. **108**(11): p. 2849-2852.

[7] C.H. DePuy, J.M. Van Doren, S. Gronert, S.R. Kass, E.L. Motell, G.B. Ellison, and V.M. Bierbaum, *Gas-phase negative-ion chemistry of diazomethane.* Journal of Organic Chemistry, 1989. **54**(8): p. 1846-50.

[8] R.A.J. OHair, S. Gronert, and C.H. DePuy, *New insights into the gas-phase anion chemistry of nitrous oxide.* European Mass Spectrometry, 1995. **1**(5): p. 429-436.

[9] C.D. Hurd and S.C. Lui, *Vinyldiazomethane.* Journal of the American Chemical Society, 1935. **57**: p. 2656-2657.

[10] A. Ledwith and D. Parry, *1,3-Dipolar cycloaddition reactions of diazo alkanes. II. Kinetics of the thermal and photochemical formation of pyrazole from diazopropene.* Journal of the Chemical Society B: Physical Organic, 1967(1): p. 41-42.

[11] H. Hart and J.L. Brewbaker, *1,3-Bisdiazopropane. Preparation and cyclization to pyrazole.* Journal of the American Chemical Society, 1969. **91**(3): p. 706-711.

[12] J.L. Brewbaker and H. Hart, *Cyclization of 3-diazoalkenes to pyrazoles.* Journal of the American Chemical Society, 1969. **91**(3): p. 711-715.

8 2-Oxepinoxide, $C_6H_5O_2^-$

8.1 Introduction

This chapter describes experiments performed measuring the photoelectron spectrum of 2-oxepinoxide, $C_6H_5O_2^-$ in order to establish the EA of the corresponding neutral, the 2-oxepinoxy radical. The 2-oxepinoxy radical is believed to be an intermediate formed during the combustion of benzene, as originally proposed by Carpenter.[1] Theoretical investigations on the oxidation of the phenyl radical[2] and unimolecular decomposition of the phenylperoxy radical[3] followed, both which include the 2-oxepinoxy radical as an intermediate to the formation of cyclopentadienyl radical and CO_2. These studies and another theoretical report on the unimolecular decomposition of the 2-oxepinoxy radical[4] suggest that the 2-oxepinoxy radical should be a stable intermediate formed during benzene combustion at intermediate temperatures.

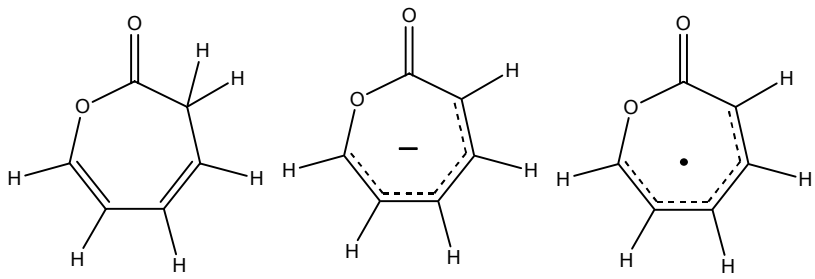

Recently, the gas phase acidity of 2(3H)-oxepinone was determined[5] as the first step in a series of three experiments designed to establish the heat of formation of 2-oxepinoxy radical. Determination of the EA of the 2-oxepinoxyl radical, reported here, is the second step. Combination of the 2(3H)-oxepinone gas phase acidity with the 2-oxepinoxyl radical EA in a thermodynamic cycle (as described in Chapter 2) will yield information about a C-H

bond dissociation energy of 2(3H)-oxepinone. The third experiment in the series is the calorimetric measurement of the heat of formation of 2(3H)-oxepinone. Combination of this heat of formation with the bond dissociation energy of 2(3H)-oxepinone will yield the heat of formation of the 2-oxepinoxy radical.

8.2 Experiment

2(3H)-Oxepinone was obtained from Carpenter and coworkers, prepared as described previously,[5] and was introduced into the flow tube by flowing a stream of helium over the liquid sample. Hydroxide ions, created using the microwave discharge ion source as described in Chapter 2, were used to deprotonate 2(3H)-oxepinone yielding the desired 2-oxepinoxide anion as well as an unknown ion of m/z = 65. Stable ion beams of ~100 pA of 2-oxepinoxide were produced using this method. In some experiments, liquid nitrogen was used to cool the flow tube, aiding in the cooling of the ions. In these experiments, slightly less intense ion beams were formed (~50 pA). In all experiments, the laser wavelength used for photodetachment was 351.1 nm and calibration of the absolute energy scale was accomplished via measurement of the EA of oxygen.

8.3 Results

Figure 8.1 shows the room temperature 351 nm photoelectron spectra of 2-oxepinoxide anion with the laser polarization at the magic angle (black), 0° (blue), and 90° (red) to the photoelectron collection axis. The spectrum consists of a broad photoelectron band with several sharper features which show no indication of a pattern. The angular measurements result in an anisotropy parameter, β, of –0.18 ± 0.07 at the peak of the broad detachment signal at 2.254 ± 0.010 eV.

DFT calculations were performed on the 2-oxepinoxide anion and 2-oxepinoxyl radical to assist in the assignment of the photoelectron spectra, as previously outlined in

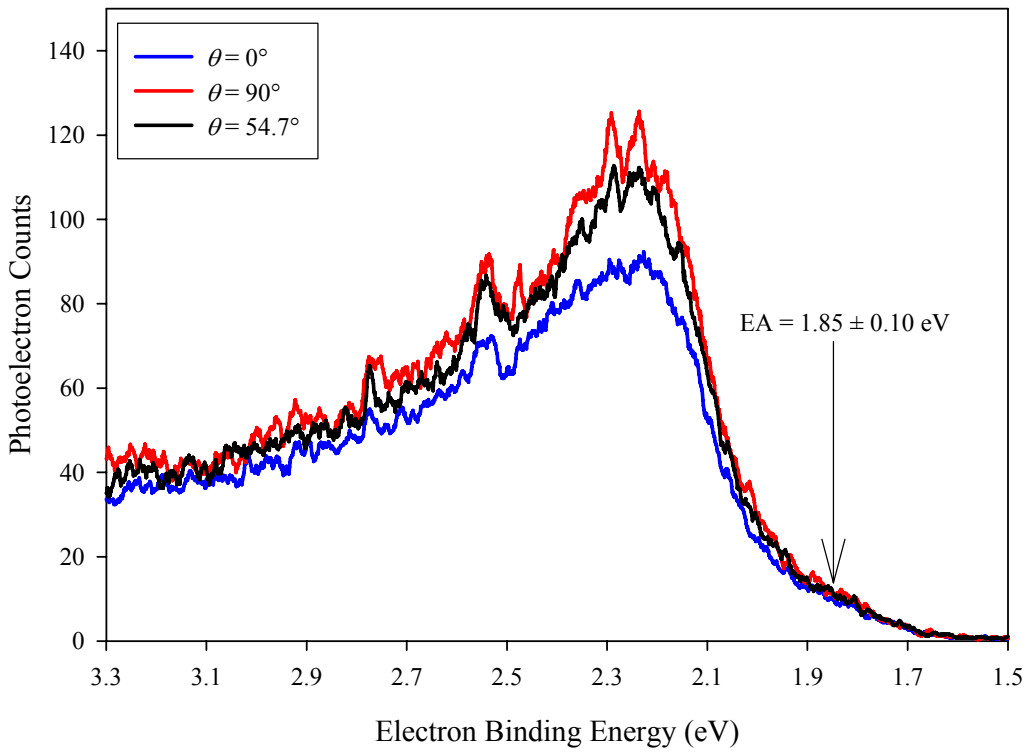

Figure 8.1 351.1 nm photoelectron spectrum of 2-oxepinoxide at 300 K taken at the magic angle (54.7°, black), parallel (0°, blue) and perpendicular (90°, red) to the photoelectron collection axis.

Chapter 2. The B3LYP method was used with the 6-31+G(d) basis set. Optimized geometries and harmonic vibrational frequencies were obtained for the ground states of the anion and neutral and are listed in Tables 8.2 and 8.3. For the 2-oxepinoxide anion, a minimum with non-planar structure (C_1 symmetry) was obtained. For 2-oxepinoxyl radical, a minimum with planar structure (C_s symmetry) was obtained. These calculations predict an EA of ~1.76 eV, close to the region of the experimental spectrum where the photodetachment signals begin.

With the anion having C_1 symmetry and the neutral having C_s symmetry, all 33 vibrational modes are allowed in the photoelectron spectrum. Large normal mode displacements are expected for the out-of-plane bending vibrations of the neutral, which should result in an extended vibrational progression for these modes. Franck-Condon simulations using the optimized geometries and frequencies were attempted, but, due to the large number of allowed and active vibrational modes (all 33 modes were found to be active), meaningful results have not been obtained.

For the Franck-Condon simulations described in previous chapters, a "cutoff" value of 0.001% of the origin intensity was used. This means that transitions whose intensities were less than 0.001% of the origin were omitted from the simulation. At this cutoff level, the 0 K Franck-Condon simulation of 2-oxepinoxide photodetachment is outside of our processing capabilities. Larger cutoff values were used successfully, however. Figure 8.2 shows the 0 K Franck-Condon simulation of 2-oxepinoxide detachment with cutoff values of 100%, 10%, and 1% of the origin intensity. In all of these simulations, the origin was given an intensity of 100 counts and a position matching the DFT computed EA (1.7567 eV). From the simulations, a clear trend is visible, with the rightmost portion of a particular simulation being a good approximation to a simulation with a smaller cutoff value. Simulations with even smaller cutoff values (0.1% and 0.01%) also show that this trend continues.

2-Oxepinoxide Anion

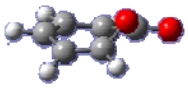

	Coordinates		
	X	Y	Z
C1	-0.4781	-1.4879	0.1423
C2	1.2816	0.1290	-0.0017
C3	0.4982	1.2974	0.1631
C4	-0.8864	1.4688	-0.0920
C5	-1.6714	-0.8540	0.2329
C6	-1.8983	0.5253	-0.1191
O7	2.4944	-0.0069	0.1861
O8	0.6015	-1.0107	-0.5814
H9	-0.3080	-2.4750	0.5772
H10	1.0827	2.1851	0.3978
H11	-1.2043	2.5097	-0.2142
H12	-2.4856	-1.4144	0.7016
H13	-2.9254	0.8641	-0.2534

2-Oxepinoxyl Radical

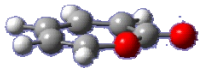

	Coordinates		
	X	Y	Z
C1	-0.7059	-1.5087	0.0000
C2	1.3026	0.0000	0.0000
C3	0.6116	1.2847	0.0000
C4	-0.7354	1.5911	0.0000
C5	-1.7956	-0.6875	0.0000
C6	-1.8434	0.7292	0.0000
O7	2.5086	-0.0924	0.0000
O8	0.6223	-1.2322	0.0000
H9	-0.8346	-2.5859	0.0000
H10	1.3234	2.1037	0.0000
H11	-0.9649	2.6554	0.0000
H12	-2.7454	-1.2168	0.0000
H13	-2.8284	1.1871	0.0000

Table 8.1 2-Oxepinoxide anion and 2-oxepinoxyl radical geometries in Cartesian coordinates obtained from the B3LYP/6-31+G(d) calculations.

Mode	2-Oxepinoxide Frequency (cm^{-1})
ν_1	3160
ν_2	3142
ν_3	3126
ν_4	3091
ν_5	3074
ν_6	1692
ν_7	1648
ν_8	1571
ν_9	1506
ν_{10}	1415
ν_{11}	1401
ν_{12}	1267
ν_{13}	1239
ν_{14}	1199
ν_{15}	1053
ν_{16}	1031
ν_{17}	954
ν_{18}	930
ν_{19}	907
ν_{20}	865
ν_{21}	825
ν_{22}	746
ν_{23}	724
ν_{24}	702
ν_{25}	682
ν_{26}	653
ν_{27}	577
ν_{28}	508
ν_{29}	420
ν_{30}	478
ν_{31}	346
ν_{32}	191
ν_{33}	115

Mode	Symmetry	2-Oxepinoxyl Frequency (cm^{-1})
ν_1	a'	3228
ν_2	a'	3220
ν_3	a'	3205
ν_4	a'	3185
ν_5	a'	3170
ν_6	a'	1786
ν_7	a'	1617
ν_8	a'	1558
ν_9	a'	1480
ν_{10}	a'	1453
ν_{11}	a'	1418
ν_{12}	a'	1345
ν_{13}	a'	1268
ν_{14}	a'	1215
ν_{15}	a'	1094
ν_{16}	a'	1049
ν_{17}	a'	951
ν_{18}	a'	892
ν_{19}	a'	801
ν_{20}	a'	696
ν_{21}	a'	509
ν_{22}	a'	421
ν_{23}	a'	359
ν_{24}	a"	992
ν_{25}	a"	941
ν_{26}	a"	851
ν_{27}	a"	795
ν_{28}	a"	739
ν_{29}	a"	640
ν_{30}	a"	536
ν_{31}	a"	376
ν_{32}	a"	133
ν_{33}	a"	73

Table 8.2 2-Oxepinoxide anion and 2-oxepinoxyl radical fundamental vibrational frequencies obtained from B3LYP/6-31+G(d) calculations.

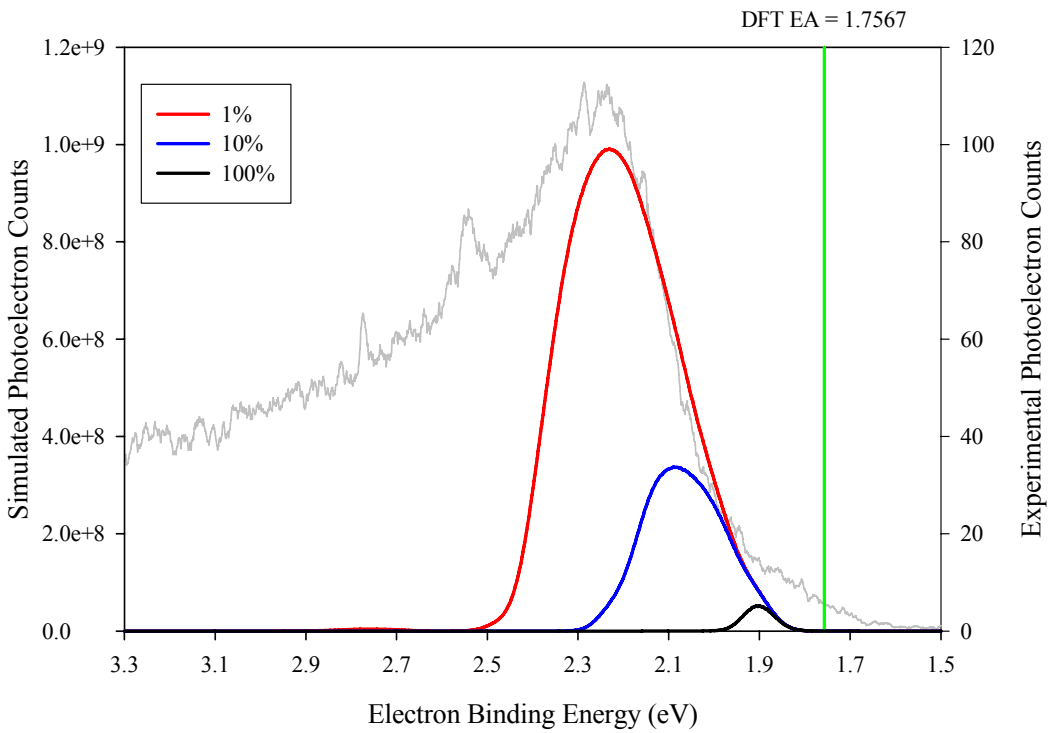

Figure 8.2 Franck-Condon simulation of 2-oxepinoxide 351.1 nm photodetachment at 0 K with a cutoff level of 100% (black), 10% (blue), and 1% (red) of the origin intensity. The position of the origin is indicated by the green line. The experimental spectrum is overlaid in grey.

Figure 8.3 shows Franck-Condon simulations performed at 300 K to explore the effects of hot band transitions. Again, cutoff values of 100%, 10%, and 1% of the origin intensity were used, with an origin intensity and position identical to that used for the 0 K simulations. With a cutoff value of 100%, the simulation is identical to that at 0 K, indicating that all hot-band transitions have smaller Franck-Condon factors than that of the origin. The simulations with cutoff values of 10% and 1% clearly show how significantly the hot-band transitions affect the spectrum. Inclusion of these hot-band transitions increases the computation time dramatically, however.

8.4 Discussion

Unfortunately, as can be seen in Figures 8.2 and 8.3, there is no indication of convergence of the simulation with the cutoff level as small as 1%. Franck-Condon simulations at 0 K with cutoff levels of 0.1% and 0.01% also show no indication of convergence. Without a reasonable Franck-Condon simulation, another method is needed to allow for the determination of the EA of the 2-oxepinoxyl radical. By estimating the difference between the DFT computed vertical detachment energy (VDE) and EA and applying that difference to the experimental VDE, an approximate experimental EA may be determined.

At the B3LYP/6-31+G(d) level, the computed EA is 1.7567 eV and the VDE is 2.0792 eV; the difference between these two values is 0.3225 eV. Figure 8.4 shows hypothetical potential energy curves for the 2-oxepinoxide system illustrating these energy differences. Applying this difference to the experimentally observed VDE of 2.254 ± 0.010 eV results in an EA of approximately 1.931 eV, near the region of the spectrum where the detachment signals start. This estimation is somewhat consistent with the 300 K Franck-Condon simulations where the EA is slightly higher in energy than the start of the photoelectron signals. To better estimate the difference between the VDE and EA,

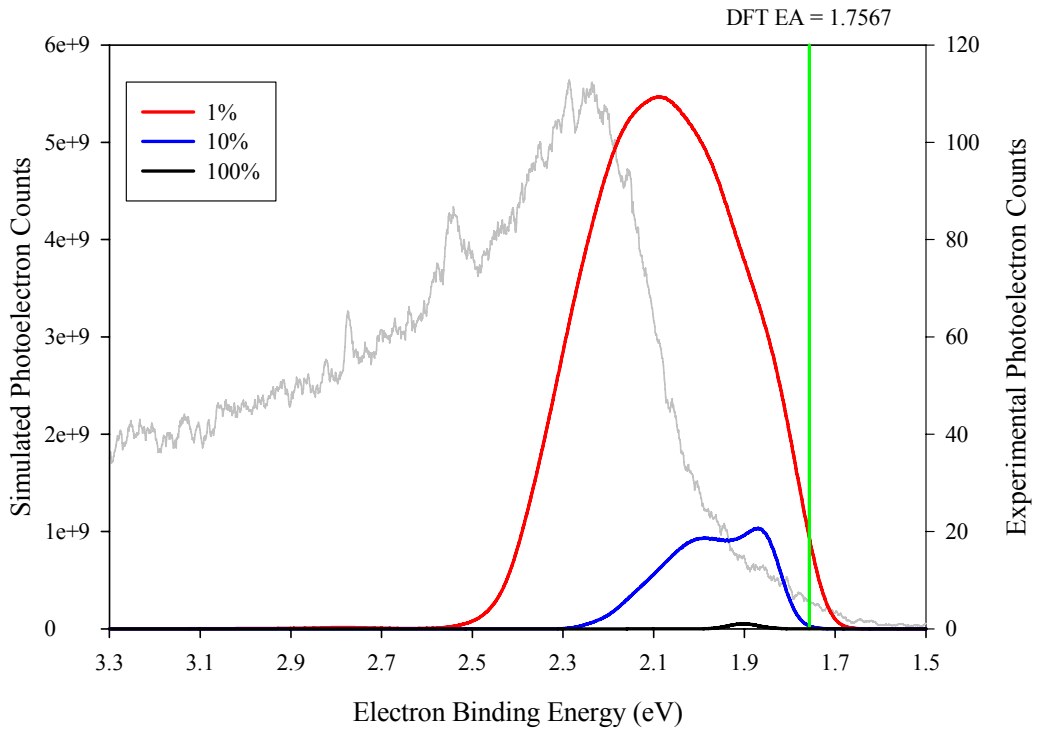

Figure 8.3 Franck-Condon simulation of 2-oxepinoxide 351.1 nm photodetachment at 300 K with a cutoff level of 100% (black), 10% (blue), and 1% (red) of the origin intensity. The position of the origin is indicated by the green line. The experimental spectrum is overlaid in grey.

calculations with the larger 6-311++G(d,p) basis set were performed, yielding an EA of 1.8166 eV and VDE of 2.1353 eV, for a difference of 0.3187 eV. Applying this difference to the experimental VDE yields an EA of 1.935 eV. With the aug-cc-pVTZ, the EA computed in this way is 1.918 eV.

As shown in the earlier chapters in this dissertation, DFT often predicts radical EAs extremely well. Table 8.3 summarizes the experimental and DFT electron affinities. With an average absolute error of 0.017 eV, B3LYP with the 6-311++G(d,p) basis set is expected to predict the EA of 2-oxypinoxy quite accurately. Considering this and the above discussion of the VDE and EA differences, we assign the EA of the 2-oxepinoxyl radical as 1.85 ± 0.10 eV.

With the EA of the 2-oxepinoxyl radical, it is possible to obtain the bond dissociation energy of 2(3H)-oxepinone using the methods outlined in Chapter 2. From the literature,[5] the 298 K deprotonation enthalpy of 2(3H)-oxepinone is 352 ± 2 kcal mol^{-1}. Using thermal corrections from the DFT calculations, $\Delta_{acid}H_0$ = 350 ± 2 kcal mol^{-1}. Combining this with the EA from above yields a bond dissociation energy of D_0 = 80 ± 3 kcal mol^{-1}. This value is close to the B3LYP/6-311++G(d,p) computed D_0 of 74 kcal mol^{-1}.

Several sharp features extend beyond the broad congested photodetachment signal which have a slightly different anisotropy. Since the deprotonation enthalpy[5] of 2(3H)-oxepinone is 352 ± 2 kcal mol^{-1} and that[6] of H_2O is 390.27 ± 0.03 kcal mol^{-1}, the reaction of 2(3H)-oxepinone with hydroxide is exothermic by ~38 kcal mol^{-1}. Such a large exothermicity could fragment the ring structure, and such an isomer of 2-oxepinoxide may be the signal carrier for these sharp features. Experiments using F^- as the deprotonation agent of 2(3H)-oxepinone are currently underway to help determine if these features originate from such an ion. Observation[5] of an ion with m/z 65 formed in the reaction of 2(3H)-oxepinone with hydroxide indicates that the ring structure may not stay intact. Unimolecular decomposition of 2-oxepinoxide could form CO_2 and a mass 65 ion with molecular formula

$C_5H_5^-$. Photoelectron experiments on this ion indicate the structure is not that of cyclopentadienide but most likely an open chain isomer.

8.5 Conclusion

The photoelectron spectrum of 2-oxepinoxide anion reveals that there is a large geometry change upon photodetachment, indicated by a broad congested spectrum with no discernable structure with a VDE of 2.254 ± 0.010. Franck-Condon simulations based on DFT computed geometries and frequencies also show that a broad spectrum is expected. The Franck-Condon simulations fail to reproduce the experimental spectrum within a reasonable amount of time to allow for precise determination of the EA of 2-oxepinoxyl. In spite of this difficulty, the EA of 2-oxepinoxyl radical is assigned as 1.85 ± 0.10 eV from the estimation of the difference between the EA and VDE. This combines with a previously reported gas phase acidity of 2(3H)-oxepinone to establish the bond dissociation energy of 2(3H)-oxepinone to be 80 ± 3 kcal mol^{-1}.

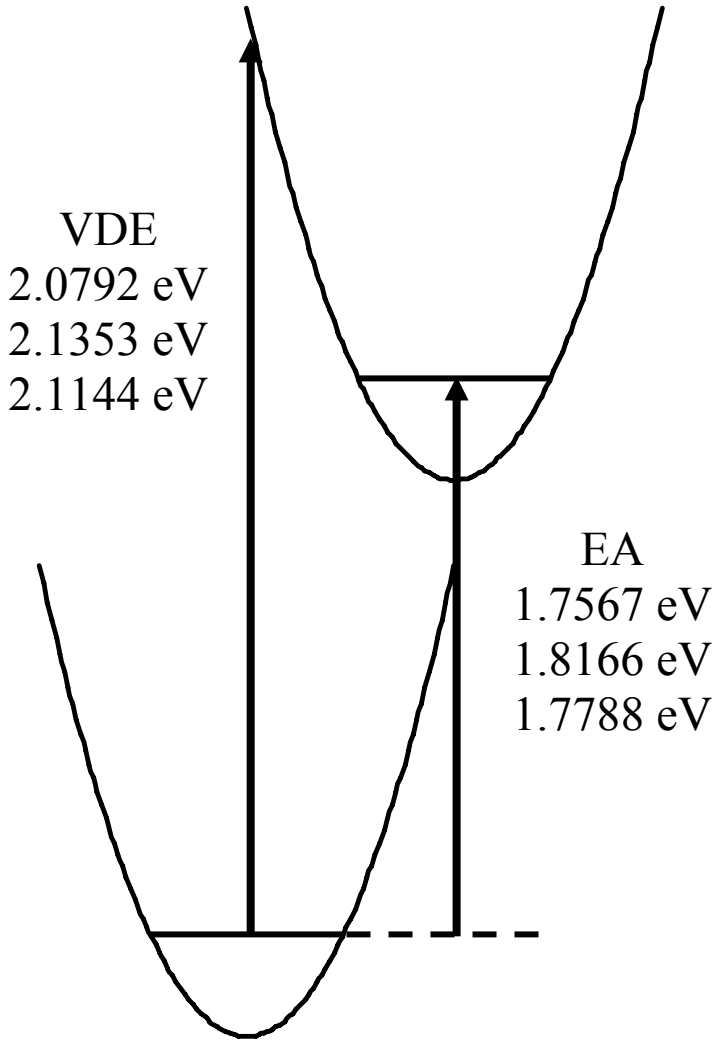

Figure 8.4 Potential energy curves illustrating the B3LYP computed vertical detachment energy (VDE) and electron affinity (EA). The top values were computed using the 6-31+G(d) basis set, the middle values using the 6-311++G(d,p) basis set and the bottom values using the aug-cc-pVTZ basis set.

Radical	Experimental EA (eV)	Basis Set	B3LYP EA (eV)	$EA_{exp} - EA_{B3LYP}$ (eV)
Cyclopentadienyl	1.812 ± 0.005	6-311++G(d,p)	1.763	0.049
Pyrrolyl	2.145 ± 0.010	6-311++G(d,p)	2.116	0.029
1-Imidazolyl	2.613 ± 0.006	6-311++G(d,p)	2.592	0.021
5-Imidazolyl	1.992 ± 0.010	6-311++G(d,p)	1.986	0.006
1-Pyrazolyl	2.935 ± 0.005	6-311++G(d,p)	2.945	-0.010
5-Pyrazolyl	2.104 ± 0.005	6-311++G(d,p)	2.109	-0.005
E-Vinyldiazomethyl	1.867 ± 0.007	6-311++G(d,p)	1.869	-0.002
2-Oxepinoxyl	—	6-31+G(d)	1.757	—
2-Oxepinoxyl	—	6-311++G(d,p)	1.817	—
2-Oxepinoxyl	—	aug-cc-pVTZ	1.779	—

Table 8.3 Experimental and B3LYP computed electron affinities.

Chapter 8 References

[1] B.K. Carpenter, *Computational Prediction of New Mechanisms for the Reactions of Vinyl and Phenyl Radicals with Molecular-Oxygen.* Journal of the American Chemical Society, 1993. **115**(21): p. 9806-9807.

[2] C. Barckholtz, M.J. Fadden, and C.M. Hadad, *Computational study of the mechanisms for the reaction of $O_2(^3\Sigma_g)$ with aromatic radicals.* Journal of Physical Chemistry A, 1999. **103**(40): p. 8108-8117.

[3] M.J. Fadden, C. Barckholtz, and C.M. Hadad, *Computational study of the unimolecular decomposition pathways of phenylperoxy radical.* Journal of Physical Chemistry A, 2000. **104**(13): p. 3004-3011.

[4] M.J. Fadden and C.M. Hadad, *Unimolecular decomposition of the 2-oxepinoxy radical: A key seven-membered ring intermediate in the thermal oxidation of benzene.* Journal of Physical Chemistry A, 2000. **104**(34): p. 8121-8130.

[5] S.M. Kroner, M.P. DeMatteo, C.M. Hadad, and B.K. Carpenter, *The gas-phase acidity of 2(3H)-oxepinone: A step toward an experimental heat of formation for the 2-oxepinoxy radical.* Journal of the American Chemical Society, 2005. **127**(20): p. 7466-7473.

[6] K.M. Ervin and V.F. DeTuro, *Anchoring the gas-phase acidity scale.* Journal of Physical Chemistry A, 2002. **106**(42): p. 9947-9956.

9 Summary and Conclusions

9.1 Introduction

There has recently been interest in homonuclear polynitrogen compounds as high energy density materials.[1-3] One polynitrogen species, N_5^-, was experimentally detected through collision induced dissociation electrospray ionization mass spectrometry[4] and laser desorption ionization time-of-flight mass spectrometry[5] of substituted *p*-phenylpentazoles. Theoretical studies suggest that N_5^- is a stable 5-membered ring compound, pentazolide.[6-9] Its decomposition into azide anion (N_3^-) and N_2 is predicted to be exothermic by 14-16 kcal mol^{-1}, and the heat of formation of pentazolide is predicted[9] to be $\Delta_f H_{298}$ = 62.1 ± 3.6 kcal mol^{-1}. Determination of these thermodynamic values through experiments is challenging, considering the difficulty in synthesis of pentazolide. Unequivocal synthesis or observation of pentazole (N_5H) has not yet been reported.[10]

The pentazolide anion is isoelectronic with the other 5-membered ring anions described earlier in this dissertation (cyclopentadienide, pyrrolide, imidazolide, and pyrazolide). By examining the systematic substitution of N atoms into the 5-membered ring, it may be possible to predict some of the properties of pentazole/pentazolide/pentazolyl radical through extrapolation of the experimental values described in previous chapters.

This chapter summarizes the previous chapters and makes the extrapolations discussed above based on similarities and trends observed in the experimental data. Since most of the compounds discussed in this dissertation are isoelectronic (with the exception $C_6H_5O_2^-$, discussed in Chapter 8), it is expected that these trends may provide useful predictions for the properties of other isoelectronic species yet unobserved (such as the triazole and tetrazole systems) in addition to N_5^-. Insights into potential experimental or

theoretical difficulties which may arise in the collection and interpretation of these data are also discussed.

9.2 Electron Affinities

Electron affinities of the 5-membered ring radicals cyclopentadienyl, pyrrolyl, 1-imidazolyl and 1-pyrazolyl were determined using negative ion photoelectron spectroscopy. Their values are 1.812 ± 0.005, 2.145 ± 0.010, 2.613 ± 0.006, and 2.938 ± 0.005 eV, respectively. Figure 9.1 displays the electron affinity of these radicals as a function of the number of nitrogen atoms in the ring. Also displayed are B3LYP/6-311++G(d,p) computed electron affinities for 1,2,3-triazolyl, 1,2,4-triazolyl, and tetrazolyl. As a first approximation, these data are used in a linear regression to predict an EA for the pentazolyl radical of ~4.6 eV. Vertical detachment energies of 5.7 and 5.6 eV have been previously predicted for pentazolide.[9, 11]

DFT predicts the EAs of the 1,2,3- and 1,2,4- triazolyl radicals to be 3.39 and 3.48 eV, respectively. The EA of tetrazolyl is predicted to be 4.16 eV. Notice that these energies are close to or greater than the photon energy used in these experiments of 3.408 or 3.531 eV. It is expected that experiments on these systems will require a higher energy photon to allow for determination of the EA of these radicals.

Electron affinities of other species were also determined, including isomers of 1-imidazolyl and 1-pyrazolyl. The EAs of these carbon centered radicals, 5-imidazolyl and 5-pyrazolyl are 1.992 ± 0.010 and 2.104 ± 0.005 eV, respectively. The EA of vinyldiazomethyl radical, a ring opened isomer of these isoelectronic species, was also found to be 1.867 ± 0.007 eV.

The EA of the 2-oxepinoxy radical was not precisely established in this dissertation. A large geometry change upon photodetachment of the 2-oxepinoxide anion strongly activates all vibrational modes of the radical in the photoelectron spectrum, resulting in a

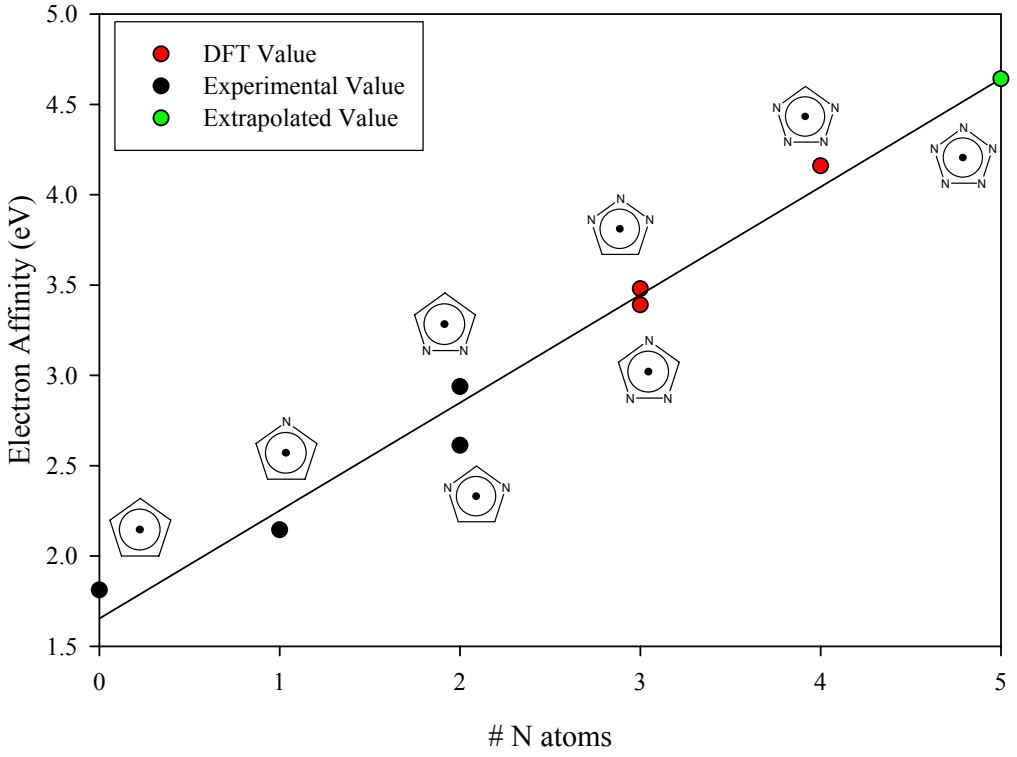

Figure 9.1 EAs of the 5-membered ring radicals with the corresponding number of nitrogen atoms in the 5-membered ring. The black points are experimental values and the red points are DFT calculated EAs. The solid line is a linear regression fit of the data to a line, and the green point is the EA predicted for pentazolyl radical from the extrapolation.

highly congested spectrum with little indication of the position of the band origin. Despite difficulties in simulating the spectrum, an EA of 1.85 ± 0.10 eV was assigned. DFT calculations predict an EA for the 2-oxepinoxyl radical of 1.82 eV at the B3LYP/6-311++G(d,p) level.

9.2 Bond Dissociation Energies and Heats of Formation

Bond dissociation energies were established for several of the 5-membered ring parent compounds for breaking a C—H or N—H bond using a thermodynamic cycle combining the gas phase acidity of the parent compound with the EA of the radical. Figure 9.2 displays the N—H bond dissociation energy as a function of the number of nitrogen atoms in the ring. The N—H bond dissociation energies of pyrrole, imidazole, and pyrazole are 93.92 ± 0.11,[12] 95.1 ± 0.5 and 106.4 ± 0.4 kcal mol^{-1}. N—H bond dissociation energies for 1,2,3-triazole, 1,2,4-triazole, and tetrazole were computed at the B3LYP/6-311++G(d,p) level and are also shown in Figure 9.2. A linear regression of the data suggests the N—H bond dissociation energy of hydrogen pentazole (N_5H) is ~114 kcal mol^{-1}.

For two of these heterocyclic compounds, imidazole and pyrazole, C—H bond dissociation energies were determined by combining the EAs of the corresponding radicals with the C—H gas phase acidity determined via bracketing observed in the photoelectron spectrometer. The carbon-5 proton on both imidazole and pyrazole is acidic enough to be deprotonated by HO^- but not acidic enough for deprotonation by O^-, resulting in identical gas phase acidities of $\Delta_{acid}G_{298}$ = 380 ± 4 kcal mol^{-1}. The EAs and gas phase acidities combine to give C5—H bond dissociation energies of 119 ± 4 and 121 ± 4 kcal mol^{-1} for imidazole and pyrazole, respectively. The C—H bond dissociation energies of cyclopentadiene and 2(3H)-oxepinone, also determined using a thermodynamic cycle, are 80.6 ± 2.3 and 81 ± 3 kcal mol^{-1}, respectively.

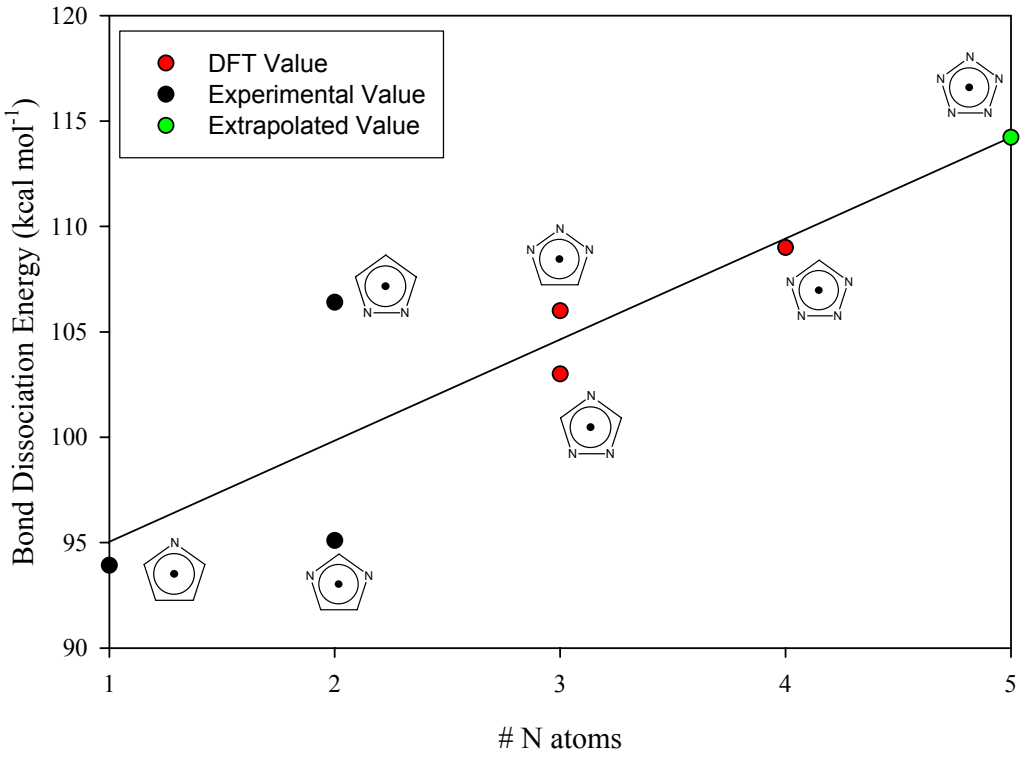

Figure 9.2 N—H bond dissociation energies of the 5-membered heterocyclic compounds as a function of the number of nitrogen atoms in the 5-membered ring. The black points are the experimental data, and the red points are DFT computed values. The solid line is a linear regression fit of the data to a line, and the green point is the N—H bond dissociation energy predicted for hydrogen pentazole from the extrapolation.

Comparison of the bond dissociation energies determined here can reveal the relative stability of the different radical species. Cyclopentadiene, with the smallest C—H or N—H bond dissociation energy, is expected to have the most stable radical formed upon breaking this bond. This radical will be followed in stability by the pyrrolyl radical, the 1-imidazolyl radical and the 1-pyrazolyl radical. The carbon radicals 5-imidazolyl and 5-pyrazolyl are likely to follow this.

Comparing the heats of formation of these radicals can verify this simple argument. From the bond dissociation energies and the heats of formation of the parent compounds,[13] the radical heats of formation can be determined. The 298 K heat of formation of the cyclopentadienyl radical is 64.6 ± 2.7 kcal mol^{-1}. The 298 K heat of formation of the pyrrolyl radical[12] is 69.15 ± 0.35 kcal mol^{-1}. The 298 K heats of formation of 1-imidazolyl and 1-pyrazolyl are 76.2 ± 0.6 and 98.7 ± 0.5 kcal mol^{-1}, respectively. The 298 K heats of formation of the carbon radicals 5-imidazolyl and 5-pyrazolyl are 100 ± 4 and 113 ± 4 kcal mol^{-1}, respectively. Figure 9.3 summarizes these values.

9.3 Electronic and Vibrational Structure

Aside from the thermodynamic parameters discussed above, electronic and vibrational structure of the neutral species can be extracted from the anion photoelectron spectra. The photoelectron spectrum of the high-symmetry $^1A_1'$ cyclopentadienide anion reflects the presence of Jahn-Teller interactions in the doubly degenerate $^2E_1''$ cyclopentadienyl radical. The spectrum is dominated by an intense origin band, but vibrational bands corresponding to the Jahn-Teller active vibrations are clearly observed. Additionally, unexpected vibrational bands appear in the spectrum, and are assigned to non-totally symmetric modes which gain intensity due to strong off-diagonal coupling. Since the pentazolide and cyclopentadienide systems are isoelectronic and of the same symmetry (D_{5h}), it is expected that, if bound, pentazolyl will exhibit similar electronic and vibrational structure

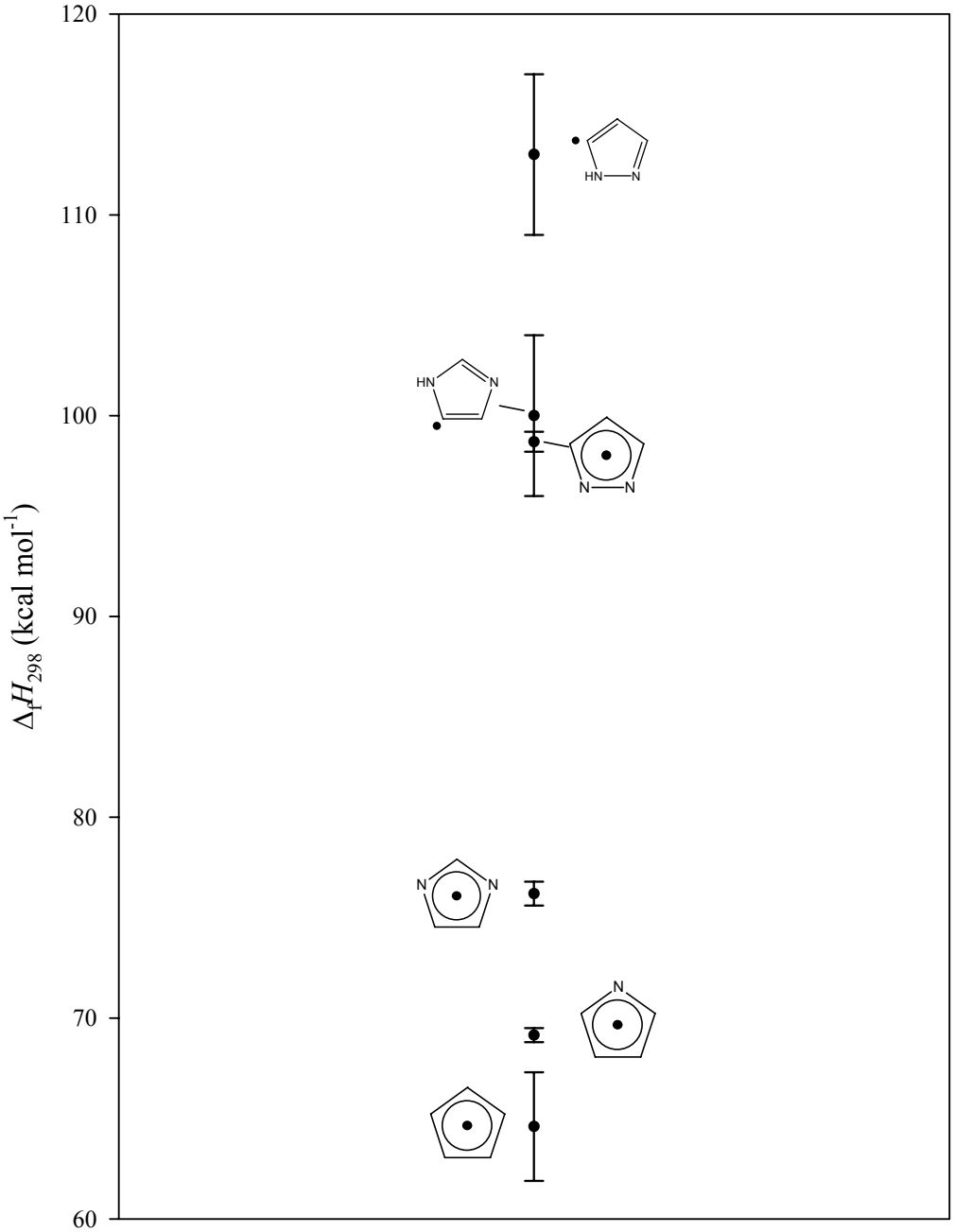

Figure 9.3 298 K heats of formation of 5-membered ring radicals.

as the cyclopentadienyl radical, with a spectrum dominated by the band origin and Jahn-Teller active vibrations.

With the maximum symmetry lowered from D_{5h} to C_{2v}, Jahn-Teller interactions are not present in the pyrrolyl, 1-imidazolyl, and 1-pyrazolyl systems. Franck-Condon simulations do, however, show that these systems are not free from non-adiabatic effects, and the spectra show interesting effects attributed to vibronic coupling between low lying electronic states. In pyrrolyl, the ground state features are well resolved but the vibronic coupling effects cause the first excited state to appear broad and featureless. This is due to transformation of the expected potential energy minimum into a transition state.[14] In the 1-imidazolyl system, however, the vibronic coupling effects are minimal and the spectrum of the electronic ground state appears very Franck-Condon like. A small unexpected feature appears in the spectrum and is assigned to an overtone of an in-plane non-totally symmetric vibration, gaining intensity from a Fermi-Resonance which is affected by vibronic coupling.[15]

The photoelectron spectrum of 1-pyrazolide shows the ground and first excited states of 1-pyrazolyl to be very close in energy. Franck-Condon simulations on these states fail to reproduce the experimental spectra, with two peaks missing which are experimentally observed and the intensities of most other vibrational bands severely overestimated. The second electronic excited state further complicates the spectra and is transformed into a transition state by the vibronic coupling effects with the ground and first excited states. Simulations which take the nonadiabatic effects into consideration predict the spectrum very well, allowing for confident assignments of the vibrational features observed.[16, 17] It is expected that the photoelectron spectrum of the 1,2,3-triazolide, 1,2,4-triazolide, and tetrazolide anions may also have analogous vibronic coupling effects, which may cause difficulties in assignment of the spectra.

The photoelectron spectra of the isoelectronic 5-imidazolide and 5-pyrazolide are reproduced nearly perfectly by the Franck-Condon simulations. Several vibrational features

are observed in the spectra which correspond primarily to in-plane ring distortion or ring breathing vibrations of the corresponding neutral radicals. Franck-Condon simulations of the vinyldiazomethyl anion detachment show that the spectrum originates from the E-vinyldiazomethyl anion isomer, with little or no indication of Z-vinyldiazomethyl anion formation in the flow tube.

9.4 Future Work

Photoelectron spectra of one more 5-membered heterocyclic ion, 1,2,3-triazolide, are being obtained in another of Professor Lineberger's laboratories. Once finalized, the EA of the corresponding radical and the parent N—H bond dissociation energy can be added to the extrapolations performed here to lend additional support to the predicted properties of the pentazole system.

Experiments on N-methyl substituted imidazolide and pyrazolide are being performed on the photoelectron spectrometer used here to obtain the EA of the C5-methyl-imidazolyl and C5-methyl-pyrazolyl radicals. These measurements, coupled with corresponding measurements of the C5—H gas phase acidities will allow for a precise determination of the C5—H bond dissociation energies of these compounds.[18] Assuming the methyl substitution is only a small perturbation, this will provide a useful comparison to the C5—H bond dissociation energies obtained for imidazole and pyrazole; preliminary results indicate this to be the case.

Continuing the investigation of heterocyclic compounds, experiments are planned on the 6-membered rings which are isoelectronic with benzene (pyridine, pyrimidine, etc). These experiments will provide EAs, bond dissociation energies, and heats of formation for these systems, which at present are not well known. Additionally, all of the experiments which are planned or currently in progress will reveal vibrational structure of the unstable radical species formed from the photodetachment of the closed shell anions.

Chapter 9 References

[1] T.M. Klapotke, *Homopolyatomic nitrogen compounds.* Angewandte Chemie-International Edition, 1999. **38**(17): p. 2536-2538.

[2] A. Hammerl and T.M. Klapotke, *Tetrazolylpentazoles: Nitrogen-rich compounds.* Inorganic Chemistry, 2002. **41**(4): p. 906-912.

[3] V. Benin, P. Kaszynski, and J.G. Radziszewski, *Arylpentazoles revisited: Experimental and theoretical studies of 4-hydroxyphenylpentazole and 4-oxophenylpentazole anion.* Journal of Organic Chemistry, 2002. **67**(4): p. 1354-1358.

[4] A. Vij, J.G. Pavlovich, W.W. Wilson, V. Vij, and K.O. Christe, *Experimental detection of the pentaazacyclopentadienide (pentazolate) anion, cyclo-N_5^-.* Angewandte Chemie-International Edition, 2002. **41**(16): p. 3051-3054.

[5] H. Ostmark, S. Wallin, T. Brinck, P. Carlqvist, R. Claridge, E. Hedlund, and L. Yudina, *Detection of pentazolate anion (cyclo-N_5^-) from laser ionization and decomposition of solid p-dimethylaminophenylpentazole.* Chemical Physics Letters, 2003. **379**(5-6): p. 539-546.

[6] M.N. Glukhovtsev, H.J. Jiao, and P.V. Schleyer, *Besides N-2, what is the most stable molecule composed only of nitrogen atoms?* Inorganic Chemistry, 1996. **35**(24): p. 7124-7133.

[7] R.N. Butler, A. Fox, S. Collier, and L.A. Burke, *Pentazole chemistry: the mechanism of the reaction of aryldiazonium chlorides with azide ion at -80 degrees C: concerted versus stepwise formation of arylpentazoles, detection of a pentazene intermediate, a combined H-1 and N-15 NMR experimental and ab initio theoretical study.* Journal of the Chemical Society-Perkin Transactions 2, 1998(10): p. 2243-2247.

[8] L. Gagliardi, G. Orlandi, S. Evangelisti, and B.O. Roos, *A theoretical study of the nitrogen clusters formed from the ions N-3(-), N-5(+), and N-5(-).* Journal of Chemical Physics, 2001. **114**(24): p. 10733-10737.

[9] M.T. Nguyen and T.K. Ha, *Decomposition mechanism of the polynitrogen N_5 and N_6 clusters and their ions.* Chemical Physics Letters, 2001. **335**(3-4): p. 311-320.

[10] R.N. Butler, J.C. Stephens, and L.A. Burke, *First generation of pentazole (HN5, pentazolic acid), the final azole, and a zinc pentazolate salt in solution: A new N-dearylation of 1-(p-methoxyphenyl) pyrazoles, a 2-(p-methoxyphenyl) tetrazole and application of the methodology to 1-(p-methoxyphenyl) pentazole.* Chemical Communications, 2003(8): p. 1016-1017.

[11] S. Fau, K.J. Wilson, and R.J. Bartlett, *On the stability of $N_5^+N_5^-$.* Journal of Physical Chemistry A, 2002. **106**(18): p. 4639-4644.

[12] B. Cronin, M.G.D. Nix, R.H. Qadiri, and M.N.R. Ashfold, *High resolution photofragment translational spectroscopy studies of the near ultraviolet photolysis of pyrrole.* Physical Chemistry Chemical Physics, 2004. **6**(21): p. 5031-5041.

[13] J.E. Bartmess, *"Negative Ion Energetics Data"*, in *NIST Chemistry Webbook, NIST Standard Reference Database Number 69*, J.P. Linstrom and W.G. Mallard, Editors. June 2005, National Institue of Standards and Technology: Gaithersburg MD, 20899.

[14] A.J. Gianola, T. Ichino, R.L. Hoenigman, S. Kato, V.M. Bierbaum, and W.C. Lineberger, *Thermochemistry and electronic structure of the pyrrolyl radical.* Journal of Physical Chemistry A, 2004. **108**(46): p. 10326-10335.

[15] A.J. Gianola, T. Ichino, R.L. Hoenigman, S. Kato, V.M. Bierbaum, and W.C. Lineberger, *Photoelectron spectra and ion chemistry of imidazolide.* Journal of Physical Chemistry A, 2005. **109**(50): p. 11504-11514.

[16] A.J. Gianola, T. Ichino, S. Kato, V.M. Bierbaum, and W.C. Lineberger, *Thermochemical Studies of Pyrazolide.* Journal of Physical Chemistry A, 2006. 10.1021/jp057499+.

[17] T. Ichino, A.J. Gianola, W.C. Lineberger, and J.F. Stanton, *Nonadiabatic effects in the photoelectron spectrum of the pyrazolide anion: Three-state interactions of the pyrazolyl radical.* Submitted.

[18] S.M. Villano, A.J. Gianola, S. Kato, V.M. Bierbaum, and W.C. Lineberger, *Manuscript in preparation.*

Bibliography

G.W. Adams, J.H. Bowie, and R.N. Hayes, *Negative-Ion Fragmentations of Deprotonated Heterocycles - the Pyrazole and Imidazole Ring-Systems.* Rapid Communications in Mass Spectrometry, 1992. **6**(1): p. 54-57.

B.E. Applegate, A.J. Bezant, and T.A. Miller, *The Jahn-Teller and related effects in the cyclopentadienyl radical. II. Vibrational analysis of the A $^2A_2''$ - X $^2E_1''$ electronic transition.* Journal of Chemical Physics, 2001. **114**(11): p. 4869-4882.

B.E. Applegate, T.A. Miller, and T.A. Barckholtz, *The Jahn-Teller and related effects in the cyclopentadienyl radical. I. The ab initio calculation of spectroscopically observable parameters.* Journal of Chemical Physics, 2001. **114**(11): p. 4855-4868.

G.B. Bacskay, M. Martoprawiro, and J.C. Mackie, *An ab initio quantum chemical study of the electronic structure and stability of the pyrrolyl radical: Comparison with the isoelectronic cyclopentadienyl radical.* Chemical Physics Letters, 1998. **290**(4-6): p. 391-398.

C. Barckholtz, M.J. Fadden, and C.M. Hadad, *Computational study of the mechanisms for the reaction of $O_2(^3\Sigma_g)$ with aromatic radicals.* Journal of Physical Chemistry A, 1999. **103**(40): p. 8108-8117.

J.E. Bartmess, *"Negative Ion Energetics Data"*, in *NIST Chemistry Webbook, NIST Standard Reference Database Number 69*, J.P. Linstrom and W.G. Mallard, Editors. June 2005, National Institue of Standards and Technology: Gaithersburg MD, 20899.

M.J. Bearpark, M.A. Robb, and N. Yamamoto, *A CASSCF study of the cyclopentadienyl radical: conical intersections and the Jahn-Teller effect.* Spectrochimica Acta Part A - Molecular and Biomolecular Spectroscopy, 1999. **55**(3): p. 639-646.

A.D. Becke, *Density-Functional Thermochemistry .3. The Role of Exact Exchange.* Journal of Chemical Physics, 1993. **98**(7): p. 5648-5652.

V. Benin, P. Kaszynski, and J.G. Radziszewski, *Arylpentazoles revisited: Experimental and theoretical studies of 4-hydroxyphenylpentazole and 4-oxophenylpentazole anion.* Journal of Organic Chemistry, 2002. **67**(4): p. 1354-1358.

G. Bermudez and L. Pfefferle, *Laser Ionization Time-of-Flight Mass-Spectrometry Combined with Residual-Gas Analysis for the Investigation of Moderate Temperature Benzene Oxidation.* Combustion and Flame, 1995. **100**(1-2): p. 41-51.

P.F. Bernath, *Spectra of Atoms and Molecules*. 1995, New York: Oxford University Press.

V.M. Bierbaum, C.H. DePuy, and R.H. Shapiro, *Gas-Phase Reactions of Anions with Nitrous-Oxide and Carbon-Dioxide.* Journal of the American Chemical Society, 1977. **99**(17): p. 5800-5802.

Y.J. Bomble, K.W. Sattelmeyer, J.F. Stanton, and J. Gauss, *On the vertical excitation energy of cyclopentadiene.* Journal of Chemical Physics, 2004. **121**(11): p. 5236-5240.

W.T. Borden and E.R. Davidson, *Potential Surfaces for the Planar Cyclopentadienyl Radical and Cation.* Journal of the American Chemical Society, 1979. **101**(14): p. 3771-3775.

R. Botter, V.H. Dibeler, J.A. Walker, and H.M. Rosenstock, *Experimental and Theoretical Studies of Photoionization-Efficiency Curves for C_2H_2 and C_2D_2.* J. Chem. Phys., 1966. **44**: p. 1271-1278.

J.L. Brewbaker and H. Hart, *Cyclization of 3-diazoalkenes to pyrazoles.* Journal of the American Chemical Society, 1969. **91**(3): p. 711-715.

R.N. Butler, A. Fox, S. Collier, and L.A. Burke, *Pentazole chemistry: the mechanism of the reaction of aryldiazonium chlorides with azide ion at -80 degrees C: concerted versus stepwise formation of arylpentazoles, detection of a pentazene intermediate, a combined H-1 and N-15 NMR experimental and ab initio theoretical study.* Journal of the Chemical Society-Perkin Transactions 2, 1998(10): p. 2243-2247.

R.N. Butler, J.C. Stephens, and L.A. Burke, *First generation of pentazole (HN5, pentazolic acid), the final azole, and a zinc pentazolate salt in solution: A new N-dearylation of 1-(p-methoxyphenyl) pyrazoles, a 2-(p-methoxyphenyl) tetrazole and application of the methodology to 1-(p-methoxyphenyl) pentazole.* Chemical Communications, 2003(8): p. 1016-1017.

B.K. Carpenter, *Computational Prediction of New Mechanisms for the Reactions of Vinyl and Phenyl Radicals with Molecular-Oxygen.* Journal of the American Chemical Society, 1993. **115**(21): p. 9806-9807.

J. Catalan, R.M. Claramunt, J. Elguero, J. Laynez, M. Menendez, F. Anvia, J.H. Quian, M. Taagepera, and R.W. Taft, *Basicity and Acidity of Azoles - the Annelation Effect in Azoles.* Journal of the American Chemical Society, 1988. **110**(13): p. 4105-4111.

I.C. Chang, *Acousto-Optic Devices and Applications*, in *Handbook of Optics*, M. Bass, Editor. 1995, McGraw-Hill: New York. p. 12.1-12.54.

P. Chen, *Photoelectron Spectroscopy of Reactive Intermediates*, in *Unimolecular and Bimolecular Reaction Dynamics*, C.Y. Ng, T. Baer, and I. Powis, Editors. 1994, Wiley & Sons: New York. p. 371-425.

J. Cooper and R.N. Zare, *Angular distribution of photoelectrons.* Journal of Chemical Physics, 1968. **48**: p. 942-943.

B. Cronin, M.G.D. Nix, R.H. Qadiri, and M.N.R. Ashfold, *High resolution photofragment translational spectroscopy studies of the near ultraviolet photolysis of pyrrole.* Physical Chemistry Chemical Physics, 2004. **6**(21): p. 5031-5041.

A. D'Anna, A. D'Alessio, and J. Kent, *A computational study of hydrocarbon growth and the formation of aromatics in coflowing laminar diffusion flames of ethylene.* Combustion and Flame, 2001. **125**(3): p. 1196-1206.

C.H. DePuy, J.M. Van Doren, S. Gronert, S.R. Kass, E.L. Motell, G.B. Ellison, and V.M. Bierbaum, *Gas-phase negative-ion chemistry of diazomethane.* Journal of Organic Chemistry, 1989. **54**(8): p. 1846-50.

P.J. Derrick, L. Asbrink, O. Edqvist, and E. Lindholm, *Photoelectron-Spectroscopical Study of Vibrations of Furan, Thiophene, Pyrrole and Cyclopentadiene.* Spectrochimica Acta, Part A: Molecular Spectroscopy, 1971. **A 27**(12): p. 2525-2537.

J. Eiding, R. Schneider, W. Domcke, H. Koppel, and W. Vonniessen, *Abinitio Investigation of the Multimode Dynamic Jahn-Teller Effect in the $X\,^2E_{1g}$ State of the Benzene Cation.* Chemical Physics Letters, 1991. **177**(3): p. 345-351.

J.H.D. Eland, *Molecular Photoelectron-Spectroscopy.* Journal of Physics E-Scientific Instruments, 1978. **11**(10): p. 969-977.

P.C. Engelking and W.C. Lineberger, *Laser Photoelectron Spectrometry of $C_5H_5^-$ - Determination of Electron-Affinity and Jahn-Teller Coupling in Cyclopentadienyl.* Journal of Chemical Physics, 1977. **67**(4): p. 1412-1417.

P.C. Engelking, *Approximate Rotational Band Shifts.* Journal of Physical Chemistry, 1986. **90**(19): p. 4544-4545.

R. Engleman and D.A. Ramsay, *Electronic Absorption Spectrum of Cyclopentadienyl Radical (C_5H_5) and Its Deuterated Derivatives.* Canadian Journal of Physics, 1970. **48**(8): p. 964-969.

K.M. Ervin, J. Ho, and W.C. Lineberger, *A Study of the Singlet and Triplet-States of Vinylidene by Photoelectron-Spectroscopy of $H_2C{=}C^-$, $D_2C{=}C^-$, and $HDC{=}C^-$ - Vinylidene Acetylene Isomerization.* Journal of Chemical Physics, 1989. **91**(10): p. 5974-5992.

K.M. Ervin and W.C. Lineberger, *Photoelectron Spectroscopy of Negative Ions*, in *Advances in Gas Phase Ion Chemistry*, N.G. Adams and L.M. Babcock, Editors. 1992, JAI Press: Greenwich. p. 121-166.

K.M. Ervin, T.M. Ramond, G.E. Davico, R.L. Schwartz, S.M. Casey, and W.C. Lineberger, *Naphthyl radical: Negative ion photoelectron spectroscopy, Franck-Condon simulation, and thermochemistry.* Journal of Physical Chemistry A, 2001. **105**(48): p. 10822-10831.

K.M. Ervin and V.F. DeTuro, *Anchoring the gas-phase acidity scale.* Journal of Physical Chemistry A, 2002. **106**(42): p. 9947-9956.

K.M. Ervin, *FCFGAUS, Fortran program*. 2003, Reno: http://www.chem.unr.edu/~ervin/pes; University of Nevada, Reno.

K.M. Ervin, W. Anusiewicz, P. Skurski, J. Simons, and W.C. Lineberger, *The only stable state of O_2^- is the $X\,^2\Pi_g$ ground state and it (still!) has an adiabatic electron detachment energy of 0.45 eV.* Journal of Physical Chemistry A, 2003. **107**(41): p. 8521-8529.

K.M. Ervin, *PESCAL, Fortran program*. 2004, Reno: http://www.chem.unr.edu/~ervin/pes; University of Nevada, Reno.

M.J. Fadden, C. Barckholtz, and C.M. Hadad, *Computational study of the unimolecular decomposition pathways of phenylperoxy radical.* Journal of Physical Chemistry A, 2000. **104**(13): p. 3004-3011.

M.J. Fadden and C.M. Hadad, *Unimolecular decomposition of the 2-oxepinoxy radical: A key seven-membered ring intermediate in the thermal oxidation of benzene.* Journal of Physical Chemistry A, 2000. **104**(34): p. 8121-8130.

S. Fau, K.J. Wilson, and R.J. Bartlett, *On the stability of $N_5^+N_5^-$.* Journal of Physical Chemistry A, 2002. **106**(18): p. 4639-4644.

F.C. Fehsenfeld, K.M. Evenson, and H.P. Broida, *Microwave Discharge Cavities Operating at 2450 MHz.* Review of Scientific Instruments, 1965. **36**(3): p. 294-298.

C.S. Feigerle, *Ph.D. Thesis*. 1983, University of Colorado: Boulder, CO.

G. Fischer, *Vibronic Coupling*. 1984, London: Academic Press.

M.J. Frisch, G.W. Trucks, H.B. Schlegel, G.E. Scuseria, M.A. Robb, J.R. Cheeseman, J.A. Montgomery, Jr. , T. Vreven, K.N. Kudin, J.C. Burant, J.M. Millam, S.S. Iyengar, J. Tomasi, V. Barone, B. Mennucci, M. Cossi, G. Scalmani, N. Rega, G.A. Petersson, H. Nakatsuji, M. Hada, M. Ehara, K. Toyota, R. Fukuda, J. Hasegama, M. Ishida, T. Nakajima, Y. Honda, O. Kitao, H. Nakai, M. Klene, X. Li, J.E. Knox, H.P. Hratchian, J.B. Cross, C. Adamo, J. Jaramillo, R. Gomperts, R.E. Stratmann, O. Yazyev, A.J. Austin, R. Cammi, C. Pomelli, J.W. Ochterski, P.Y. Ayala, K. Morokuma, G.A. Voth, P. Salvador, J.J. Dannenberg, V.G. Zakrzewski, S. Dapprich, A.D. Daniels, M.C. Strain, O. Farkas, D.K. Malick, A.D. Rabuck, K. Raghavachari, J.B. Foresman, J.V. Ortiz, Q. Cui, A.G. Baboul, S. Clifford, J. Cioslowski, B.B. Stefanov, G. Liu, A. Liashenko, P. Piskorz, I. Komaromi, R.L. Martin, D.J. Fox, T. Keith, M.A. Al-Laham, C.Y. Peng, A. Nanayakkara, M. Challacombe, P.M.W. Gill, B. Johnson, W. Chen, M.W. Wong, C. Gonzalez, and J.A. Pople, *Gaussian 03, Revision B.05*. 2003, Gaussian, Inc.: Pittsburgh, PA.

L. Gagliardi, G. Orlandi, S. Evangelisti, and B.O. Roos, *A theoretical study of the nitrogen clusters formed from the ions N-3(-), N-5(+), and N-5(-).* Journal of Chemical Physics, 2001. **114**(24): p. 10733-10737.

A.J. Gianola, T. Ichino, R.L. Hoenigman, S. Kato, V.M. Bierbaum, and W.C. Lineberger, *Thermochemistry and electronic structure of the pyrrolyl radical.* Journal of Physical Chemistry A, 2004. **108**(46): p. 10326-10335.

A.J. Gianola, T. Ichino, R.L. Hoenigman, S. Kato, V.M. Bierbaum, and W.C. Lineberger, *Photoelectron spectra and ion chemistry of imidazolide.* Journal of Physical Chemistry A, 2005. **109**(50): p. 11504-11514.

A.J. Gianola, T. Ichino, S. Kato, V.M. Bierbaum, and W.C. Lineberger, *Thermochemical Studies of Pyrazolide.* Journal of Physical Chemistry A, 2006. 10.1021/jp057499+.

M.N. Glukhovtsev, H.J. Jiao, and P.V. Schleyer, *Besides N-2, what is the most stable molecule composed only of nitrogen atoms?* Inorganic Chemistry, 1996. **35**(24): p. 7124-7133.

R.F. Gunion, M.K. Gilles, M.L. Polak, and W.C. Lineberger, *Ultraviolet Photoelectron-Spectroscopy of the Phenide, Benzyl and Phenoxide Anions, with Abinitio Calculations.* International Journal of Mass Spectrometry and Ion Processes, 1992. **117**(1-3): p. 601-620.

J.L. Hall and M.W. Siegel, *Angular dependence of the laser photodetachment of the negative ions of carbon, oxygen, and hydrogen.* Journal of Chemical Physics, 1968. **48**: p. 943-945.

A. Hammerl and T.M. Klapotke, *Tetrazolylpentazoles: Nitrogen-rich compounds.* Inorganic Chemistry, 2002. **41**(4): p. 906-912.

D. Hanstorp and M. Gustafsson, *Determination of the Electron-Affinity of Iodine.* Journal of Physics B-Atomic Molecular and Optical Physics, 1992. **25**(8): p. 1773-1783.

D.C. Harris and M.D. Bertolucci, *Symmetry and Spectroscopy An Introduction to Vibrational and Electronic Spectroscopy*. 1978, New York, NY: Oxford University Press.

A.G. Harrison, L.R. Honnen, H.J. Dauben, Jr., and F.P. Lossing, *Free Radicals by Mass Spectrometry. XX. Ionization Potentials of Cyclopentadienyl and Cycloheptatrienyl Radicals.* Journal of the American Chemical Society, 1960. **82**(21): p. 5593-5598.

H. Hart and J.L. Brewbaker, *1,3-Bisdiazopropane. Preparation and cyclization to pyrazole.* Journal of the American Chemical Society, 1969. **91**(3): p. 706-711.

A. Hazra and M. Nooijen, *Comparison of various Franck-Condon and vibronic coupling approaches for simulating electronic spectra: The case of the lowest photoelectron band of ethylene.* Physical Chemistry Chemical Physics, 2005. **7**(8): p. 1759-1771.

G. Herzberg, *Molecular Specta and Molecular Structure. Vol. II. Infrared and Raman Spectra of Polyatomic Molecules*. 1950, New York: Van Nostrand.

W.D. Hobey and A.D. McLachlan, *Dynamical Jahn-Teller effect in hydrocarbon radicals.* Journal of Chemical Physics, 1960. **33**: p. 1695-1703.

D. Hodgson, H.Y. Zhang, M.R. Nimlos, and J.T. McKinnon, *Quantum chemical and RRKM investigation of the elementary channels of the reaction C_6H_6+O(^{3}P).* Journal of Physical Chemistry A, 2001. **105**(17): p. 4316-4327.

C.D. Hurd and S.C. Lui, *Vinyldiazomethane.* Journal of the American Chemical Society, 1935. **57**: p. 2656-2657.

T. Ichino, A.J. Gianola, W.C. Lineberger, and J.F. Stanton, *Manuscript in preparation.*

T. Ichino, A.J. Gianola, W.C. Lineberger, and J.F. Stanton, *Nonadiabatic effects in the photoelectron spectrum of the pyrazolide anion: Three-state interactions of the pyrazolyl radical.* Submitted.

H.A. Jahn and E. Teller, *Stability of polyatomic molecules in degenerate electronic states. I. Orbital degeneracy.* Proc. R. Soc. (London), 1937. **A161**: p. 220-235.

P. Jimenez, M.V. Roux, C. Turrion, and F. Gomis, *Thermochemical Properties of N-Heterocyclic Compounds .1. Enthalpies of Combustion, Vapor-Pressures and Enthalpies of Sublimation, and Enthalpies of Formation of Pyrazole, Imidazole, Indazole, and Benzimidazole.* Journal of Chemical Thermodynamics, 1987. **19**(9): p. 985-992.

S.R. Kass, J. Filley, J.M. VanDoren, and C.H. DePuy, *Nitrous-Oxide in Gas-Phase Ion Molecule Chemistry - a Versatile Reagent for the Determination of Carbanion Structure.* Journal of the American Chemical Society, 1986. **108**(11): p. 2849-2852.

G. Katzer and A.F. Sax, *Numerical determination of pseudorotation constants.* Journal of Chemical Physics, 2002. **117**(18): p. 8219-8228.

J.H. Kiefer, R.S. Tranter, H. Wang, and A.F. Wagner, *Thermodynamic functions for the cyclopentadienyl radical: The effect of Jahn-Teller distortion.* International Journal of Chemical Kinetics, 2001. **33**(12): p. 834-845.

T.M. Klapotke, *Homopolyatomic nitrogen compounds.* Angewandte Chemie-International Edition, 1999. **38**(17): p. 2536-2538.

H. Koppel, W. Domcke, and L.S. Cederbaum, *Multimode Molecular-Dynamics Beyond the Born-Oppenheimer Approximation.* Advances in Chemical Physics, 1984. **57**: p. 59-246.

A.N. Kost and I.I. Grandberg, *Progress in pyrazole chemistry.* Advances in Heterocyclic Chemistry, 1966. **6**: p. 347-429.

R. Krishnan, J.S. Binkley, R. Seeger, and J.A. Pople, *Self-Consistent Molecular-Orbital Methods .20. Basis Set for Correlated Wave-Functions.* Journal of Chemical Physics, 1980. **72**(1): p. 650-654.

S.M. Kroner, M.P. DeMatteo, C.M. Hadad, and B.K. Carpenter, *The gas-phase acidity of 2(3H)-oxepinone: A step toward an experimental heat of formation for the 2-oxepinoxy radical.* Journal of the American Chemical Society, 2005. **127**(20): p. 7466-7473.

N. Kunioshi, M. Touda, and S. Fukutani, *Computational study on the formation of five-membered rings in PAH through reaction with O_2.* Combustion and Flame, 2002. **128**(3): p. 292-300.

A. Ledwith and D. Parry, *1,3-Dipolar cycloaddition reactions of diazo alkanes. II. Kinetics of the thermal and photochemical formation of pyrazole from diazopropene.* Journal of the Chemical Society B: Physical Organic, 1967(1): p. 41-42.

C.T. Lee, W.T. Yang, and R.G. Parr, *Development of the Colle-Salvetti Correlation-Energy Formula into a Functional of the Electron-Density.* Physical Review B, 1988. **37**(2): p. 785-789.

D.G. Leopold, K.K. Murray, and W.C. Lineberger, *Laser Photoelectron-Spectroscopy of Vibrationally Relaxed CH_2^- - a Reinvestigation of the Singlet Triplet Splitting in Methylene.* Journal of Chemical Physics, 1984. **81**(2): p. 1048-1050.

D.G. Leopold, K.K. Murray, A.E.S. Miller, and W.C. Lineberger, *Methylene - a Study of the $X\,^3B_1$ and $^1A_1$ States by Photoelectron-Spectroscopy of CH_2^- and CD_2^-.* Journal of Chemical Physics, 1985. **83**(10): p. 4849-4865.

G.R. Liebling and H.M. McConnell, *Study of molecular orbital degeneracy in C_5H_5.* Journal of Chemical Physics, 1965. **42**(11): p. 3931-3934.

S. Mahapatra, H. Koppel, and L.S. Cederbaum, *Impact of nonadiabatic coupling between the conically intersecting $X\,^2A_1$ and $A\,^2B_2$ states of NO_2 on the negative ion photoelectron spectra of NO_2^-*. Journal of Chemical Physics, 1999. **110**(12): p. 5691-5701.

M. Marynowski, W. Franzen, and M. Elbatanouny, *Analysis of the Properties of an Electrostatic Triplet Quadrupole Lens Used as an Electron-Beam Transport Device.* Review of Scientific Instruments, 1994. **65**(12): p. 3718-3723.

D.M. Matheu, A.M. Dean, J.M. Grenda, and W.H. Green, *Mechanism generation with integrated pressure dependence: A new model for methane pyrolysis.* Journal of Physical Chemistry A, 2003. **107**(41): p. 8552-8565.

S. Matsika and D.R. Yarkony, *Conical intersections of three electronic states affect the ground state of radical species with little or no symmetry: Pyrazolyl.* Journal of the American Chemical Society, 2003. **125**(41): p. 12428-12429.

M. Mayer, L.S. Cederbaum, and H. Koppel, *Ground-State Dynamics of NO_3 - Multimode Vibronic Borrowing Including Thermal Effects.* Journal of Chemical Physics, 1994. **100**(2): p. 899-911.

C.S. McEnally and L.D. PFefferle, *The effects of slight premixing on fuel decomposition and hydrocarbon growth in benzene-doped methane nonpremixed flames.* Combustion and Flame, 2002. **129**(3): p. 305-323.

R. Meyer, F. Graf, T.K. Ha, and H.H. Gunthard, *Jahn-Teller Effect in Cyclopentadienyl Radical - Delocalized Vibronic Valence Isomerization.* Chemical Physics Letters, 1979. **66**(1): p. 65-71.

R.B. Moffett, *Cyclopentadiene and 3-chlorocyclopentene.* Organic Syntheses, 1952. **32**: p. 41-44.

C.E. Moore, *Atomic Energy Levels*. NSRDS-NBS. 1952, Washington: US GPO Circular No. 467.

H. Muller, H. Koppel, and L.S. Cederbaum, *Topology and Dynamics of Vibronically Coupled Potential-Energy Surfaces - General-Aspects and Application to the Ozone Cation.* New Journal of Chemistry, 1993. **17**(1-2): p. 7-29.

H.H. Nelson, L. Pasternack, and J.R. Mcdonald, *Excitation and Emission-Spectra of the $^2A_2'' \leftrightarrow {}^2E_1''$ System of the Gas-Phase Cyclopentadienyl Radical.* Chemical Physics, 1983. **74**(2): p. 227-237.

D.M. Neumark, K.R. Lykke, T. Andersen, and W.C. Lineberger, *Laser Photodetachment Measurement of the Electron-Affinity of Atomic Oxygen.* Physical Review A, 1985. **32**(3): p. 1890-1892.

D.M. Neumark, *Transition-State Spectroscopy Via Negative-Ion Photodetachment.* Accounts of Chemical Research, 1993. **26**(2): p. 33-39.

M.T. Nguyen and T.K. Ha, *Decomposition mechanism of the polynitrogen N_5 and N_6 clusters and their ions.* Chemical Physics Letters, 2001. **335**(3-4): p. 311-320.

T.L. Nguyen, T.N. Le, and A.M. Mebel, *Thermochemistry of cyclopentadienylidene (c-C_5H_4, C_{2v}, $^3B_1$), cyclopentadienyl radical (c-C_5H_5•, C_{2v}, $^2B_1$) and 1,3-cyclopentadiene (c-C_5H_6, C_{2v}, $^1A_1$): a theoretical study by the G2M(RCC,MP2) method.* Journal of Physical Organic Chemistry, 2001. **14**(3): p. 131-138.

R.A.J. OHair, S. Gronert, and C.H. DePuy, *New insights into the gas-phase anion chemistry of nitrous oxide.* European Mass Spectrometry, 1995. **1**(5): p. 429-436.

H. Ostmark, S. Wallin, T. Brinck, P. Carlqvist, R. Claridge, E. Hedlund, and L. Yudina, *Detection of pentazolate anion (cyclo-N_5^-) from laser ionization and decomposition of solid p-dimethylaminophenylpentazole.* Chemical Physics Letters, 2003. **379**(5-6): p. 539-546.

I. Ozkan, *Franck-Condon Principle for Polyatomic-Molecules - Axis-Switching Effects and Transformation of Normal Coordinates.* Journal of Molecular Spectroscopy, 1990. **139**(1): p. 147-162.

R.G. Pearson, *A symmetry rule for predicting molecular structure.* Journal of the American Chemical Society, 1969. **91**: p. 4947-4955.

J.H. Richardson, L.M. Stephenson, and J.I. Brauman, *Photodetachment of Electrons from Large Molecular Systems - Pyrrolate Ion - Electron Affinity of C_4H_4N.* Journal of the American Chemical Society, 1975. **97**(5): p. 1160-1162.

J.C. Rienstra-Kiracofe, D.E. Graham, and H.F. Schaefer, *Medium ring compounds and their anions: a systematic density functional theory study.* Molecular Physics, 1998. **94**(5): p. 767-787.

K. Roy, M. Braun-Unkhoff, P. Frank, and T. Just, *Kinetics of the cyclopentadiene decay and the recombination of cyclopentadienyl radicals with H-atoms: Enthalpy of formation of the cyclopentadienyl radical.* International Journal of Chemical Kinetics, 2002. **34**(3): p. 209-222.

M.P. Sammes and A.R. Katritzky, *The 3H-Pyrazoles.* Advances in Heterocyclic Chemistry, 1983. **34**: p. 1-52.

A. Samuni and P. Neta, *Electron-Spin Resonance Study of Reaction of Hydroxyl Radicals with Pyrrole, Imidazole, and Related Compounds.* Journal of Physical Chemistry, 1973. **77**(13): p. 1629-1635.

T. Sato, K. Tokunaga, and K. Tanaka, *Vibronic coupling in cyclopentadienyl radical: A method for calculation of vibronic coupling constant and vibronic coupling density analysis.* Journal of Chemical Physics, 2006. **124**(2). 024314.

T.E. Sharp and H.M. Rosenstock, *Franck-Condon factors for Polyatomic Molecules.* J. Chem. Phys., 1964. **41**: p. 3453-3463.

J. Simons, *Detachment Processes for Molecular Anions*, in *Photoionization and Photodetachment*, C.Y. Ng, Editor. 1999, World Scientific: River Edge, NJ. p. 958-1010.

M.S. Skjoth-Rasmussen, P. Glarborg, M. Ostberg, J.T. Johannessen, H. Livbjerg, A.D. Jensen, and T.S. Christensen, *Formation of polycyclic aromatic hydrocarbons and soot in fuel-rich oxidation of methane in a laminar flow reactor.* Combustion and Flame, 2004. **136**(1-2): p. 91-128.

L.C. Snyder, *Jahn-Teller distortions in cyclobutadiene, cyclopentadienyl radical, and benzene positive and negative ions.* Journal of Chemical Physics, 1960. **33**: p. 619-621.

J.F. Stanton and J. Gauss, *Analytic Energy Derivatives for Ionized States Described by the Equation-of-Motion Coupled-Cluster Method.* Journal of Chemical Physics, 1994. **101**(10): p. 8938-8944.

J.F. Stanton, *Coupled-cluster theory, pseudo-Jahn-Teller effects and conical intersections.* Journal of Chemical Physics, 2001. **115**(22): p. 10382-10393.

S. Sun and E.R. Bernstein, *Vibronic Structure of the Cyclopentadienyl Radical and Its Nonrigid Van-Der-Waals Cluster with Nitrogen.* Journal of Chemical Physics, 1995. **103**(11): p. 4447-4454.

R.W. Taft, F. Anvia, M. Taagepera, J. Catalan, and J. Elguero, *Electrostatic Proximity Effects in the Relative Basicities and Acidities of Pyrazole, Imidazole, Pyridazine, and Pyrimidine.* Journal of the American Chemical Society, 1986. **108**(12): p. 3237-3239.

B.A. Thrush, *Spectrum of the cyclopentadienyl radical.* Nature, 1956. **178**: p. 155-156.

C. Valli, C. Blondel, and C. Delsart, *Measuring electron affinities with the photodetachment microscope.* Physical Review A, 1999. **59**(5): p. 3809-3815.

A. Vij, J.G. Pavlovich, W.W. Wilson, V. Vij, and K.O. Christe, *Experimental detection of the pentaazacyclopentadienide (pentazolate) anion, cyclo-N_5^-.* Angewandte Chemie-International Edition, 2002. **41**(16): p. 3051-3054.

S.M. Villano, A.J. Gianola, S. Kato, V.M. Bierbaum, and W.C. Lineberger, *Manuscript in preparation.*

J. Wei, A. Kuczmann, J. Riedel, F. Renth, and F. Temps, *Photofragment velocity map imaging of H atom elimination in the first excited state of pyrrole.* Physical Chemistry Chemical Physics, 2003. **5**(2): p. 315-320.

P.G. Wenthold, M.L. Polak, and W.C. Lineberger, *Photoelectron spectroscopy of the allyl and 2-methylallyl anions.* Journal of Physical Chemistry, 1996. **100**(17): p. 6920-6926.

P.G. Wenthold and W.C. Lineberger, *Negative ion photoelectron spectroscopy studies of organic reactive intermediates.* Accounts of Chemical Research, 1999. **32**(7): p. 597-604.

R.H. Wiley, ed., *Chemistry of Heterocyclic Compounds, Vol. XXII: Pyrazoles, Pyrazolines, Pyrazolidines, Indazoles, and Condensed Rings*. 1967.

L. Yu, S.C. Foster, J.M. Williamson, M.C. Heaven, and T.A. Miller, *Rotationally Resolved Electronic-Spectrum of Jet-Cooled Cyclopentadienyl Radical.* Journal of Physical Chemistry, 1988. **92**(15): p. 4263-4266.

L. Yu, J.M. Williamson, and T.A. Miller, *Rotationally Resolved Electronic-Spectrum of Jet-Cooled Deuterated Cyclopentadienyl Radical.* Chemical Physics Letters, 1989. **162**(6): p. 431-436.

L.A. Yu, D.W. Cullin, J.M. Williamson, and T.A. Miller, *High-Resolution Laser Spectroscopy of Asymmetrically Deuterated Cyclopentadienyl Radicals - a Study of Vibronic Degeneracy Resolution and Jahn-Teller Distortion.* Journal of Chemical Physics, 1993. **98**(4): p. 2682-2698.

S. Zilberg and Y. Haas, *A valence bond analysis of electronic degeneracies in Jahn-Teller systems: Low-lying states of the cyclopentadienyl radical and cation.* Journal of the American Chemical Society, 2002. **124**(36): p. 10683-10691.